Advancements in the Aerosol Robotic Network (AERONET) Version 3 Database – Automated Near Real-Time Quality Control Algorithm with Improved Cloud Screening for Sun Photometer Aerosol Optical Depth (AOD) Measurements

David M. Giles[1,2], Alexander Sinyuk[1,2], Mikhail G. Sorokin[1,2], Joel S. Schafer[1,2], Alexander Smirnov[1,2], Ilya Slutsker[1,2], Thomas F. Eck[2,3], Brent N. Holben[2], Jasper Lewis[2,4], James Campbell[5], Ellsworth J. Welton[2], Sergey Korkin[2,3], and Alexei Lyapustin[2]

[1]Science Systems and Applications Inc. (SSAI), Lanham, MD 20706, USA
[2]NASA Goddard Space Flight Center (GSFC), Greenbelt, MD 20771, USA
[3]Universities Space Research Association (USRA), Columbia, MD 21046, USA
[4]Joint Center for Earth Systems Technology, University of Maryland, Baltimore County, Baltimore, MD 21250, USA
[5]Marine Meteorology Division, Naval Research Laboratory (NRL), Monterey, CA 93943, USA

Correspondence: David M. Giles (David.M.Giles@nasa.gov)

Abstract. The Aerosol Robotic Network (AERONET) provides highly accurate, ground-truth measurements of the aerosol optical depth (AOD) using Cimel Electronique Sun/Sky radiometers for more than 25 years. In Version 2 (V2) of the AERONET database, the near real-time AOD was semi-automatically quality controlled utilizing mainly cloud screening methodology, while additional AOD data contaminated by clouds or affected by instrument anomalies were removed manually before attaining quality assured status (Level 2.0). The large growth in the number of AERONET sites over the past 25 years resulted in significant burden to manually quality control millions of measurements in a consistent manner. The AERONET Version 3 (V3) algorithm provides fully automatic cloud screening and instrument anomaly quality controls. All of these new algorithm updates apply to near real-time data as well as post-field deployment processed data, and AERONET reprocessed the database in 2018. A full algorithm redevelopment provided the opportunity to improve data inputs and corrections such as unique filter specific temperature characterizations for all visible and near-infrared wavelengths, updated gaseous and water vapor absorption coefficients, and ancillary data sets. The Level 2.0 AOD quality assured data set is now available within a month after post-field calibration, reducing the lag time from up to several months. Near real-time estimated uncertainty is determined using data qualified as V3 Level 2.0 AOD and considering the difference between the AOD computed with the pre-field calibration and AOD computed with pre-field and post-field calibration. This assessment provides a near real-time uncertainty estimate where average differences of AOD suggest a +0.02 bias and one sigma uncertainty of 0.02, spectrally, but the bias and uncertainty can be significantly larger for specific instrument deployments. Long-term monthly averages analyzed for the entire V3 and V2 databases produced average differences (V3−V2) of +0.002 with a ±0.02 standard deviation, yet monthly averages calculated using time-matched observations in both databases were analyzed to compute an average difference of −0.002 with a ±0.004 standard deviation. The high statistical agreement in multi-year monthly averaged AOD validates the advanced automatic data quality control algorithms and suggests that migrating research to the V3 database will corroborate most V2 research conclusions and likely lead to more accurate results in some cases.

1 Introduction

Space-based, airborne, and surface-based Earth observing platforms can remotely retrieve or measure aerosol abundance. Each method has its own assumptions and dependencies in which the aerosol total column abundance quantified by aerosol optical depth (AOD) introduces uncertainty in the retrieval or measurement. At the forefront, ground based Sun photometry has been considered the ground truth in the measurement of AOD given minimal assumptions, reliable calibration, and weak dependency on trace gases at carefully selected wavelength bands thus resulting in highly accurate data (Holben et al., 1998). Meanwhile, AOD inferred from other observing platforms such as satellite retrievals provide quantitative AOD but with significantly higher uncertainty (Remer et al., 2005; Li et al., 2009; Levy et al., 2010; Sayer et al., 2013). Further, in situ measurements lack the ability to provide a reliable columnar AOD due to the requirement of measuring aerosols vertically in each layer while not perturbing or modifying the particle properties during the measurement (Redemann et al., 2003; Andrews et al., 2017). Light Detection and Ranging (LIDAR) is fundamental in the determination of the vertical aerosol extinction distribution (Welton et al., 2000; Omar et al., 2013). Quantification of columnar AOD from ground-based LIDAR, for example, may be less reliable due to low signal to noise ratio during the daylight hours at high altitudes and below the overlap region in which the aerosols very near the surface are poorly observed by LIDAR. Satellite retrieval issues include determining the AOD for very high aerosol loading episodes, cloud adjacency effects, land/water mask depiction, surface reflectance, highly varying topography, and aerosol type assumptions (Levy et al., 2010; Levy et al., 2013; Omar et al., 2013). With each of these measurement platforms, uncertainties exist with AOD; however, these concerns are minimized with AOD measurements from surface based Sun photometry such as from the federated Aerosol Robotic Network (AERONET). Ground-based Sun photometry, a passive remote sensing technique, is robust in measuring collimated direct sunlight routinely during the daytime in mainly cloud-free conditions (Shaw 1983; Holben et al., 1998; Takamura and Nakajima 2004, Smirnov et al., 2009; Kazadzis et al., 2018). While these surface-based measurements are only point measurements, the federated AERONET provides measurements of columnar AOD and aerosol characteristics over an expansive and diverse geographic area of the Earth's surface at high temporal resolution.

Standardization of Sun photometer instrumentation, calibration, and freely available data dissemination of AOD and related aerosol databases highlights the success of the federated AERONET. For more than 25 years, the AERONET federation has expanded due to the investments and efforts of NASA (Goddard Space Flight Center, GSFC) (Holben et al. 1998), University of Lille (PHOtométrie pour le Traitement Opérationnel de Normalisation Satellitaire (PHOTONS)) (Goloub et al., 2007), University of Valladolid (Red Ibérica de medida Fotométrica de Aerosoles (RIMA)) (Toledano et al., 2011), other subnetworks (e.g., AEROCAN (Bokoye et al., 2001), AeroSpan (Mitchell et al., 2017), AeroSibnet (Sakerin et al., 2005), CARSNET (Che et al., 2015)), and collaborators at agencies, institutes, universities, and individual scientists worldwide. Conceived in the late 1980s, AERONET's primary objective was to provide an aerosol database for validation of Earth Observing System (EOS) satellite retrievals of AOD and atmospheric correction (Kaufman and Tanré, 1996). In addition to columnar direct Sun AOD, sky radiances were used to infer aerosol characteristics initially from Nakajima et al. (1996) (SkyRad.PAK) and

later by the Dubovik and King (2000) inversion algorithm to obtain products such as aerosol volume size distribution, complex index of refraction, single scattering albedo, and phase functions.

AERONET is a network of autonomously operated Cimel Electronique Sun/sky photometers used to measure Sun collimated direct beam irradiance and directional sky radiance and provide scientific quality column integrated aerosol properties of AOD and aerosol microphysical and radiative properties (Holben et al., 1998; https://aeronet.gsfc.nasa.gov). The development and growth of the program relies on imposing standardization of instrumentation, measurement protocols, calibration, data distribution and processing algorithms derived from the best scientific knowledge available. This instrument network design has led to a growth from two instruments in 1993 to over 600 in 2018. During that time, improvements were made to the Cimel instruments to provide weather-hardy, robust measurements in a variety of extreme conditions. While the basic optical technology has evolved progressively from analog to digital processing over the past 25 years, the most recent Sun/sky/lunar CE318 Model T instruments provide a number of new capabilities in measurement protocols, integrity, and customizability (Barreto et al., 2016).

All of the slightly varying models of the Cimel instruments can have measurement anomalies affecting direct Sun measurements which include measurements in the presence of clouds, various obstructions in the instrument's field of view, or systematic instrumental issues such as electrical connections, high dark currents, and clock shifts to name a few. Some of these issues depend on instrument model and, for more than a decade, these anomalies have been removed semi-automatically utilizing the cloud screening method developed by Smirnov et al. (2000) and further quality controlled by an analyst to remove additional cloud contaminated data and instrument artifacts from the database. Chew et al. (2011) identified up to 0.03 AOD bias at Singapore due to optically thin cirrus clouds for Version 2 Level 2.0 data. Coincidentally, Huang et al. (2011) examined how cirrus clouds could contaminate AOD measurements up to 25% (on average) of the data in April at Phimai, Thailand, in the Version 2 Level 2.0 data set. The number of AERONET sites has increased to more than 600 sites in the network as of 2018 and the labor intensive effort of quality controlling hundreds of thousands of measurements manually had resulted in a significant delay of quality assured data (Level 2.0) in the AERONET Version 2 database.

With these issues at hand, the cloud screening quality control procedure was reassessed as well as all other aspects of the AERONET processing algorithm including instrument temperature characterization, ancillary data set updates, and further quality control automation. Utilizing these improvements, the Version 3 Level 2.0 quality controlled dataset requires only the pre-field and post-field calibrations to be applied to the data so these data can now be released within a month of the final post-field instrument calibration instead being of delayed up to several months. As encouraged by the AERONET community, automatic quality controls in Version 3 are now also applied to near real-time Level 1.5 AOD products allowing for improved data quality necessary for numerous applications such as numerical weather prediction, atmospheric transport models, satellite evaluation, data synergism, and air quality.

114

115   The AERONET Version 3 processing algorithm marks a significant improvement in the quality controls of the Sun

116   photometer AOD measurements particularly in near real-time. The revised AERONET algorithm is introduced by

117   first reviewing the calculations made to compute the AOD plus changes in the input data sets and the resulting

118   calculation of optical depth components. Next, the preprocessing steps and data prescreening are discussed for the

119   Version 3 quality control algorithm. Cloud screening and instrument quality control algorithm changes are

120   discussed with reference to Smirnov et al. (2000), and the solar aureole cirrus cloud screening quality control is

121   introduced for the first time. The automation of instrument anomaly quality controls and additional cloud screening

122   is described in the subsequent sections. Lastly, the AERONET Version 2 and Version 3 database results are

123   analyzed for the entire data set as well as for selected sites.

124   **2   Aerosol Optical Depth Computation**

125   Sun photometry is a passive remote sensing measurement technique in which mainly collimated light generally not

126   scattered or absorbed by the atmosphere illuminates a photodiode detector and this light energy is converted to a

127   digital signal. The digital signal (V) measured by the instrument is proportional to the solar irradiance. The relative

128   solar calibration is derived from the Langley method (Ångstrom 1970; Shaw et al., 1973) utilizing the digital counts

129   from the instrument versus the optical air mass to obtain the calibration coefficient (V_o) by choosing the intercept

130   where optical air mass is zero at the top of the atmosphere (Shaw, 1983). The relative extraterrestrial solar

131   irradiance is proportional to V_o. As shown by Holben et al. (1998) and for completeness in this discussion, the Beer-

132   Lambert-Bouguer law converted to instrument digital counts is shown in Eq. (1):

133

$$V(\lambda) = V_o(\lambda) * d^2 * \exp[-\tau(\lambda)_{Total} * m],$$ **(1)**

134   where $V(\lambda)$ is the measured spectral voltage of the instrument dependent on the wavelength (λ), $V_o(\lambda)$ is the relative

135   extraterrestrial spectral calibration coefficient dependent on λ, d is the ratio of the average to the actual Earth-Sun

136   distance (Michalsky, 1988; USNO, 2018), $\tau(\lambda)_{Total}$ is the total optical depth, and m is the optical air mass, which is

137   strongly dependent on the secant of the solar zenith angle (Kasten and Young, 1989). For the Cimel Sun

138   photometer, the voltage signal is expressed as integer digital counts or digital number (DN). The error in the $\tau(\lambda)_{Total}$

139   is generally dependent on the optical air mass (m) by $\delta\tau$ proportional to m^{-1} and hence the AOD computation error

140   will tend be maximum at m=1 (Hamonou et al., 1999). Cimel instrument repeatability is tested during calibration

141   procedures by comparing voltage ratios between the field instrument and reference instrument to be less than ±1%

142   (Holben et al., 1998). The absolute uncertainty in the AOD measurement can be described as Eq. (2), with

143   calibration uncertainty of V_o being the overwhelmingly dominant error source:

144

$$\delta\tau = \frac{1}{m} * \left(\frac{\delta V}{V} + \frac{\delta V_o}{V_o} + \tau * \delta m\right) \cong \frac{1}{m} * \frac{\delta V_o}{V_o}$$ **(2)**

145

146 The spectral aerosol optical depth (AOD; $\tau(\lambda)_{Aerosol}$) should be computed from the cloud-free spectral total optical

147 depth ($\tau(\lambda)_{Total}$) and the subtraction of the contributions of Rayleigh scattering optical depth and spectrally dependent

148 atmospheric trace gases as shown in Eq. (3).

149

$$\tau(\lambda)_{Aerosol} = \tau(\lambda)_{Total} - \tau(\lambda)_{Rayleigh} - \tau(\lambda)_{H_2O} - \tau(\lambda)_{O_3} - \tau(\lambda)_{NO_2} - \tau(\lambda)_{CO_2} - \tau(\lambda)_{CH_4} \tag{3}$$

150

151 The Rayleigh optical depth ($\tau_{Rayleigh}$) is calculated based on the assumptions defined in Holben et al. (1998), optical

152 air mass (Kasten and Young 1989), and formula by Bodhaine et al. (1999), except correcting the result based on the

153 NCEP derived station pressure. The ozone (O_3) optical depth (τ_{O3}) is dependent on the O_3 absorption coefficient

154 (a_{O3}) for the specific wavelength, the geographic and temporally dependent multi-year monthly climatological Total

155 Ozone Mapping Spectrometer (TOMS) O_3 concentration (C_{O3}), and the O_3 optical air mass (m_{O3}) (Komhyr et al.,

156 1989) using the following formulation: $\tau_{O3} = a_{O3} * C_{O3} * m_{O3}/m$. Similarly, nitrogen dioxide (NO_2) optical depth

157 (τ_{NO2}) is computed using absorption coefficient (a_{NO2}) and geographic and temporally dependent multi-year monthly

158 climatological Ozone Monitoring Instrument (OMI) NO_2 concentration (C_{NO2}) assuming NO_2 scale height is equal to

159 aerosol: $\tau_{NO2} = a_{NO2} * C_{NO2}$. The water vapor optical depth (τ_{H2O}) is calculated based filter dependent (e.g., 1020nm

160 and 1640nm) A and B coefficients (discussed further below) and precipitable water in cm (u) using the following

161 linear formulation: $\tau_{H2O} = A + Bu$. The carbon dioxide (CO_2) optical depth (τ_{CO2}) and methane (τ_{CH4}) use station

162 elevation dependent formulations: $\tau_{CO2} = 0.0087 * P/P_0$ and $\tau_{CH4} = 0.0047 * P/P_0$, assuming the U.S. standard

163 atmosphere (1976) and absorption constants derived from HITRAN. Further descriptions of these calculations are

164 provided below.

165

166 Table 1 provides a list of the spectral corrections used in the calculation of AOD and precipitable water from

167 935nm. The nominal standard aerosol wavelengths are 340nm, 380nm, 440nm, 500nm, 675nm, 870nm, 1020nm,

168 and 1640nm. For wavelengths shorter than and equal to 1020nm, these channels are measured using a Silicon

169 photodiode detector with a spectral range from 320nm to 1100nm. If the Cimel instrument has an InGaAs detector

170 with a 900nm to 1700nm spectral range, then the 1640nm wavelength is measured along with a redundant 1020nm

171 measurement used to compare instrument optical characteristics between detectors, lenses, and collimator tubes.

172 The Cimel SEAPRISM instrument models, which are deployed on ocean or lake platforms as part of the

173 AERONET-Ocean Color component to retrieve normalized water leaving radiances at 8–12 additional visible band

174 wavelengths for ocean and lake remote sensing studies, are similarly corrected for atmospheric effects (Zibordi et

175 al., 2010).

176

177 Rayleigh optical depth calculations require the use of the station pressure (Bodhaine et al., 1999) as well as the

178 optical air mass (Kasten and Young 1989). To determine AERONET site station pressure (P_S), the NCEP/NCAR

179 reanalysis mean sea level pressure and geopotential heights at standard levels (1000hPa, 925hPa, 850hPa, 700hPa,

180 and 600hPa) are fitted by a quadratic function in logarithmic space to infer the station pressure at the corresponding

181 interpolated geopotential height. The NCEP/NCAR reanalysis data are available routinely at six hourly temporal

182 resolution and 2.5 degrees spatial resolution (Kalnay et al., 1996). Errors in the station pressure are generally less
183 than 2hPa when the station elevation is accurate and the weather conditions are benign (i.e., atmospheric pressure
184 tends to be stable), since aerosol measurements are typically performed in mainly cloud-free conditions.
185
186 The 935nm wavelength is used to determine the water vapor optical depth contribution, which is consequently
187 subtracted from the longer aerosol wavelengths (i.e., 709nm SEAPRISM, 1020nm, and 1640nm). The AOD at
188 935nm is extrapolated based on the Ångstrom exponent (AE) computed from the linear regression of the AOD and
189 wavelengths in logarithmic space within the range of 440–870nm excluding channels affected by water vapor
190 absorption (Eck et al., 1999). To extract the precipitable water (PW) in cm from the 935nm measurements, the
191 Rayleigh optical depth and the AOD components need to be subtracted from the total optical depth at 935nm. As a
192 result, the dimensionless column water vapor abundance (u) is obtained using the following equations:
193

$$T_W = \ln\left[T_{935nm[Measured]}\right] - \ln\left[T_{935nm[Extrapolated]}\right]$$
(4)

$$-\ln[T_W] = \ln[V_{o\ 935nm} * d^2] - \ln[V_{935nm}] - m * \left(\tau_{935nm\ AOD} + \tau_{935nm\ Rayleigh}\right)$$
(5)

$$\ln\left[\frac{T_W}{C}\right] = -A * (m_W * u)^B$$
(6)

$$u = \frac{\left[\frac{\ln T_W}{-A}\right]^{1/B}}{m_W}$$
(7)

194
195 where T_W is the water vapor transmission and constants A and B are absorption constants unique to the particular
196 935nm filter, C is an absorption constant assumed to be equal to one (Ingold et al., 2000), d and m are defined in Eq.
197 (1), m_W is the water vapor optical air mass (Kasten et al., 1965), and u is the total column water vapor abundance
198 (Schmid et al., 2001; Smirnov et al., 2004). The total column water vapor abundance (u) is converted to total
199 column water content or PW by using the normalization factor (u_o=10 kg/m^2) and dividing it by the mean value of
200 water density (p_o=1000 kg/m^3) to obtain water column height units of cm (Bruegge et al., 1992; Ingold et al., 2000).
201
202 In the calculation of the filter dependent A and B constants, the water vapor absorption optical thickness is
203 determined by the integration of water vapor extinction coefficient over height from the bottom to the top of the
204 atmosphere. This calculation requires the following inputs to determine the extinction at each height: HITRAN
205 spectral lines with assumed US1976 model standard atmosphere temperature and pressure profiles; the absorption
206 continuum lookup table from the Atmospheric and Environmental Research (AER) Radiative Transfer Working
207 Group (Clough et al., 1989; Mlawer et al., 2012); and Total Internal Partition Sums that define the shape and
208 position of lines dependent on temperature (Gamache et al., 2017). Nine defined total column water vapor amounts
209 (0.5 cm, 1.0 cm, 1.5 cm, 2.0 cm, 2.5 cm, 3.0 cm, 4.0 cm, 5.0 cm, and 6.5 cm) are used to generate water vapor

210 absorption optical depth lookup tables. From these lookup tables, transmittances are calculated based on the
211 bandpass and averaged spectral solar irradiance for the quiet Sun obtained from the University of Colorado
212 LASP/NRL2 model (Coddington et al., 2016) to generate filter-specific A and B coefficients. The one sigma
213 uncertainty in the calculation of PW in cm is expected to be less than 10% compared to GPS precipitable water
214 retrievals (Halthore et al., 1997; Bokoye et al., 2003; Sapucci et al., 2007; Alexandrov et al., 2009; Prasad et al.
215 2009; Bock et al., 2013; Van Malderen et al., 2014; Pérez-Ramírez et al., 2014; Campenelli et al., 2018). The
216 spectral water vapor optical thickness ($\tau_{H2O}(\lambda)$) is determined by computing the average of all A and B constants
217 from the suite of filters affected by water vapor absorption (i.e., 709nm SEAPRISM, 935nm, 1020nm, and 1640nm)
218 in the AERONET database. The $\tau_{H2O}(\lambda)$ is also dependent on the dimensionless total column water vapor abundance
219 (Michalsky et al., 1995; Schmid et al., 1996):

220

$$\tau_{H_2O}(\lambda) = \bar{A}(\lambda) + \bar{B}(\lambda) * u \tag{8}$$

221

222 The contribution of ozone (O_3) optical depth is determined utilizing the total column TOMS monthly average
223 climatology (1978–2004) of O_3 concentration at 1.00° x 1.25° spatial resolution, the O_3 optical air mass using O_3
224 scale height adjustment by latitude (Komhyr et al., 1989), and the O_3 absorption coefficient (Burrows et al., 1999).
225 The OMI O_3 data set is not used here due to instrument sampling anomalies (McPeters et al., 2015). While the
226 TOMS O_3 data set is extensive and generally characterizes the distribution of O_3, recent changes in concentration
227 could introduce some minor uncertainty in AOD. Similarly, the nitrogen dioxide (NO_2) optical depth is calculated
228 using the total column OMI monthly average climatology (2004–2013) of NO_2 concentration at 0.25° x 0.25° spatial
229 resolution and the NO_2 absorption coefficient (Burrows et al., 1998). Tropospheric NO_2 is highly variable spatially
230 due to various source emissions and stratospheric NO_2 concentrations are more stable spatially than the tropospheric
231 NO_2 and can bias the calculation of AOD if neglected (Arola and Koskela 2004; Boersma et al., 2004). Therefore,
232 regions with high tropospheric NO_2 emission will tend to have greater proclivity for deviating from climatological
233 means. Further, NO_2 can vary significantly on the diurnal scale (Boersma et al., 2008). Improved satellite
234 observations, models, or collocation with surface-based PANDORA instruments measuring temporal total column
235 O_3 and NO_2 may assist in reducing the uncertainty and determination of the total column NO_2 optical depth
236 contribution in later versions of the algorithm (Herman et al., 2009; Tzortziou et al. 2012). Concentrations for
237 carbon dioxide (CO_2) and methane (CH_4) are assumed constant and optical depths are computed based on the
238 HITRAN-derived absorption coefficients of 0.0087 and 0.0047 for the 1640nm filter, respectively, and adjusted to
239 the station elevation.

240

241 The calibration of the AOD measurements is traced to a Langley measurement performed by a reference instrument
242 (Shaw 1983; Holben et al., 1998). The reference instruments obtain a calibration based on the Langley method
243 morning only analyses based on typically 4 to 20 days of data performed at a mountaintop calibration sites. The
244 primary mountaintop calibration sites in AERONET are located at Mauna Loa Observatory (19.536° N, 155.576°
245 W, 3402 m) on the island of Hawaii and Izana Observatory (28.309° N, 16.499° W, 2401 m) on the island of

246   Tenerife in the Canary Islands (Toledano et al., 2018). These reference instruments are routinely monitored for

247   stability and typically recalibrated every three to eight months. Reference instruments rotate between mountaintop

248   calibration sites and inter-calibration facilities at NASA GSFC (38.993° N, 76.839° W, 87 m) in Maryland,

249   Carpentras (44.083° N, 5.058° E, 107 m) in France, and Valladolid (41.664° N, 4.706° W, 705 m) in Spain, where

250   reference instruments operate simultaneously with field instruments to obtain pre-field and post-field deployment

251   calibrations. For periods when the AOD is low (τ_{440nm}<0.2), optical air mass is low (m<2), and aerosol loading is

252   stable, the reference Cimel calibration may be transferred to field instruments (Holben et al., 1998). Eck et al. 1999

253   estimates the reference instrument calibration uncertainty impact on AOD varies from 0.0025 to 0.0055 with the

254   maximum representing uncertainty only in the UV channels (340nm and 380nm). In Version 3, the field instrument

255   AOD uncertainty is still estimated to be from 0.01 to 0.02 with the maximum representing the uncertainty only in

256   the UV channels (340nm and 380nm).

257

258   The Version 2 processing used default temperature corrections based on three sensor head temperature (T_S) ranges

259   (T_S<21°C, 21°C≤T_S≤32°C, and T_S>32°C) using a constant nominal temperature sensitivity only for the 1020nm filter

260   direct Sun measurements. In Version 3, measurement temperature sensitivity has been updated for all wavelengths

261   ≥400nm and all measurement types (i.e., direct solar, sky, water, and lunar viewing measurements). Beginning in

262   2010, the temperature sensitivity was characterized for almost all wavelengths uniquely for each Cimel instrument.

263   The temperature effect on signal (i.e., digital number per °C) is a function of the combined sensitivity of the detector

264   and the filter material itself. If any Cimel data relying on a filter was in use prior to 2010 and the filter was not

265   temperature characterized, then the default values for the filter and manufacturer type are applied, if established.

266   Filters in the ultraviolet (i.e., 340nm and 380nm) are not measured for temperature dependence because of low

267   integrating sphere radiance output at these wavelengths. Due to temperature dependence of the field instrument and

268   the reference instrument, the Sun and sky calibration transfer needs to be adjusted by computing the ratio of the

269   Cimel temperature coefficients for each wavelength and for the temperature observed at the time of the calibration.

270   In addition, when the AOD is computed for field instruments, the sensor head temperature is measured for each

271   direct Sun measurement so these data can be adjusted to the temperature response of the instrument optics (i.e.,

272   combined effect of the detector and filters) and electronics.

273

274   The temperature response is measured at the AERONET calibration facilities using an integrating sphere and a

275   temperature chamber where the temperature is varied from −40°C to +50°C. The wavelength dependent

276   temperature coefficient is typically determined from the slope of ordinary least squares regression fit of the digital

277   voltage counts versus the sensor head temperature reading. For this relationship, the second order polynomial fit is

278   computed for 1020nm, while other filters use either a linear or second order polynomial fit (depending on the larger

279   correlation coefficient). For Cimel Model 4 and some Model 5 instruments with two Silicon photodiode detectors,

280   the digital counts for solar aureole and sky instrument gains are used to determine temperature coefficients for each

281   detector (Holben et al., 1998; https://aeronet.gsfc.nasa.gov). Some Model 5 and all Model T instruments perform

282   the direct Sun and sky measurements on the same detector (Silicon or InGaAs) and typically utilize the solar aureole

283   gain digital counts (Barreto et al., 2016; https://aeronet.gsfc.nasa.gov).

284

285   According to Holben et al. (1998), all instruments generally perform measurements sequentially from longer

286   wavelength to the shortest wavelength filters on a rotating filter wheel inside the sensor head, which positions each

287   filter in front of the photodiode detector and behind the sensor head lenses and collimator tube. The robotically

288   controlled sensor head points automatically at the Sun based on the time and geolocation of the instrument. The

289   laboratory tuned 4-quadrant detector provides nearly perfect solar and lunar tracking to one motor step or ~0.1°

290   immediately following the geographic pointing. A dual tube external collimator with internal baffles attached to the

291   top of the sensor head reduces stray light effects into the sensor head 1.2° field of view optical train.

292

293   The instrument performs measurements of the Sun using measurement triplets, that is, performing the series of

294   measurements of all filters at time hh:m0:00 (time notation for hours, minutes, seconds), where for duration of about

295   eight seconds, and then repeating these measurements at hh:m0:30 and hh:m1:00. The resulting one-minute

296   averaged measurement sequence is defined as a triplet measurement and the maximum to minimum range of these

297   measurements is termed the triplet variability. The triplet measurement advantageously allows for separation of

298   homogeneously dispersed aerosols versus highly temporally variable clouds. The triplet measurements are

299   performed either every 15 minutes for older Model 4 instruments or every three minutes for newer Model 5 and

300   Model T instruments increasing the temporal availability of the AOD measurements in the AERONET database.

301   **3   Automatic Quality Controls of Sun Photometrically Measured Aerosol Optical Depth**

302   The AERONET database has provided three distinct levels for data quality: Level 1.0, Level 1.5, and Level 2.0. In

303   Version 2, Level 1.0 was defined as prescreened data, Level 1.5 represented near real-time automatically cloud-

304   cleared data, and Level 2.0 signified automatically cloud-cleared, manually quality controlled data set with pre and

305   post-field calibrations applied. In Version 3, the definitions have been modified substantially for Level 1.5 and

306   Level 2.0. Version 3 Level 1.5 now represents near real-time automatic cloud screening and automatic instrument

307   anomaly quality controls and Level 2.0 additionally applies pre-field and post-field calibrations. The Version 3 fully

308   automated cloud screening and quality control checks eliminate the need for manual quality control and cloud

309   screening by an analyst and increases the timeliness of quality assured data. Note that in all cases each subsequent

310   data quality level requires the previous data level to be available as input (e.g., Level 1.5 requires Level 1.0 and

311   Level 2.0 requires Level 1.5). The following sections will describe these new definitions and automatic quality

312   controls in detail and the impact these new quality assurance measures have on the AERONET database.

313

314   **3.1   Preprocessing Steps and Prescreening**

315   Most preprocessing data quality criteria operate on voltage (V, expressed as the integer digital number (DN)) or

316   sensor head temperature (T_S). The impact of these conditions may immediately remove data from Level 1.0

consideration or later only impact Level 1.5 and Level 2.0 AOD. Each quality control section describes the reasoning for the screening at the specified data quality level. Digital count anomalies typically result from anomalous electronic issues such as very low or high battery voltages, malfunctioning amplifiers, or loose connections of internal control box components. These digital count anomalies mostly affect older Cimel Model 4 (CE318-1) and Model 5 (CE318N) instruments (Holben et al., 1998; https://aeronet.gsfc.nasa.gov), while several of these connection issues have been mitigated in the Cimel Model T (CE318-T) instruments (Barreto et al., 2016).

3.1.1   Electronic Instability

Cimel Model 4 instruments use a 16-bit analog/digital (A/D) converter in the processing unit in which the analog signal from the sensor head detector to the control box is subject to electronic noise. Cimel Model 5 instruments use a 16-bit A/D converter inside the sensor head and the instrument invokes electronic chopping to reduce electronic noise. Cimel Model T instruments utilize an increased quantization from 16 bits to 24 bits, which significantly reduces noise effects. Cimel Model 5 and Model T instruments internally adjust for the dark current (V_D) with each measurement and no separate record is logged. Cimel Model 4 instruments perform V_D measurements after each sky scan (approximately hourly) for each spectrally dependent instrument gain parameter (i.e., Sun, aureole, and sky). Large V_D values generally represent significant instrument electronic instability. Quality controls applied to the V_D will remove the entire day for Model 4 instrument data from all of the quality levels for either of the following conditions: 1) a single dark current measurement is greater than 100 counts for greater than N-1 wavelengths, where N is the total number of wavelengths or 2) more than three dark current measurements are greater than 100 counts for three or more wavelengths.

Amplifiers in the Cimel Model 4 instruments can produce unphysical increases in the digital counts or decreases in the AOD for the 340nm and 380nm wavelengths at large optical air mass (Fig. 1). These instability issues are evaluated simply using a relative threshold with respect to the available visible wavelength AOD measurements. If the τ_{380} is greater than $0.5 * \tau_{340}$ and ($\tau_{440} + \tau_{500\text{ or }675} < \tau_{380} + \tau_{340} - 2.0$), then the triplet measurements for 340nm and 380nm are removed from the database for Level 1.5 and subsequent levels. These quality controls are limited to Model 4 instruments that were not manufactured after 2001; however, the early AERONET database (1993–2005) contains much of these data. New Cimel Model T instruments are replacing Model 4 instruments but over 40 Model 4 instruments remain active in 2018.

The instrument may rarely malfunction by producing constant digital voltages for triplet measurements and the result of keeping these data in the database leads to unphysical variations in the AOD. A frequency analysis is performed to determine if any digital number (DN) values occur more than 10 times in a day. If more than 50% of the DNs are from the same triplet measurement, then this measurement is identified as an anomalous measurement. If more than 50% of the triplet measurements in the day are considered anomalous, then the entire day will be removed from Levels 1.5 and 2.0.

352 ### 3.1.2 Radiometer Sensitivity Evaluation

353 The Cimel 4-quadrant solar near infrared detector requires enough sensitivity to track the Sun and a DN threshold of
354 100 in the near infrared is needed to have sufficient signal. Near infrared wavelengths (e.g., 1020nm) typically have
355 a higher measured solar DN(V) due to higher atmospheric transmission in the presence of fine mode dominated
356 aerosols even in very high aerosol loading conditions. When the DN (V_{870nm} or V_{1020nm}) is less than 100 counts for
357 any measurement of the solar triplet, then the entire solar triplet AOD will be removed for all wavelengths from
358 Level 1.0 and subsequent levels due to potential solar tracking accuracy issues.

359

360 Version 2 data processing assessed the instrument electronic and diffuse light sensitivity by defining a digital
361 number (DN) of 10 to remove solar AOD triplet measurements. Electronic issues impact Cimel Model 4
362 instruments in the UV and short visible wavelengths due to high $DN(V_D)$. Scattered diffuse light into the collimated
363 field of view can affect all instruments and produce unusual AOD changes with optical air mass especially when the
364 aerosol loading is high and optical air mass is large. The signal to noise ratio of the Cimel instrument requires setting
365 a minimum threshold for the determination of the solar measured DN(V) to limit the effect of diffuse radiance in the
366 instrument field of view (Sinyuk et al., 2012). When a dark current $DN(V_D)$ (e.g., ~50–100) is nearly equal to or
367 larger than the measured solar DN(V) (e.g., ~25–50) will result in V and τ decreasing with increasing optical air
368 mass. All wavelengths are evaluated to determine if the measured solar DN(V) (subtracted from the closest
369 temporal dark current $DN(V_D)$ for Model 4 instruments only) is less than $DN(V_O)/1500$, then the identified
370 wavelength will be removed from all AOD levels. A threshold of 1500 is calculated from a DN of 15000, a typical
371 average $DN(V_O)$ for Cimel Models 4 and 5, normalized to a minimum signal DN of 10. The maximum product of
372 AOD times optical air mass ($\tau_m = \tau * m$) of approximately 7.3 is computed by the natural logarithm of 1500 (i.e., ln
373 (15000/10)) for Cimel Model T instruments. For non-Model T instruments, the 100 DN threshold for 870nm and
374 1020nm limits the τ_m to approximately 5.0 (i.e., ln (15000/100)) for only those two wavelengths. The τ_m maximum
375 threshold applies to all channels; however, the signal count can decrease significantly with optical air mass and
376 depend on the wavelength dependence of V_O. For values exceeding the τ_m maximum threshold, the diffuse radiation
377 increases the signal and, as a result, unfiltered AODs show a decrease in magnitude as optical air mass increases for
378 high AOD even when $DN(V_D)$ equals zero. A measured solar DN(V) lower than the ratio $DN(V_O)/1500$ threshold
379 will result in the removal of the solar triplet AOD for the specific wavelength (Fig. 2).

380 ### 3.1.3 Digital Number Triplet Variance

381 As mentioned in Sect. 2, the Cimel instrument performs a direct Sun triplet measurement at regular intervals
382 throughout the day. A variance threshold is applied based on the root mean square (RMS) differences of the triplet
383 measurements relative to the mean of these three values. If the (RMS/mean)*100% of the digital number triplet
384 values is greater than 16%, then these data are not qualified as Level 1.0 AOD (Eck et al., 2014). The digital
385 number temporal variance threshold is sensitive to clouds with large spatial-temporal variance in cloud optical depth
386 and optically thick clouds such as cumulus clouds as well as issues due to poor tracking of the instrument.

3.1.4   Sensor Head Temperature Anomaly Identification

Each Cimel instrument has a fixed resistance (Model 4) or band gap (Models 5 and T) temperature sensor inside the optical head within 0.5 cm of the detector, filter wheel, and optical train assembly. As discussed in Sect. 2, the instrument optics and digital counts can have dependence to the sensor head temperature (T_S) which is saved with each measurement triplet. Sensor head temperatures may be erroneous due to instrument electronic instability or communication issues. These potentially unphysical values of T_S are evaluated by a number of algorithm steps such as checks for 1) constant T_S values, 2) unphysical extreme high or low T_S, 3) potentially physical yet anomalously low T_S with respect to the NCEP/NCAR reanalysis ambient temperatures, and 4) unphysical T_S decreases (dips) or increases (spikes). When the algorithm removes a T_S reading or the T_S measurement is missing, an assessment is made on the instrument temperature response based on ±15°C of the NCEP/NCAR reanalysis temperature for the date and location to determine whether the temperature characterization coefficient for a specific wavelength would result in a change of AOD by more than 0.02. If this condition is met for a specific wavelength, then data associated with this wavelength-specific triplet measurement will be removed at Level 1.5 and subsequent levels while preserving other less temperature dependent spectral triplet measurements.

3.1.5   Eclipse Circumstance Screening

During episodic solar or lunar eclipses, AOD will increase to the maximum obscuration of the eclipse at a particular location on the Earth's surface. The AOD increases due to the reduction of the irradiance and the celestial body (Moon or Earth) obscuring the calibrated light source (Sun or Moon). While any one point on Earth infrequently experiences an eclipse, when an eclipse episode does occur, the eclipse can affect many locations nearly simultaneously making manual removal tedious at sites distributed globally. To automate the removal of eclipse episodes, the NASA solar and lunar eclipse databases are queried for eclipse circumstances based on geographic position of the site to produce a table of eclipse episodes starting from 1992. The eclipse tool utilizes established Besselian elements based on the Five Millennium Canon of Solar Eclipses: −1999 to +3000 (Espenak and Meeus 2006) to quantify the geometric and temporal position of the celestial bodies (Sun, Earth, and Moon), determine the type of eclipse (e.g., partial, annular, total), and predict times of the various stages of the solar or lunar eclipse. For the Version 3 database, the eclipse site-specific tables are used to discretely remove triplet measurements affected by any stage of the eclipse circumstance. For example, during a solar eclipse, solar triplets will be removed between the partial eclipse first contact to the partial eclipse last contact regardless of the eclipse obscuration or magnitude for Level 1.5 data and subsequent levels (Fig. 3). The partial eclipse first contact is defined as the time at which the penumbral shadow is visible at a point on the Earth's surface and the partial eclipse last contact is defined as the time at which the penumbral shadow is no longer visible a point on the Earth's surface. Efforts to retain AOD during solar eclipse episodes have been attempted by the authors in which up to 95% of the AOD can be corrected based on adjusting calibration coefficients by the eclipse obscuration. However, spectral calibration coefficients also need to be adjusted to account for the solar atmosphere spectral irradiance, which becomes more dominant during the solar eclipse episode and is a topic of further investigation.

3.1.6   Very High AOD Retention

Cloud screening procedures in the next section may inadvertently remove aerosol in very high aerosol loading cases due to biomass burning smoke and urban pollution as discussed by Smirnov et al. (2000). For Version 3, each triplet reaching Level 1.0 is evaluated for possible retention in the event that a specific Level 1.5 cloud screening procedure removes the triplet. When the AOD measurement for 870nm is >0.5 and AOD 1020nm >0.0, these conditions will potentially qualify the triplet for very high AOD retention. Further analysis is performed on those qualified triplets to remove the effect of heavily cloud-contaminated data using the AE for the wavelength ranges of 675–1020nm or 870–1020nm (Eck et al., 1999). If the $AE_{675-1020nm}$>1.2 (or $AE_{870-1020nm}$>1.3, if AOD_{675nm} is not available), and the AE for the same range is less than 3.0, then the triplet qualifies for very high AOD retention and the triplet can be retained at Level 1.5 even if the measurement does not pass Level 1.5 cloud screening quality control steps in Sect. 3.2.

3.1.7   Total Potential Daily Measurements

Cloud screening methods in Sect. 3.2 may incompletely remove all cloud-contaminated points and leave data fragments. To mitigate this issue, a methodology was developed based on the total number of potential measurements in the day and calculated AE values. The total number of potential measurements in the day is defined as the number of triplet measurements plus the number of wet sensor activations. If the number of remaining measurements after all screening steps in Sect. 3.2 are performed is less than three measurements or less than 10% of the potential measurements (whichever is greater), then the algorithm will remove the remaining measurements. This condition is repeated after each cloud screening step in Sect. 3.2 and will only be activated when the very high AOD restoration is not triggered (see Sect. 3.1.6) or when the $AE_{440-870nm}$ is less than 1.0 for a triplet measurement indicating large particles such as clouds may contaminate the remaining measurements.

3.1.8   Optical Air Mass Range

The basic Cimel Sun photometer Sun and sky measurement protocols were specified to NASA requirements in Holben et al. (1992, 1998, and 2006), and have only been slightly modified since that time for improved measurement capability of the Model 5 and Model T instruments (Barreto et al., 2016). All instruments systematically perform direct Sun measurements between the optical air mass (*m*) of 7.0 in the morning and *m* of 7.0 in the evening. In Version 2 and earlier databases, AERONET data processing limited the Level 1.5 and Level 2.0 AOD computation from *m* of 5.0 in the morning to *m* of 5.0 in the evening. The *m* limitation may avoid potential error in the computation of the optical air mass at large solar zenith angles (Russell et al., 1993) and possible increased cloud contamination (Smirnov et al., 2000). For Version 2 and 3 processing, the Kasten and Young 1989 formulation was used to account for very small differences in the optical air mass calculations at high solar zenith angles. Noting that the AOD error ($\delta\tau/m$) has a minimum at large *m* (conversely a maximum at solar noon), the maximum *m* of 5.0 was extended to *m* of 7.0 in Version 3 processing. The larger optical air mass range leads to an increase in the number of solar measurements occurring in the early morning and the early evening contributing to additional AOD measurements used for input for almucantar and hybrid inversions plus an increase in AOD

457 measurements at high latitude sites when solar zenith angles may be large even at solar noon. The impact on the
458 cloud screening performance appears to be minimal for measurements closer to the horizon. The fidelity of the
459 Version 3 cloud screening (see Sect. 3.2) AODs supports the extended optical air mass range for Level 2.0.

460 **3.2   Level 1.5 AOD Cloud Screening Quality Controls**

461 As discussed in Sect. 3.1, several preprocessed criteria and parameters are necessary to quality control the AOD data
462 quality in near real-time (NRT). Cloud screening procedures proposed by Smirnov et al. (2000) were designated to
463 remove or reduce cloud contaminated AOD measurements. However, these procedures also had the effect of
464 surreptitiously removing occasionally other non-cloud anomalies such as repeated AOD diurnal dependence when
465 AOD had a large maximum at midday and minimum at high optical air masses due to environmental impacts on the
466 optical characteristics of the instrument (e.g., moisture on the sensor head lens or spider webs in the collimator
467 tube). While these cloud screening methods have been implemented for about 25 years, the state of knowledge has
468 progressed over this period and thus necessitates review and modification of cloud screening quality control
469 procedures (Kaufman et al. 2005, Chew et al., 2011; Huang et al., 2011). The calculation of the AOD at Level 1.0
470 essentially represents the following in Eq. (9):

471

$$\tau_{app\,Total} = \frac{1}{\Gamma_{anomaly}}\left(\tau_{aerosol} + \frac{\tau_{cirrus}}{C_{cirrus}} + \tau_{liquid\,cloud} + \tau_{eclipse}\right) \tag{9}$$

472

473 where $\tau_{app\,Total}$ is the apparent total optical depth, which at this point in the data processing, may be affected by the
474 contributions of liquid cloud droplets ($\tau_{liquid\,cloud}$), cirrus amplification factor (C_{cirrus}) applied to the cirrus crystal
475 optical depth (τ_{cirrus}) due to strong forward scattering into the field of view of the instrument, solar or lunar eclipses
476 ($\tau_{eclipse}$), and instrument anomalies ($\Gamma_{anomaly}$ adjustment factor). Given cloud free conditions and perfect instrument
477 operation, the additional non-aerosol τ components would be zero and C_{cirrus} and $\Gamma_{anomaly}$ would be one. However,
478 the Cimel Sun photometer always attempts to measure the Sun if it can be tracked regardless of the total optical
479 depth magnitude.

480

481 Clouds are a major factor in the effort to quality control remotely sensed aerosol data (Smirnov et al. 2000; Martins
482 et al. 2002; Kaufman et al., 2005; Chew et al., 2011; Kahn and Gaitley 2015). A significant portion of the liquid
483 cloud contribution is removed by the prescreening prior to Level 1.0 as discussed in Sect. 3.1.3. The $\tau_{app\,Total}$ should
484 be adjusted based on a multiplier dependent on the cirrus crystal size ($\tau_{correct}=C_{cirrus}*\tau_{app\,Total}$) according to Kinne et
485 al. (1999). While this cirrus coefficient (C_{cirrus}) is not specifically modelled by Kinne et al. (1999) for the Cimel
486 instrument field of view half angle of 0.6°, this multiplier is likely to be close to one for small cirrus crystals (e.g.,
487 $r_{eff}=6\mu m–16\mu m$), but near two for larger cirrus crystal sizes (e.g., $r_{eff}=25\mu m–177\mu m$). These adjustment factors
488 would result in the reduction of the $\tau_{app\,Total}$ due to forward scattering in the presence of cirrus. On the other hand,
489 liquid water cloud droplets would significantly increase the $\tau_{app\,Total}$ in a manner similar to large dust particles.
490

491   Cimel instruments also may have internal and external anomalous conditions that modify the optical characteristics

492   or response of the instrument resulting in amplification or dampening impacts ($\Gamma_{anomaly}$) of varying magnitudes on

493   the computation of the $\tau_{app\ Total}$. These anomaly adjustments can be difficult to quantify and can have strong

494   dependence on optical air mass (m) or the sensor head temperature (T_S). As a result, the following sections will

495   describe the mechanisms in which these additional cloud and anomaly components are automatically eliminated or

496   reduced as close to zero as possible to provide a quality assured AOD ($\tau_{aerosol}$) after final calibration is applied (see

497   Sect. 4) across the global AERONET AOD database.

498   **3.2.1   Cloud Screening Quality Controls**

499   As Level 1.0 AOD data may have cloud contamination, these data should be considered as potentially cloud

500   contaminated where the triplet measurement represents the apparent AOD ($\tau_{app\ aerosol}$) as defined in the previous

501   section. Table 2 provides a summary of the cloud screening quality control changes from Version 2 to Version 3

502   and these changes are discussed in detail below and Sect. 3.2.2.

503

504   Cimel triplet measurements are performed typically every three minutes (every 15 minutes for older instrument

505   types) and these triplet measurements can detect rapid changes in the $\tau_{app\ aerosol}$ by analyzing the maximum to

506   minimum variability (i.e., the $\Delta\tau_{app\ aerosol}\{MAX-MIN\}$). Assuming that spatial and temporal variance of aerosols

507   plus clouds is much greater than aerosols alone, in many cases, $\Delta\tau_{aerosol}$ would be near zero and $\Delta\tau_{cloud}$ should be

508   much larger than zero when especially liquid phase cloud droplets exist. For Version 2 and earlier databases,

509   Smirnov et al. (2000) methodology utilized all available wavelengths to perform $\tau_{app\ aerosol}$ triplet screening for cloud

510   contamination. Therefore, large triplet variability would indicate the presence of clouds due to large $\Delta\tau_{cloud}$.

511   Analyses (e.g., Eck et al., 2018) have shown that removing the entire triplet measurement when only one or more of

512   the shorter wavelengths indicates a large variation ($\Delta\tau_{aerosol}(\lambda)$ much greater than zero) may not be the most robust

513   approach. For example, in cases of highly variable fine mode aerosols such as smoke can produce large triplet

514   variability as a result of the inhomogeneous nature of the aerosol plume especially for shorter wavelengths (e.g.,

515   340nm, 380nm, 440nm) where fine mode dominated aerosol particles can have radii similar to short wavelength

516   measurements.

517

518   Considering these factors, several potential techniques were explored utilizing various wavelength combinations and

519   utilizing the Spectral Deconvolution algorithm (SDA) fine and coarse mode triplet separation (O'Neill et al., 2001,

520   2003). While the SDA algorithm derived triplets for coarse mode AODs relative change tended to show utility in

521   cloud removal, the SDA algorithm itself could not be applied universally to the AERONET database to due

522   anomalous results in which fine and coarse mode AODs can have a negative relationship when the number of

523   available wavelengths or wavelength range is not satisfied. Anomalies in SDA retrievals can occur when the

524   uncertainty in AOD is relatively large near solar noon compared to the magnitude of AOD as is sometimes the case

525   when only the pre-field deployment calibration has been applied. Upon further consideration of the triplet

526   variability technique, analyses indicated that using all three longest standard AERONET wavelengths (i.e., 675nm,

870nm, and 1020nm) could be used to remove a triplet measurement when they have high triplet variability that exceeds 0.01 or 0.015*AOD (whichever is greater). The reduction in the threshold of the triplet variability criterion is proportional to the magnitude decrease AOD uncertainty compared to UV wavelengths (0.02) to those of visible and near infrared wavelengths (0.01).

While Smirnov et al. (2000) did not impose an Ångstrom exponent limitation, Version 3 processing constrains the $AE_{440-870nm}$ of Level 1.5 data to be within −1.0 and +3.0. In general, the $AE_{440-870nm}$ values outside this range are unphysical and should not be used due to the inconsistency of the AOD spectral dependence. These inconsistencies typically occur at very low optical depth (<0.05) where the uncertainty of the AOD may be up to 100% of the actual value thus producing AE values that are invalid.

The AOD time series smoothness uses a number of numerical methods and fits dependent on the application. For an AOD time series, rapid and large increases are usually the result of cloud contamination. In Version 2 and prior versions, a technique proposed by Smirnov et al. (2000) to implement a smoothness methodology similar to Dubovik et al. (1995). In this scheme, the triplet measurements were considered as discrete points and differences in logarithm of $\tau_{app\,aerosol}$ and relative difference in times between those measurements were utilized to calculate the first derivative differences in which an arbitrary parameter D (similar to the norm of the second derivative) is calculated. In Version 2 and earlier versions, when the value of D was greater than 16 for an AOD measurement time sequence for 500 nm or 440nm, then this triplet was removed from the data set. Further, the smoothness procedure was repeated or measurements were rejected for the day if less than three triplets remained for the day as discussed in Smirnov et al. (2000). While the D=16 threshold was empirically derived, the smoothness parameter is somewhat arbitrary in origin and operates in logarithmic coordinates rather than natural ones. For example, the distribution of aerosol measurements in a single day is typically normally distributed rather than logarithmically distributed. Further, the D parameter smoothness procedure was not always successful at removing cloud-contaminated data and this may be related to the fact that the empirically derived D parameter was tuned for 15-minute triplet measurement intervals rather than three-minute intervals now commonly observed in the network. Therefore, an approach adhering to the relative change in the total optical depth with time is feasible and a more straightforward physical quantification of the change in $\tau_{app\,aerosol}$ with time.

The AOD time series smoothness in Version 3 evaluates the same $\tau_{app\,aerosol}$ 500nm wavelength (or 440nm if 500nm is not available). The Version 3 smoothness method computes the relative rate of change of $\tau_{app\,aerosol}$ per minute and if $\Delta\tau_{app\,aerosol}/\Delta t > 0.01$ per minute, then the larger triplet measurement in the pair is removed and the smoothness procedure will continue to remove triplets until measurement pairs in the day do not surpass the smoothness threshold. The selection of this threshold of 0.01 per minute hinges on the premise that the triplet average does not change rapidly within one minute. The Version 3 smoothness procedure could be affected by extreme changes in AOD due to anomalous aerosol plumes (e.g., biomass burning or desert dust plumes) where a strong gradient exists.

564 After the cirrus cloud screening quality control (to be discussed in the Sect. 3.2.2), triplets are evaluated for spurious
565 or isolated measurements remaining during the day after applying the cloud screening quality control procedures.
566 So-called "standalone points" may be relevant given the ability of the instrument to perform measurements in cloud
567 breaks or gaps. Here, the definition of a standalone triplet is when no triplets are available within 1 hour of the
568 measurement. If the $AE_{440-870nm}$ is greater than 1.0, the algorithm retains the triplet measurement; otherwise, the
569 measurement will be removed from the data set. Further, daily averaged data are evaluated for temporal stability
570 using the AOD stability during the day at 500nm (or 440nm) and daily outlier triplets using the 3-sigma check for
571 AOD at 500nm (or 440nm) and $AE_{440-870nm}$ to be within ±3 standard deviations (Smirnov et al. 2000). Finally, each
572 wavelength is evaluated to be greater than or equal to −0.01 (based on uncertainty of 0.01; Eck et al., 1999). At this
573 point in the quality control algorithm, the remaining triplet measurements are not expected to have a major
574 component of τ_{cloud} or τ_{cirrus}.

575

576 **3.2.2   Novel Cirrus Removal Method Utilizing Solar Aureole Curvature**

577 Utilizing satellite and surface-based LIDAR, studies have shown the AERONET Version 2 Level 2.0 AOD data are
578 impacted by homogeneous optically thin cirrus clouds with a bias up to 0.03 in AOD (DeVore et al., 2009; Chew et
579 al., 2011; Huang et al., 2011). The optically thin cirrus bias can influence radiative forcing calculations and satellite
580 validation when clouds contaminate the measurement (DeVore et al., 2012). In addressing the shortcoming of
581 Smirnov et al. (2000) and manual checks in which the identification of optically thin cirrus clouds give relatively
582 weak signal in the AOD or AE, the authors leveraged high angular resolution radiance measurements routinely
583 performed in the solar aureole region (3.2°–6.0° scattering angle range). While cirrus detection may be possible with
584 other scattering angle ranges, Cimel Sun photometer radiance measurements do not presently have high enough
585 angular resolution from 6.0°–35.0° to reliably and consistency detect cirrus induced atmospheric phenomena (e.g.,
586 solar halos and sun dogs), since these events depend on cirrus crystal shape and orientation and are not always
587 detectable beyond levels of cloud optical depth variability.

588

589 The use of the solar aureole radiance (L_A; $\mu W/cm^2/sr/nm$) with respect to the scattering angle (φ; in radians) has
590 been demonstrated using the Sun and Aureole Measurement (SAM) aureolegraph instrument to indicate the
591 presence of large particles such as cirrus crystals (DeVore et al., 2009, 2012; Haapanala et al., 2017). The effect of
592 the surface reflectance is much less than the radiance of the solar aureole so it is ignored; however, this may become
593 important at very large solar zenith angles and bright surfaces such as snow (Eiden 1968). All Cimel instrument
594 models perform solar aureole measurements at the nominal 1020nm wavelength. The Cimel performs solar triplet
595 measurements directly on the solar disk, while solar aureole radiances are measured mainly during the almucantar,
596 principal plane, and hybrid sky scans. These solar aureole measurements are performed hourly for Models 4 and 5
597 instruments during sky scan scenarios and for Model T instruments before each solar triplet as well as for the hourly
598 almucantar and hybrid sky scan measurements.

599

600 The AERONET measurements of the solar aureole directional radiances (L_A) depend on the absolute calibration of
601 the integrating sphere. The integrating spheres at the AERONET calibration centers provide an absolute calibration
602 traceable to a NIST standard lamp hosted at the NASA GSFC calibration facility. The uncertainty in the radiance
603 calibration is typically less than 3% due to systematic degradation in the lamp levels, changes in integrating sphere
604 characteristics, and instrument spectral signal response. The solar aureole radiance magnitudes also depend on the
605 instrument Sun sensitivity gain settings for each wavelength for Cimel Model 4 and 5 instruments, while the Model
606 T instruments use an internal instrument gain switch applying to all wavelengths (Barreto et al., 2016). The L_A
607 measurements have calibration and temperature correction applied and are measured by all Cimel instruments at the
608 440nm, 675nm, 870nm, and 1020nm wavelengths. Due to lower AOD in fine mode aerosol loading situations, less
609 Rayleigh scattering, and lower calibration uncertainty, the L_A measurements at 1020nm have less noise for
610 evaluating cirrus cloud presence.

611

612 Given that the L_A measurements are performed at discrete φ, we calculate the ordinary least squares linear regression
613 fit on logarithmic scale when more than three scattering angles are available to determine the intercept (a), slope (b),
614 and the correlation coefficient (R). If R is less than or equal to 0.99, then we do not proceed to check for cirrus
615 contamination. When R is greater than 0.99, the curvature (k_o) for the first available scattering angle (φ_o) in the
616 3.2°–6.0° scattering angle range is calculated using the equation of curvature of the signed planar curve, which gives
617 the rate of turning of the tangent vector in Eq. (10) (Kline 1998):

618

$$k = \frac{y''}{(1 + y'^2)^{\frac{3}{2}}} \tag{10a}$$

619

620 The curvature (k) can be formulated by assuming the Power Law function and its derivatives, and, in our
621 application, using the first scattering angle (φ_o) in radians for φ below:

622

$$y = a * \varphi^b \tag{10b}$$

$$y' = a * b * \varphi^{b-1} \tag{10c}$$

$$y'' = a * b * (b - 1) * \varphi^{b-2} \tag{10d}$$

623

624 According to the k formulation, the stronger the forward scattering peak, then the smaller the value of curvature
625 since the second derivative is small and the first derivative is large due to the steepness of the solar aureole
626 radiances. Further, the overall slope of curvature for all of the scattering angles (3.2°–6.0°) can be calculated using
627 the assumption that $y'^2 \gg 1$ rendering the addition of 1 in the denominator of Eq. (10)a insignificant. The slope of
628 the logarithm of curvature versus logarithm of scattering angle is desired and this slope can be calculated using a
629 and b from the linear regression above by converting from logarithmic coordinates. Therefore, we derive the Eq.
630 (11) to determine the slope of curvature dependent only on the slope of the linear regression fit of L_A and φ on
631 logarithmic scale as follows:

$$\ln k = a + (1 - 2b) * \ln \varphi \qquad\qquad (11)$$

633

634   Here, the slope of curvature (M) is defined as ($1-2b$). The value of M will typically be positive since b will tend to
635   be negative due to the dimming of the solar aureole with increasing scattering angle. Alternatively, M can be
636   calculated numerically for each k and φ to obtain similar results. A small value of curvature (k_o) at the smallest
637   scattering angle available represents the possible existence of large particles producing a forward scattering peak.
638   The slope of curvature (M) represents the average characterization of the solar aureole shape across the scattering
639   angle 3.2°–6.0° range where a large magnitude signifies the potential presence of large particles as curvature
640   increases with increasing scattering angle across the forward scattering peak.

641

642   The Micropulse LIDAR Network (MPLNET) is a global network of LIDARs monitoring the vertical distribution of
643   aerosols and clouds (Welton et al., 2000, 2002; Campbell et al., 2002). To determine the thresholds for these Sun
644   photometer solar aureole curvature parameters for different surface types and aerosol environments, the MPLNET
645   LIDAR cloud identification database was used at eight collocated AERONET sites as shown in Table 3. Multi-year
646   MPLNET LIDAR deployment data were analyzed and matched with AERONET observations when the solar zenith
647   angle was less than 30° to minimize the spatio-temporal differences of the zenith pointing LIDAR versus the
648   slantwise pointing of the Sun photometer in which sky condition can be quite different at large solar zenith angles.
649   The MPLNET cloud base height data product was matched with MERRA reanalysis vertical temperature profile
650   corresponding to the geopotential height pressure surface. When a cloud top temperature is less than −37°C, a cloud
651   is designated to be cirrus, while other non-cirrus clouds may contain liquid or mixed phase particles (Sassen and
652   Campbell, 2001; Campbell et al., 2015; Lewis et al., 2016). The partitioning the AERONET data set of solar
653   aureole radiances in terms cirrus clouds, non-cirrus clouds, all clouds, and clear (no cloud base detected) sky
654   condition categories allowed for the empirical determination of potential thresholds for the curvature parameters.
655   For each site, AERONET curvature parameters (k and M) were computed for almucantar and principal plane solar
656   aureole (L_A) measurements (i.e., left and right scans separately) and further categorized based on the coincident
657   LIDAR detected sky condition. These solar aureole radiances have calibration and temperature characterization
658   applied for the 1020nm channel and these L_A measurements were only quality controlled based on the correlation
659   threshold of 0.99 discussed above.

660

661   Figure 4a shows the number distribution of the k at NASA GSFC (38.99° N, 76.84° W) for each of the four LIDAR
662   sky condition categories. The number of the potential clouds is large for magnitudes of k less than 2.0E−5.
663   Similarly, Fig. 4b and Fig. 4c show the number distributions of the M at NASA GSFC for each LIDAR sky
664   condition category. In Fig. 4b, the number of potential clouds generally dominates when the M is greater than 4.3
665   with generally clear or possibly cloudy conditions when M is less than or equal to 4.3. Some overlapping of the
666   categories for M may be related to the differences in the viewing geometry of the sky between the Sun photometer
667   and the LIDAR or inhomogeneous cloud conditions.

668

669 Algorithmically combining the two thresholds of k and M produces a defined distribution of clear versus cloudy sky

670 condition categories. When the threshold of $k<2.0\text{E}{-}5$ is applied first, then the distribution of mainly cloudy

671 conditions becomes more distinct as shown for NASA GSFC in Fig. 4c. The maximum in the number distribution

672 for cirrus is near $M=4.6$ and the maximum in the number distribution of clear sky condition is at $M=4.3$ (Fig. 4c). At

673 Singapore (1.29° N, 103.78° E), Fig. 5c suggests that the distinction of small aerosol particles and larger cirrus cloud

674 ice crystals allows for adequate separation to identify an observation as cloud contaminated using a threshold of M

675 greater than 4.3. Figure 6a shows the number distribution of the curvature at the first scattering angle for coincident

676 AERONET and MPLNET observations at the SEDE BOKER (30.85° N, 34.78° E). Figure 6c shows the distinction

677 is similarly distributed as GSFC and Singapore to potentially identified cirrus contaminated observations. For Fig.

678 6a, the clear sky condition category is much higher in number than other sky condition categories; however, the k

679 values less than the first scattering angle threshold of $2\text{E}{-}5$ (shown by the orange vertical line) indicates a

680 significant presence of dust particles rather than cirrus clouds due to forward scattering of dust. Note that as for Fig.

681 4 and Fig. 5, the x-axis of Fig. 6a is truncated to $1\text{E}{-}4$ but the number distribution continues at values near zero for

682 larger first point curvatures. SEDE BOKER data in Fig. 6c exhibits a significant contribution of clear conditions are

683 preserved indicating that this method does not appear to misidentify dust as cirrus at this mixed dust and urban

684 pollution site.

685

686 When evaluating all of the collocated AERONET/MPLNET sites in Table 3 (Fig. 7), the maximum in the number

687 distribution for cirrus is at $M=4.3$ after the $k<2.0\text{E}{-}5$ threshold is applied with a relative minimum for the clear

688 conditions for $M>4.3$. Given this information, an empirical threshold of $M>4.3$ can be established for maximizing

689 the removal of cirrus clouds and minimizing removal of potentially clear data points. As mentioned previously, the

690 almucantar and principal plane sky scans are performed on an hourly basis. If cirrus clouds are homogeneously

691 distributed in the sky, then this assumption allows for the application of the temporal screening of triplet

692 measurements within 30 minutes of the solar aureole measurement time. As a result, a significant number of cirrus

693 contaminated measurements for $M{\leq}4.3$ are likely removed with this procedure given the normally distributed

694 number distribution of cirrus identified solar aureole measurements around $M=4.3$. For the Cimel Model T

695 instruments, sky scan aureole measurements are superseded by a special solar aureole scan (CCS) performed from

696 3.0° to 7.5° scattering angle range at 0.3° increments (left and right) after each triplet solar measurement; therefore,

697 temporal screening for these triplet measurements is applied within two minutes of the CCS scan. Overall, the

698 aureole curvature cirrus cloud screening quality control decreases the probability of a cirrus bias in the AOD data set

699 globally by using this standard procedure. However, the Version 3 Level 1.5 AOD data set may still be influenced

700 by optically thin or sub-visible cirrus clouds with ice crystals similar in diameter to coarse mode aerosols such as

701 those found at polar latitudes or when solar aureole measurements are not available due to instrument malfunction or

702 incomplete data transfer.

703

704   Figure 8 shows solar aureole radiances have significant nonlinearity with scattering angle when impacted by cirrus

705   clouds while measurements without cirrus are more linear. The SEDE BOKER site is influenced by desert dust.

706   Dust particles can affect the calculation of the k parameter to be close to the threshold of 2E−5 even when cirrus

707   clouds are not present (SEDE BOKER case 1); however, the overall slope is more linear for the non-cirrus case

708   compared to the cirrus case (SEDE BOKER case 2). As a result, the M parameter is much lower and the algorithm

709   action would be to preserve the SEDE BOKER Case 1 data and remove data for SEDE BOKER case 2. Note that

710   the k parameter is quite low for SEDE BOKER Case 1 and in general dusty sites may frequently have k less than

711   2E−5; therefore, the M curvature parameter is needed to prevent inadvertent removal of aerosol data. For fine mode

712   at GSFC case 1 and Singapore, small values of k and large values of M result in removal of the cirrus-contaminated

713   data. For comparison, the GSFC case 2 shows significant linearity when cirrus clouds are not present. The GSFC

714   case 3 and Trinidad Head case show the variation in these curvature parameters at low optical depths in which only

715   one of the curvature parameters indicates the possibility of cirrus clouds. While these two curvature parameters may

716   be used independently in certain conditions, the current algorithm must employ both curvature parameter thresholds

717   to avoid inadvertently identifying aerosols as clouds in dust and low aerosol loading conditions.

718   **3.3**   Level 1.5 Quality Controls to Screen Instrument Anomalies

719   While cloud-screening quality controls remove a significant portion of data impacted by cloud contamination and

720   some instrument anomalies, a portion of the remaining AOD data set can be impacted by internal or external

721   instrument anomalies. Most instrument anomalies can be removed utilizing the prescreening steps outlined in the

722   Sect. 3.1, but a number of issues still exist which are more evident after the cloud screening quality controls have

723   been applied to the data set. A data set with some clouds can mask or offset patterns in the AOD spectra that can

724   clearly identify data anomalies dependent on optical air mass. For AERONET instruments, data anomalies either

725   dependent on the optical air mass, the sensor head temperature, or leakage, degradation, or looseness of the optical

726   interference filter. Section 3.1 addresses the quality control procedure with respect to the instrument temperature

727   dependence. Some instrument anomalies dependent on the optical air mass include deviations of the measurement

728   time to the true time (i.e., time shift) and obstruction of light into the silicon or InGaAs detector (e.g,. dust, moisture,

729   spider webs). Measurements performed at high latitudes have a slowly varying optical air mass and thus optical air

730   mass pattern recognition is more difficult. The AOD spectra may have optical air mass dependence for out of band

731   leakage or degradation of transmittance due to irregularities in the optical filter composition or the AOD may have

732   significant variability due to a loose filter inside the sensor head.

733

734   The retained spectral AOD measurements passing the quality controls from Sect. 3.1 and Sect. 3.2 are evaluated as

735   input for the quality controls in the present section. The removal of nearly all of the clouds and most instrument

736   anomalies from the previous steps allow for more defined pattern recognition. This section will discuss the pattern

737   recognition techniques utilized for the time shift and AOD diurnal dependence, provide a description of the detector

738   consistency, and AOD spectral dependence quality controls. Further, the AOD diurnal dependence algorithm can be

739   used jointly with the detector consistency and AOD spectral dependence quality controls to remove anomalous data

740 with more certainty. These quality controls can be applied for multiple days to remove data impacted by anomalies
741 for more than one day even when clouds interrupt the day-to-day AOD pattern. The final data set is evaluated for
742 the remaining number of observations in a day and deployment period.

743 **3.3.1   Time Shift Screening**

744 AERONET data are transferred by satellite Data Collection Platform (DCP), PC, or SIM card data transfer. The
745 older Vitel satellite transmitters provided a handshake between the instrument and transmitter allowing for time
746 adjustment and newer Sutron Satlink transmitters provide a GPS time stamp to each message. While time shift is
747 not an issue for satellite transmissions, the time shift can become more significant for PC data transfer and even
748 some instruments using SIM card data transfer. AERONET has developed a program called cimel_https_connect
749 that can update the processing unit clock of Cimel Model 5 instruments. Older instruments (Model 4) and old non-
750 AERONET data transfer software (e.g., Cimel ASTPwin) do not have the capability to synchronize the Cimel
751 control box with the time-synced AERONET server. Most non-AERONET software requires the PC time to be
752 updated from a timeserver or GPS system to provide accurate clock synchronization. Even some newer Model T
753 instruments transferring data by PC or SIM can have faulty GPS modules in which the clock deviated significantly.
754 Cimel Model T instruments may allow for the PC software (e.g., cimelTS_https_connect) updating the time and
755 overriding the GPS module.

756

757 A Cimel clock that deviates from true time can result in an optical air mass calculation not appropriate for the actual
758 time especially when the optical air mass varies relatively rapidly diurnally. This instrument anomaly can result in
759 significant changes in the AOD, which affects all wavelengths but most greatly shorter wavelengths (e.g., 340nm,
760 380nm, and 440nm) at large optical air mass when it changes rapidly. In general, longer wavelength AODs (675nm,
761 870nm, and 1020nm) have less impact from erroneous optical air mass calculations due to less influence of
762 molecular (Rayleigh) scattering. As a result, AODs from the longer wavelengths tend to be more stable and AODs
763 from the shorter wavelengths will tend to crossover the longer wavelengths only at one end of the day (near sunrise
764 or near sunset). The timing of the wavelength crossover depends on whether the Cimel clock is too fast or too slow
765 with respect to the actual time. For example, if the time is slow (fast) relative to the actual time, the temporally
766 deviated optical air mass magnitude will be larger (smaller) than the actual optical air mass and thus the short
767 wavelength AODs will be lower (higher) and possibly cross the longer wavelength AODs (significantly increase
768 spectral dependence). In general, Cimel clock temporal deviations in AOD data can be identified using the
769 following:

770   1.   When the shortest available wavelength AOD crosses neighboring UV, visible, and NIR channel
771   AODs near sunset and the short wavelength AOD is decreasing significantly relative a longer stable
772   wavelength (e.g., 870nm) AOD, this condition indicates the Cimel clock is too fast (Fig. 9a).
773   2.   When the shortest available wavelength AOD crosses neighboring UV, visible and NIR channel
774   AODs near sunrise and the short wavelength AOD is increasing significantly relative to a longer stable
775   wavelength (e.g., 870nm) AOD, this condition indicates the Cimel clock is too slow (Fig. 9b).

776

777   The AOD differences and trends are used for a specific optical air mass interval (2.5–7.0), where the temporal clock

778   deviation amplifies the error in optical air mass calculations. Individual day screening is limited to mainly cloud

779   free periods with low AOD in areas with significant variation in optical air mass from ~1.0–7.0.

780

781   The time shift algorithm is applied over a multi-day period. The algorithm scans the current day plus 19 days in the

782   past (~3 week period) to determine if three or more days indicate the occurrence of a time shift. If the multi-day

783   time shift criteria of three or more days are met, then data between the current day and the last occurrence of the

784   time shift are removed from the field deployment. Although the Cimel clock could possibly be adjusted

785   periodically, most time shift issues tend to occur at remote sites and this approach will maximize the removal of data

786   over the multi-day period to minimize the negative impact on the data from the clock-shifted anomalies. Moderate

787   to high aerosol loading can partly mask the temporal AOD time shift pattern and these data periods may not be

788   removed completely unless they occur between periods of lower aerosol loading when the clock shift spectral AOD

789   pattern is more defined.

790

791   **3.3.2   Detector Consistency Quality Control**

792   The instrument external collimator on the sensor head avoids stray light and reduces front lens contamination, while

793   the internal sensor head defines the field of view of the instrument (nominally 1.2°) by the achromatic front lens,

794   filter, and field stop before each detector. The external collimator is composed of two tubes and the aperture design

795   varies slightly by instrument type. The Cimel Model 4 instrument type has two Silicon photodiode detectors in the

796   sensor head to measure the Sun and sky while newer model instruments have one Silicon photodiode and one

797   InGaAs photodiode detector to measure the Sun and sky on both detectors. One of the detectors could be impacted

798   by an obstruction such as a spider web, insect debris, dust, or moisture. For Cimel Model 4 and some Model 5

799   instruments, the sky scan scenario performs two measurements at the 6° azimuth angle for the almucantar and 6°

800   scattering angle for the principal plane at each wavelength over both detectors. For these older instruments, the

801   solar aureole gain is used for the solar Silicon diode detector and the sky gain is used for the sky Silicon diode

802   detector. These redundant measurements can allow for detection of the change in the relative signal but this method

803   is currently more appropriate to use for quality controlling the inversion products due to uncertainty in sky

804   calibration. Newer Model 5 and Model T instruments (with the solar and sky measurements performed on both

805   detectors) do not have the redundant sky measurement; instead, these instruments have a redundant solar

806   measurement at 1020nm in both collimator tubes, where each solar measurement of the triplet is performed within

807   eight seconds of each other. The AOD 1020nm measurements on Silicon and InGaAs detectors can be compared

808   directly to determine if an obstruction exists in front of either of the detectors. Applying a similar approach to Giles

809   et al. (2012), the difference limit ($\Delta\tau_{Limit}$) can be computed using the optical air mass and AOD magnitude dependent

810   formulation (Eq. (12)):

811

$$\Delta\tau_{Limit} = \frac{(0.04 + (0.02 * MIN[\tau_{1020nm}]))}{m} \tag{12}$$

812

813   where *MIN[τ1020nm]* is the minimum of the AOD at 1020nm obtained from the redundant AOD 1020nm

814   measurements on Silicon and InGaAs detectors and *m* is the optical air mass. The difference limit for an AOD

815   1020nm minimum of 1.0 will result in the 0.06/m 1020nm difference limit described in Giles et al. (2012). A more

816   lenient approach is used here based on the AOD magnitude to prevent removal of data for low AOD at 1020nm. At

817   low AOD, the average field instrument uncertainty (up to 0.01) becomes more significant while the maximum AOD

818   error occurs at midday and differences due to their temperature dependency can contribute up to 0.02 AOD bias.

819   Given the relative difference in the AOD 1020nm measurements, the maximum uncertainties in both 1020nm

820   measurements must be considered. Therefore, the 0.02 threshold is derived from the average uncertainty (up to

821   0.01) and the 0.04 limit is derived from the maximum midday error in AOD and temperature dependency (up to

822   0.02). When more than 10% of the total measurements for the day exceed the *Δτ_Limit*, data are removed in the

823   following manner:

824   1. If the AOD 1020nm Silicon subtracted by the AOD 1020nm InGaAs detector is greater than *Δτ_Limit*, then the

825   Silicon side has an obstruction and the entire measurement is removed for both Silicon and InGaAs AOD

826   data.

827   2. If AOD 1020nm Silicon subtracted by the AOD 1020nm InGaAs is less than *−Δτ_Limit*, then the InGaAs

828   detector has an obstruction and only the InGaAs AOD for 1020nm and 1640nm measurements are

829   removed.

830   3. If the redundant AOD 1020nm values are nearly the same (*−Δτ_Limit ≥Δτ≥ Δτ_Limit*), then an obstruction could

831   possibly exist in the event that a substance (e.g., spider webs, dust, moisture) similarly obstruct both

832   detectors.

833   For condition (3), this case is further evaluated by the AOD diurnal dependence quality control in the next section.

834   **3.3.3   Aerosol Optical Depth Diurnal Dependence**

835   The AERONET instrument has spectral calibrations made and typically applied both before and after field

836   deployment. When the instrument operates in the field, the pre-field spectral calibration applied to the near real-time

837   data is constant. If the calibration changes significantly during the instrument deployment, the error in the

838   computation of the AOD increases with decreasing optical air mass where the maximum error occurs when optical

839   air mass approaches one ($\delta\tau*m$; Hamonou et al., 1999). As a result, an apparent diurnal dependence in the AOD can

840   occur depending on the magnitude of the deviation from the pre-field calibration. When both the pre-field and post-

841   field calibrations are applied and data still show a diurnal dependence in the AOD, then the deviation in the field

842   measurements is due to a non-linear change in the calibration coefficient since Level 2.0 data utilize a linear

843   interpolation between the pre-field and post-field calibration coefficients.

844

845   Midday maximum (concave pattern) or midday minimum (convex pattern) of AOD diurnal dependence can be

846   observed at any AOD magnitude but are typically more pronounced at lower aerosol loading due to calibration

847 offset (Cachorro et al., 2004) or instrument anomalies. Quality controls developed for the analysis of the AOD
848 diurnal dependence need to consider the impact of clouds and missing data to assess whether to remove these data
849 while minimizing the removal of data exhibiting true diurnal dependence. For example, one cloud-free day may
850 show diurnal dependence, but on another day, the morning or afternoon data may not be available due to missing
851 data during cloudy or rainy periods. The algorithm must have a sufficient number of observations to perform a
852 robust assessment of the AOD diurnal dependence.

853

854 Variation in the number of available measurements in a day due to clouds or instrument issues can limit the
855 application of a single day only approach. As a result, the morning and afternoon periods must have at least five
856 measurements separately and the analysis of the full day must have at least 10 measurements. To analyze the
857 diurnal dependence and reduce the impact of outliers, the GNU Scientific Library robust least squares (RLS) linear
858 regression fit is performed for AOD versus the inverse optical air mass (m^{-1}, where m is approximately the cosine of
859 the solar zenith angle). The slope and correlation coefficient (R) values derived from the linear fit are used as
860 thresholds to determine the magnitude and strength of the diurnal dependence (Table 4).

861

862 The nominal AERONET 440nm, 675nm, 870nm, and 1020nm wavelengths for the Silicon detector and 1640nm for
863 the InGaAs detector are assessed for diurnal dependence and potential removal of all spectral channels. An example
864 of the AOD diurnal dependence of 1020nm wavelength is shown in Fig. 10 at the Rio Branco (9.96° S, 67.87° W)
865 AERONET site where the site manager indicated spider webs were obstructing measurements. If data are removed
866 for the InGaAs detector, then only InGaAs detector data are removed, while removal of the Silicon detector data will
867 remove all data including InGaAs detector data, if any. The AOD diurnal dependence is classified as two
868 categories: independent and dependent. If the algorithm meets the strict thresholds for "independent" diurnal
869 dependence, then all channels exhibiting diurnal dependence can remove data for a day, except the 1020nm channel
870 since some old data with temperature defaults may exhibit false diurnal dependence. Otherwise, all of the above
871 channels are used for the "dependent" diurnal dependence quality control. The dependent diurnal quality control
872 relies on more lenient thresholds for the slope and R; however, the removal of data generally requires that another
873 quality control flag is set such as the detector consistency quality control (Sect. 3.3.2), where an obstruction was
874 identified in front of one of the detectors or at least one additional qualified wavelength meeting the slope and R
875 thresholds. When a qualified wavelength indicates dependent AOD diurnal dependence for Day or both AM and
876 PM and the AM and PM slopes are positive, then the entire day can qualify for independent removal. This
877 methodology allows for a more skilled approach in removing only data affected by instrumental anomalies while
878 minimizing the removal of data coincidently producing a true diurnal dependence signature.

879

880 The AOD diurnal dependence identification can be complicated by changes in aerosol loading during the day, cloud
881 artifacts, and missing data. A multi-day scan must be performed to maximize the removal of data impacted by
882 instrument anomalies. A multi-day assessment example is provided in Fig. 11 for Rio Branco. Figure 11a shows
883 that the spectral AOD varies significantly diurnally for the period from 26 August to 5 September 2011, especially

884   for the 870nm and 1020nm near infrared wavelengths. Figure 11b shows evaluation of the slope and correlation

885   coefficient (R) for the AOD 1020nm daily variation, which shows 7 of the 10 days exceeding the thresholds (slope >

886   0.1 and R>0.94) and wavelengths established in Table 4. For these data to qualify for dependent AOD diurnal

887   dependence removal, additional information is needed such as another qualified wavelength with slope and R

888   exceeding the thresholds. For this case, the AOD 870nm daily slope and correlation parameters (not shown) also

889   exceed the thresholds, which lead to the elimination of these data from Levels 1.5 and 2.0. Similar to the time shift

890   screening in Sect. 3.3.1, the AOD diurnal dependence algorithm scans the last 19 days including the current day to

891   determine the first occurrence and last occurrence of the dependent and independent AOD diurnal dependence.

892   When three or more days are identified, data are removed from the first occurrence to the last occurrence of AOD

893   diurnal dependence during the 20-day period. The multi-day screening allows for the elimination of data affected by

894   an obstruction in the instrument field of view even with moderately high aerosol loading in the NIR wavelengths

895   and when days with incomplete number of measurements from the established protocol due to clouds.

896   **3.3.4   Reverse Spectral Dependence**

897   While the majority of the cloud screening quality controls remove aerosol measurements contaminated by clouds,

898   some spurious points or slowly varying changes in cloud properties may still affect the data set at this point in the

899   algorithm. A new method (Fig. 12) utilizing the Ångstrom exponent (AE) is applied to the remaining data set for

900   evaluation of cloud contamination. Ångstrom exponents derived from anomalous AOD measurements due to

901   instrument artifacts may produce a similar signature. The spectral dependence among the wavelengths is now much

902   improved compared to Version 2 by removing temperature dependencies that influenced the calculation of the AE at

903   low AODs reducing the effect of improper spectral dependence due to temperature anomalies.

904

905   The AE is computed utilizing the ordinary least squares fit of the logarithms of AOD and wavelength for the ranges

906   of 440–870nm, 870–1640nm (if 1640nm is available), and the 870–1020nm (for Silicon detectors only) range (Eck

907   et al., 1999). The reverse spectral dependence algorithm in Fig. 12 removes cloud contaminated points utilizing

908   these AE ranges depending on the instrument model. Figure 13 shows the removal of the anomalously high AOD at

909   the Bratts Lake (50.20° N, 104.71° W) AERONET site in southwest Canada. In Fig. 13b, all negative and a few

910   positive AE values are identified and the algorithm removes nearly all of the residual cloud contamination in this

911   case. However, the penultimate and final measurements in Fig. 13c have slightly higher AOD than the previous

912   hour of data, which may be due to marginal contamination by optically thin cirrus clouds. Additional algorithm

913   development is still needed to further enhance the removal cloud contaminated data with small ice crystals while not

914   removing dust aerosols.

915   **3.3.5   Aerosol Optical Depth Spectral Dependence**

916   The wavelength dependence of AOD typically is strong for fine mode aerosols (e.g., pollution or smoke) and weak

917   for coarse mode aerosols (e.g., dust or sea salt). The AE provides an index of the strength of the spectral

918   dependence related to the estimation of the possible aerosol size (Eck et al., 1999). In general, the $AE_{440-870nm}$ will

919 typically provide values between approximately 0.0 and 3.0. These prospective values indicate no spectral

920 dependence at $AE_{440-870nm}$ of 0.0 and very strong spectral dependence with an $AE_{440-870nm}$ near 3.0 (AE values of 3.0

921 have not been observed in good quality data with sufficiently high AOD). The spectral dependence can be used to

922 evaluate the quality of each channel given that most channels in the measurement suite adhere to the stated AOD

923 uncertainty of 0.01 for wavelengths ≥400nm and 0.02 for wavelengths <400nm (Eck et al., 1999). The fit of the

924 AOD with wavelength on logarithmic scale should generally be linear for coarse mode dominated or fine/coarse

925 mode particle mixtures. However, in moderate to high aerosol loading cases (especially when fine mode

926 dominated), a quadratic or cubic assumption is needed to fit the data depending on the wavelength range under

927 evaluation (Eck et al., 1999; O'Neill et al., 2008). The ordinary least squares (OLS) methodology is perturbed by

928 the presence of outliers and therefore skews the fit towards outliers. If the boundary wavelengths are impacted by

929 anomalies, the ordinary least squares can poorly fit other intermediate wavelengths.

930

931 In an effort to reduce the influence of outliers, the GNU Scientific Library (GSL Version 2.2.1 C compilation)

932 robust least squares (RLS) technique is utilized to improve the removal of spectral AOD outliers. In general, the

933 OLS technique is sensitive to the endpoints and to the number of points used in the regression. For example, the

934 outlier detection will have less skill with a few points or anomalous endpoints. The RLS scheme uses an iterative

935 approach with up to 100 passes using the Tukey biweight function and assigning the outliers a lower weight with

936 each pass. The RLS approach allows for the more meticulous removal of wavelengths out of spectral dependence

937 and more importantly preserves mid-visible wavelengths that could be removed incorrectly when utilizing the

938 ordinary least squares method.

939

940 Outlier detection is performed utilizing the uncertainty of the AOD measurement and providing an allowable

941 tolerance in the fit given potential irregular nature of the uncertainty (0.01 to 0.02). For wavelengths ≥400nm and

942 <1600nm, the allowable AOD difference between the measurements and fit for a candidate wavelength is

943 (0.02*AOD)+0.02, based on the stated AOD uncertainty for these wavelengths (Holben et al., 1998; Eck et al.,

944 1999). For wavelengths <400nm and 1640nm, the allowable AOD difference between the measurements and fit for

945 a candidate wavelength is (0.02*AOD)+0.04, which is adjusted for greater uncertainty at the UV wavelengths and

946 greater uncertainty in the larger spectral range to fit the 1640nm wavelength.

947

948 The spectral outlier procedure begins by identifying and removing any negative AOD values that are not within the

949 allowable AOD difference from the RLS linear fit. Negative AOD due to slight calibration drift can be observed at

950 very clean locations; otherwise, these negative values may be anomalous. The algorithm will evaluate each

951 wavelength separately and compute the RLS linear fit based on the remaining wavelengths producing the slope,

952 intercept, and R^2 values, where the slope and intercept are used to compute the AOD fit at the wavelength under

953 evaluation. If the algorithm does not identify any wavelengths for removal, then the procedure is complete. If AOD

954 is low (AOD_{440nm}<0.1) and one wavelength AOD exceeds the maximum allowable difference, then the wavelength

955 will be removed due to the linear fit deviation. However, if more than one wavelength has AOD marked for removal

956   for the low AOD condition, then the wavelength with the largest departure from the linear fit to the measurement
957   and largest R^2 will qualify for removal.

958

959   In the case of higher AOD ($AOD_{440nm} \geq 0.1$), the algorithm stores the information from the RLS linear fit and
960   continues to perform a RLS quadratic fit ($400nm \leq \lambda \leq 1020nm$) or a RLS cubic fit ($\lambda = 1640nm$). If the candidate
961   wavelength deviates from the allowable difference in fit to the measurements for the higher order fits, then the
962   wavelength will be removed if it is identified as a wavelength that corresponds to the maximum deviation for the
963   RLS linear fit. Figure 14 provides an example of this condition at the Osaka ($34.65°$ N, $135.59°$ E) AERONET site.
964   After each wavelength removal regardless of order of the fit, the algorithm repeats until no wavelength removals
965   occur or when less than three wavelengths remain.

966   **3.3.6**   **Large Aerosol Optical Depth Triplet Variability**

967   In addition to growth of hygroscopic aerosols near cumulus cloud boundaries and large triplet variability at short
968   wavelengths in highly variable fine mode plumes, a misaligned filter due to improper filter wheel movement or dust
969   on the filter may produce large AOD triplet variability (AOD Max – AOD Min). The cloud screening triplet
970   variability quality control (Sect. 3.2.1) removes the entire measurement when 675nm, 870nm, and 1020nm AOD
971   triplets all have large triplet variability exceeding the threshold (0.01 or 0.015 * AOD, whichever is greater). A
972   situation may exist where one of those wavelengths or shorter wavelengths are impacted by a filter anomaly making
973   it necessary to assess the large AOD triplet variability. If the triplet measurement is identified for high AOD
974   retention (Sect. 3.1.6), then the following large adjacent triplet quality control is not performed because very high
975   aerosol loading in fine mode events can lead to large triplet variability naturally. Occasionally, if the triplet is very
976   large and exceeds the limit of 0.03+0.2*AOD, then the wavelength is removed independently of the next longer
977   wavelength.

978

979   To further screen anomalous triplets individually or the entire day, each triplet and wavelength is evaluated using the
980   triplet variability from the shortest wavelength (e.g., 340nm) and the next longer wavelength (e.g., 380nm). The
981   allowable triplet variability limit is computed based on the aerosol loading and the AOD triplet variability of the
982   next longer wavelength: 0.03+0.02*AOD+triplet_variability_of_next_longer_wave. If the total number of triplets
983   for a wavelength exceeding the large triplet variability threshold is more than 25%, then the AOD measurements for
984   the wavelength are removed completely for the entire day. Figure 15 shows the large triplet variability removal at
985   the PEARL ($80.05°$ N, $86.42°$ W) AERONET site in northern Canada. The triplets at shorter wavelengths may
986   naturally exhibit relatively large triplet variability hence it is necessary to check the shorter wavelength in
987   comparison to the next longer wavelength which typically will be more stable if clouds do not impact the
988   measurements.

3.3.7   Remaining Measurements Evaluation

After the previous quality control algorithms have been applied, extraneous data points may remain and are identified for possible removal. A number of conditions have been implemented based on the total data removed for the day, number of wavelengths remaining for the day, and number of measurements for a wavelength for a deployment. These "cleanup" conditions below will remove all wavelengths in a day for any of the following conditions dependent on the "retain high AOD" from Sect. 3.1.6 and the number of wavelengths in a day:

1. If retain high AOD and less than two wavelengths remain in a day
2. If retain high AOD and two wavelengths but are not 870nm and 1020nm in a day
3. If not retain high AOD and less than three wavelengths remain in a day
4. If not retain high AOD and less than half of the wavelengths remain in a day

Each wavelength must be evaluated for remnant data artifacts. If greater than 50% of the total cloud screened AOD data for a wavelength in a day are removed, then AOD measurements for the candidate wavelength will be removed for the day. Further, a condition is implemented to remove specific wavelengths for an entire deployment. For example, if the number of measurements for a wavelength is less than 20% of the total cloud screened data set for a deployment, then all of the measurements for the specified wavelength will be removed for the deployment. These removal conditions are necessary to fully quality control the spectral AOD data set and avoid unphysically irregular and fragmented data sets.

3.4   Algorithm Performance Assessment

Data quality controls applied to the quality controlled Level 1.0 data set are evaluated for removal performance for each part of the Level 1.0 prescreening and Level 1.5 algorithm. The Level 1.0 prescreening is applied to about 84 million solar triplet measurements from 1993–2018. The radiometric sensitivity screening (see Sect. 3.1.2) for the DN of 1020nm removes about 36% and the digital voltage triplet variance greater than 0.16 (see Sect. 3.1.3) removes nearly 11% of the Level 1.0 data. The remaining Level 1.0 prescreening that check for radiometric sensitivity screening for DN of 870nm, extreme temperatures ($T_S \leq -40°C$ or $T_S > 100°C$), and bad measurement configuration conditions remove approximately 0.5% of the Level 1.0 data. Therefore, nearly half (48%) of the initial 84 million solar triplet measurements are removed by the Level 1.0 prescreening steps due to the presence of clouds in the solar measurements that greatly reduce the signal (e.g., stratus clouds) or exhibit significant temporal variability within the one minute triplet measurement sequence (e.g., cumulus clouds).

The Level 1.5 quality control algorithm is divided into the two main steps for cloud screening and instrument data anomaly removal. Figure 16 shows the percentage of the Level 1.0 data removed by the Level 1.5 cloud screening quality control. Over 23% of the removal in the cloud screening algorithm was due to the large triplets at the long wavelengths (675nm, 870nm and 1020nm). Nearly 5% of the removal of the Level 1.0 data was due to the presence of cirrus clouds as detected by the solar aureole curvature algorithm and is significant since a cirrus contamination bias is evident in the AOD in Version 2 Level 2.0 data set. The "Unqualified" category indicates data that are not

1025 triplets or lack the sufficient channels to participate in the cloud screening part of the algorithm and these
1026 measurements are rejected from Level 1.5. Finally, spectral AOD removed due to too low negative values
1027 (AOD<−0.01) has maximum removal of approximately 0.5% for 380nm and 1% for 340nm of the total Level 1.5
1028 AOD measurements due to 0.02 uncertainty in the UV at very low optical depths, while other AOD wavelengths
1029 have generally much less than 0.5% removal. After all of the data are cloud screened, about 66% of the Level 1.0
1030 data are passed to the second part of the Level 1.5 instrument quality control algorithm for examination of the
1031 instrument anomalies and other spurious clouds and artifacts.

1032

1033 The second stage of the Level 1.5 quality control algorithm utilizes measurements passed from the cloud screening
1034 algorithm. While the cloud screening algorithm rejects the entire measurement in the presence of clouds, the
1035 instrument quality controls can also reject the entire measurement or remove data by wavelength depending on the
1036 anomalous condition. Figure 17 shows the removal of Level 1.5 cloud screened data due to mainly instrument
1037 anomalies for each wavelength. More than 2.5% of the data are removed due to the AOD diurnal dependence
1038 screening, about 2% for the time shift screening, and 1.5% for the AOD 1020nm difference screening. These three
1039 instrument quality control algorithms remove in general the most across all wavelengths. Some removal occurs
1040 significantly spectrally for the InGaAs channel (1640nm). The InGaAs channels can be affected in some
1041 instruments more significantly by water contamination as the InGaAs side of the collimator is facing away from the
1042 Sun when in the parked or resting position. Further, when the algorithm removes all of the Silicon channels, the
1043 remaining InGaAs channels are also removed since no other independent method exists to check the InGaAs
1044 channel data quality. The "Remaining" measurements removal shows that nearly 4% of the cloud screened data are
1045 removed from the InGaAs data set. The AOD spectral dependence removes more than 2% of the 340nm wavelength
1046 data, which tends to be the most unstable wavelength (due to filter degradation), and about 0.5% for all other
1047 wavelengths. The temperature screening removal of missing or anomalous temperatures mostly affects the Silicon
1048 1020nm wavelength with nearly 1% of the cloud-screened data removed due to its large temperature dependence
1049 compared to the other wavelengths.

1050 **4   Assessment of the Quality Assurance Data Set**

1051 The aerosol optical depth (AOD) data will be qualified for consideration of Level 2.0 once it passes the Level 1.5
1052 checks. To reach Level 2.0, these data must meet the following conditions:

1053   1. Data must have pre-field and post-field calibration applied; or in some cases, the pre-field deployment or
1054   post-field deployment calibration may be made constant for the deployment after evaluation of the best
1055   calibration values.
1056   2. Temperature characterization must be applied utilizing the temperature correction for the instrument or
1057   default values for each wavelength.
1058   3. Instrument must be designated as the primary instrument for the site.

1059

1060 Once the above conditions are met, these data are considered to reach Level 2.0. These Level 2.0 data are
1061 recommended for publication and use in various atmospheric applications. The automated quality control algorithm
1062 attempts to preserve aerosol data while removing data artifacts. Some unusual atmospheric conditions (e.g., small
1063 cirrus particles r<5µm) or rare instrument anomalies (e.g., loose filters or partially removed multi-da AOD diurnal
1064 dependence) affecting the AOD may rarely pass through the algorithm and users are advised to consider inspecting
1065 these data carefully when using them for detailed studies. Further, optical air mass dependent anomalies such as the
1066 time shift and AOD diurnal dependence quality controls may allow data to pass when aerosol loading is high or too
1067 few data exist to make an assessment. These quality controls can determine patterns more skillfully at lower aerosol
1068 loading which could result in retaining potentially contaminated high aerosol loading periods when the pattern may
1069 be less defined and does not meet the quality control thresholds.
1070
1071 The subsequent sections discuss the impact of the temperature characterization on the Version 3 Level 2.0 AOD data
1072 to quantify the change in regards to the Version 2 Level 2.0 data set. Further, the assessment of the Version 3 near
1073 real-time product is made to determine the average bias of the AOD based on the applied calibration. Finally, an
1074 analysis is made of the Version 3 Level 2.0 AOD long-term averages for select AERONET sites and these are
1075 compared to the Version 2 Level 2.0 AOD long-term averages.
1076

1077 **4.1   Temperature Characterization Evaluation**

1078 The accurate measurement of the spectral direct-beam Sun intensity (from which AOD is computed) depends on the
1079 sensor head temperature of the instrument as discussed in Sect. 2. The sensor head temperature can vary
1080 significantly since the optical head canister is heated by the Sun and can be much higher (>10°C) than the ambient
1081 temperature especially near solar noon. The temperature sensitivity of the Silicon detector is more significant for
1082 the 1020nm filter due to the proximity to the edge of the spectral range of the detector in which temperature
1083 dependence becomes more significant. The temperature dependence for all wavelengths may vary due to the
1084 composition and/or manufacturing quality of the filters and/or detectors. Due to technical difficulty, the ultraviolet
1085 wavelength (λ<400nm) filters have not been temperature characterized in Version 3; however, UV filters may have
1086 a temperature dependence. Figure 18 shows the difference in the AOD temperature coefficients for Version 3
1087 temperature correction applied to Version 3 data and Version 2 temperature correction applied to Version 3 AOD
1088 data from 1993–2018. The AOD varies most significantly for the Silicon 1020nm channel with a full range of ~0.02
1089 for sensor head temperatures between −25°C and +55°C. Notably, the shorter wavelength channels and the InGaAs
1090 wavelengths (i.e., 1020nm and 1640nm) do not show significant change in AOD less than 40°C. All of the
1091 wavelengths, except the Silicon 1020nm, show an AOD difference decrease from −0.005 to −0.010 for temperatures
1092 greater than 40°C, which may be due to changes in instrument characteristics (e.g., electronic instability in the
1093 instrument) at high temperatures. The decreasing AOD difference with increasing temperature may be related to the
1094 smaller number of observations at high temperatures and contribution by instruments with temperature
1095 characterization measurements that did not reach temperatures greater than 40°C. Temperature characterization has

1096 proven to be small yet necessary adjustment to the AOD computation and this improvement is especially exhibited
1097 in polar regions or sites with very low aerosol loading in which the Version 3 AOD spectra have much less
1098 crossover allowing for the computation of more accurate Ångstrom exponents than in the Version 2 data set.

1099 **4.2   Level 1.5 Near Real-time Aerosol Optical Depth Bias and Uncertainty**

1100 The Version 3 near real-time data set provides improved data quality compared to Version 2 since the algorithm has
1101 improved cloud screening and instrument quality controls applied to the data. The data set can vary in the near real-
1102 time interval from current day up to one month as ancillary data sets are received and processed, hence, these
1103 database changes invoke reprocessing of the AOD throughout the near real-time phase. Once AOD data have been
1104 pre-field and post-field calibrated, then these data may be raised to Level 2.0 as described in Sect. 4. The near real-
1105 time data using only constant pre-field calibration is compared to the quality assured data set that uses both the pre-
1106 field and post-field calibrations applied to the data with the assumption of linear interpolation. Figure 19 shows the
1107 distribution by wavelength for this comparison of the near real-time and quality assured data set for the entire
1108 database of Level 2.0 qualified data excluding calibration site data and deployments using a copied pre-field or post-
1109 field calibration. These results are based on the Version 3 Level 2.0 data set in which the Level 1.5 algorithm scans
1110 the entire deployment. The AOD difference histograms were computed for optical air mass ranges ($1.0 \leq m < 7.0$ and
1111 $1.0 \leq m < 1.5$). The optical air mass $1.0 \leq m < 7.0$ range includes all of the data; however, these AOD difference
1112 magnitudes will be constrained by the improved AOD measurements at large optical air mass and influenced toward
1113 Northern hemisphere winter mid-latitude sites when AOD tends to be low. The optical air mass $1.0 \leq m < 1.5$ range
1114 includes data will provide AOD measurements near solar noon and these measurements are generally less accurate
1115 ($\delta\tau * m$) than at larger optical air mass. In addition, optical air mass $1.0 \leq m < 1.5$ range data include a greater influence
1116 of tropical locations and data from the mid-latitude summer when AOD tends to be moderate to high.

1117

1118 Figure 19 shows the AOD average differences for the $1.0 \leq m < 7.0$ range indicate a positive bias in which the AOD
1119 for the pre-field only calibration tends to be on average +0.003 to +0.009 higher than the AOD using the
1120 interpolated calibration. Similarly, AOD average differences for the $1.0 \leq m < 1.5$ range show a positive bias and
1121 similar wavelength variations but up to two times larger differences than for the $1.0 \leq m < 7.0$ range. The largest
1122 average differences and standard deviations are for the UV wavelengths, which have greater uncertainty as
1123 discussed in Sect. 2. The AOD differences for the wavelengths longer than 500nm have about less than half the bias
1124 of the UV wavelengths. The Level 1.5 algorithm performance improves with increased data availability such as a
1125 greater number of wavelength or number of days. When an instrument deployment begins, some of the Level 1.5
1126 algorithm steps such as multi-day removal schemes are not available until several days into the deployment
1127 producing larger differences in the near real-time AOD with respect to the final product. While wavelength
1128 dependent biases of +0.003 to +0.009 for the $1.0 \leq m < 7.0$ range and +0.006 to +0.015 for the $1.0 \leq m < 1.5$ range exist
1129 when only the pre-field calibration is applied, the difference can vary significantly depending on each instrument
1130 deployment necessitating continued post-field calibration and maintenance effort.

1131

When an instrument is deployed in the field, the pre-field calibration is used constantly until the post-field calibration is assessed and applied to the data using linear interpolation. The difference of pre-field calibration AOD minus the post-field calibration AOD average difference and standard deviation are computed in day bins for the number of days since the pre-field calibration. Figure 20 shows the AOD 500nm average difference for the optical air mass ranges: $1.0 \leq m < 7.0$ and $1.0 \leq m < 1.5$. Instruments typically operate in the field between 12 and 18 months from the pre-field calibration date; however, the instrument deployment may be delayed and the instrument may not begin operation for a few months after the pre-field calibration. Thus, the number of AOD measurements in the days since pre-field calibration bins increase to a maximum at about 100 days. Some instruments may operate longer in the field to support field campaigns and other scientific priorities. Figure 20 shows that the AOD average difference and the standard deviation slowly but steadily increase for each optical air mass range. At about 1.5 years after pre-field calibration (~550 days), the AOD average difference is about +0.010 with a standard deviation of 0.015 for optical air mass $1.0 \leq m < 7.0$ range and +0.017 with a standard deviation of 0.021 for $1.0 \leq m < 1.5$. For the UV wavelengths, the average differences and standard deviations tend to increase slightly while the longer visible and near infrared wavelengths tend to decrease slightly. Therefore, the quality of the Level 1.5 near real-time AOD changes with time with high quality data at the start of the deployment but up to a +0.02 bias and 0.02 uncertainty for data collected more than 1.5 years since pre-field calibration.

4.3   Multi-year Monthly Comparisons of Version 3 Level 2.0 to Version 2 Level 2.0 Databases

Long-term average differences between the Version 3 and Version 2 Level 2.0 data sets provide insight into the changes to be expected across most AERONET sites. The analysis of the Version 3 and Version 2 data sets shows mainly the differences in the AOD, $AE_{440-870nm}$, precipitable water (PW) in cm, and the number of days are clustered near zero (Fig. 21). Note that precipitable water data quality depends on the quality of the input wavelengths (675nm and 870nm) and no further quality control is made on the 935nm wavelength. The increases in the Version 3 Level 2.0 multi-year monthly average AOD are often due to the increased presence of fine mode particles from high aerosol loading events as well as aerosols in near cloud environments (Eck et al., 2018). The decrease in the multi-year monthly average AOD is due to the improved removal of clouds in the Version 3 quality control algorithm. Generally, the results should be very similar between Version 3 and Version 2 in AOD calculation since the temperature characterizations as well as NO2 absorption contributions typically have relatively minor contributions.

Other factors affecting the AOD calculation include the adjustment of site coordinates and elevation information for about 100 AERONET sites utilizing GPS or digital elevation model. A few rare extreme coordinate adjustments of more than 25 km included Petrolina_SONDA (9.0691° S, 40.3201° W), Ilorin (8.4841° N, 4.6745° E), and Ouagadougou (12.4241° N, 1.4872° W). A large site coordinate adjustment can complicate satellite matchups for these few cases but the review of all AERONET sites showed that less than a 5 km distance adjustment and less than 100-meter elevation adjustment was needed for most of these 100 suspected sites.

1168   Figure 22 shows similar plots to Fig. 21 except that the observations used for the multi-year monthly averages in

1169   both data sets the instantaneous observations are time matched, hence, each data set has the same number of

1170   observations and number of days. The time matched long-term average comparison provides insight into the AOD

1171   calculation differences rather than impacts due to cloud screening and instrument quality controls applied in Level

1172   1.5. Table 5 shows the multi-year monthly overall standard deviation and AOD maximum to minimum range is

1173   significantly reduced compared to the data set without time-matched observations. Figure 22a shows a slight

1174   decreasing trend of Version 3 AOD for increasing Version 2 AOD and most of the larger AOD deviations are for

1175   sites in Asia where the impact of the OMI NO2 corrections may be contributing to the slight shift of up to 0.02 for a

1176   few months and sites.

1177

1178   For unmatched or time matched data sets in Table 5, the precipitable water climatology changed on average

1179   insignificantly. The multi-year monthly overall days difference (Table 5) for the unmatched precipitable water data

1180   set was near zero and the standard deviation was near 25 days while the maximum of +150 and minimum of −130

1181   days indicate significant variability due to the differences in quality controls between the algorithms. Overall, the

1182   changes from Version 2 to Version 3 in precipitable water are generally negligible in terms of the contribution to the

1183   calculation of the AOD.

1184

1185   Overall, the multi-year monthly overall average difference between Version 3 and Version 2 for unmatched data is

1186   +0.002 and time matched data is −0.002 indicating remarkable consistency between the long-term average quality

1187   assured data sets. For example, the NASA GSFC AERONET site multi-year monthly average (Fig. 23) located 20

1188   km north of Washington, D.C., shows minor variations in the AOD and increase in AE due to removal of cirrus

1189   clouds during the winter months and increasing AOD in the summer months due to the greater abundance of cloud

1190   processed or near cloud aerosols (Eck et al., 2014).

1191

1192   Comparison of $AE_{440–870nm}$ in Fig. 21b and Fig. 22b show significantly lower values for Version 3 than Version 2

1193   Level 2.0 at low optical depth. An analysis of long-term average data at Lulin, Taiwan (23.47° N, 120.87° E)

1194   identified significant reduction of Version 3 AE relative to Version 2 AE at very low AOD due to temperature

1195   characterization that resulted in improved AOD spectral dependence (Fig. 24). The Lulin site is a high altitude

1196   mountain station located in south central Taiwan, and this site is affected episodically by trans-boundary aerosol

1197   plumes from East and Southeast Asia (Lin et al., 2013; Wang et al., 2013). In eastern China, multi-year monthly

1198   averages from the XiangHe site (39.75° N, 116.96° E) show a significant Version 3 AOD increase of 0.2, while

1199   maintaining nearly the same AE and increasing the number of days up to near 40% for the multi-year monthly

1200   average in July and August (Fig. 25). The XiangHe site is located to the east of Beijing and is routinely impacted by

1201   urban pollution and episodically by biomass burning and desert dust events (Li et al., 2007). The significant

1202   increase in the AOD for XiangHe is likely due to the retention of highly variable fine mode aerosol events

1203   particularly at very high AOD, which were removed by the Version 2 cloud screening wavelengths utilizing large

1204   triplets less than 675nm (Eck et al., 2018). Additionally, some very high AOD events at XiangHe were previously

1205 removed by the Version 2 mid-visible low signal threshold but are now retained in Version 3, but often only for
1206 wavelengths longer than 675nm, so the statistics for these days are not accounted for in the 500nm data shown in
1207 Fig. 25.

1208

1209 At the Mongu (15.25° S, 23.15° E) site (Fig. 26), the biomass burning smoke typically occurs during the dry season
1210 from April through November due to biomass fuel cooking and agricultural burning (Eck et al., 2003). Comparisons
1211 of multi-year monthly averages for the Mongu site shows small deviations for AOD up to ±0.01 with slight
1212 increases in Version 3 AE during December through March due to enhanced cirrus cloud removal from the solar
1213 aureole check. Notably, the number of days for the Mongu multi-year monthly averages significantly decreased by
1214 10% to 25% in Version 3 due to improved cloud screening and sensor head temperature anomalies affecting
1215 instrument performance. In Cinzana, Mali (Fig. 27), the aerosol loading is dominated by background dust aerosol
1216 with episodic contributions to the aerosol loading from biomass burning smoke from November to March (Cavalieri
1217 et al., 2010). The AERONET IER-Cinzana site (13.28° N, 5.93° W) multi-year monthly averages show generally
1218 0.03 lower AOD for Version 3 than Version 2 and nearly the same AE for both versions. The number of days for
1219 each month is 7% to 25% lower in Version 3 when compared to Version 2 mainly due to improved cirrus cloud
1220 screening.

1221 **5   Summary**
1222

1223 The Aerosol Robotic Network (AERONET) has adopted a new automated quality assurance algorithm called
1224 Version 3. The significant impacts of the Version 3 algorithm are updated and improved cloud screening and
1225 quality control methods, which are powerful tools in quality assuring the Sun photometer AOD data. Comparisons
1226 between the quality assured data sets of Version 3 and Version 2 show excellent agreement. Deviations can be
1227 explained by known algorithm differences such as changes in the cloud screening triplet variability, cirrus cloud
1228 detection and removal, implementation of temperature characterization, updates to NO_2 climatology, modification of
1229 site coordinates and elevation, and identification of instrument anomalies such as aerosol optical depth (AOD)
1230 diurnal dependence, AOD spectral dependence, and instrument electrical and temperature stability. The high
1231 statistical agreement in multi-year monthly averaged AOD substantiates Version 3 algorithms and suggests that the
1232 Version 3 database will validate most Version 2 research conclusions but exceptions can exist. For example, the
1233 Version 3 algorithm permitted AOD measurements of thick biomass burning smoke in Indonesia during the strong
1234 2015 El Nino event where Version 2 AOD data were not available (Eck et al., 2019). As a result, MODIS satellite
1235 retrieval modifications have been identified to capture more high optical depth events rather than masking them as
1236 clouds (Shi et al., 2018). Given AERONET algorithm enhancements, we recommend the Version 3 AOD database
1237 for scientific investigations.

1238

1239 Major highlights of this work include (not listed in priority):

1240   1. An automatic quality control algorithm significantly reduces the necessity of analysts to inspect millions of AERONET measurements. The AERONET Version 3 algorithm applied in near real-time provides high quality AOD for data assimilation applications. The Version 3 Level 2.0 data is provided within 30 days of the post-field calibration evaluation after the instrument deployment, improving the timeliness of quality assured data.

1245   2. Improvements to the total AERONET database cloud screening results in about 60% removal of clouds from the complete Sun photometer database and this value is similar to the coverage of clouds globally of about 68% (Rossow and Schiffer 1999). Autonomous Cimel Sun photometers can view gaps and nearby regions of the clouds and become inactive during rain periods due to wet sensor activation and AERONET sites are dominated by land locations which generally have lower cloud cover on average; therefore, these factors would reduce the difference between total AERONET cloud removal percentage and global satellite observations. Over 36% of the total data were removed by the 4-quadrant solar tracker sensitivity check due to less accuracy in tracking the Sun in cloudy conditions, while about 23% of the removal was due to the variability of clouds with respect to more homogeneous aerosol loading.

1254   3. Utilizing the shape of the solar aureole radiances with scattering angle, a cirrus detection algorithm was developed by leveraging MPLNET LIDAR cloud detection capabilities. The solar aureole cirrus algorithm eliminates ~5% of the Level 1.0 AOD data to reduce the bias of optically thin cirrus clouds in AERONET database.

1258   4. Spectral temperature correction has been implemented for all AERONET instruments using the sensor head temperature sensor reading. The temperature characterization shows significant AOD deviation ±0.01 variation between −25°C and +50°C for the Silicon 1020nm, since this wavelength is on the edge of the Silicon detector sensitivity range. Other wavelengths in the 440nm to 1640nm range have weak temperature dependence from −25°C and +30°C with a few wavelengths having greater temperature dependence at higher temperatures.

1264   5. New automated instrument anomaly screening provides a systematic and objective scheme to remove entire measurements or individual wavelengths from the AERONET AOD database. Importantly, obstructions to the instrument optics are now removed automatically using an AOD diurnal dependence algorithm based on the optical air mass. The AOD diurnal dependence technique employs several conditions that were developed to mitigate the removal of true diurnal dependence conditions while maximizing the removal of data significantly impacted by anomalies affecting the instrument optics.

1270   6. Bias and uncertainty estimates for near real-time AOD are computed by using the difference of the pre-field calibration AOD minus the interpolated calibration AOD. The near-real time AERONET data have an estimated bias up to +0.02 and one-sigma uncertainty up to 0.02; these values have slightly higher uncertainty for shorter wavelengths and slightly lower uncertainty for longer wavelengths.

1274   7. The AERONET Version 3 and Version 2 AOD quality controlled databases are analyzed to have a long-term monthly average difference of +0.002 with ±0.02 standard deviation and greater agreement for time-matched observations with average difference of −0.002 with ±0.004 standard deviation. The high

1277   statistical agreement in multi-year monthly averaged AOD validates the advanced automatic data quality

1278   control algorithms and suggests that migrating research to the Version 3 database will corroborate most

1279   Version 2 research results and likely lead to some more accurate results.

1280   8. Examination of long-term sites in various aerosol source regions indicates mainly subtle changes in AOD,

1281   AE and the number of days available; however, in some months, improved cloud screening, high aerosol

1282   loading retention, and improved instrument anomaly screening not attained by Version 2 explain larger

1283   deviations in these parameters.

1284

1285 AERONET Version 3 has evolved into a database with unparalleled presence in Sun photometry. Future algorithms

1286 could include improvements to the detection of cirrus clouds in polar environments, where the ice crystal size is

1287 approaching the size of large non-cloud aerosols, the determination of anomalies in high aerosol loading conditions,

1288 and the identification of true AOD diurnal dependence versus one generated by an instrument anomaly. Cimel

1289 radiometers will also measure the moon to derive lunar AOD (Berkoff et al., 2011; Barreto et al, 2013, 2016; Li et

1290 al., 2016). For example, current lunar measurement protocols do not include lunar aureole measurements analogous

1291 to the solar aureole measurements, hence the lack of these measurements potentially reduces the ability of the

1292 algorithm to remove cirrus clouds at night, and thus a variation of the quality control methodology may need to be

1293 developed. Other surface-based remote sensing networks such as MAN (Smirnov et al., 2009), SKYNET

1294 (Takamura and Nakajima 2004), GAW-PFR (Kazadzis et al., 2018), and PANDORA (Herman et al., 2009) may

1295 benefit by implementing applicable quality control methods established by AERONET.

1296

1297 *Data Availability*. Version 3 AOD data are available from the AERONET web site (https://aeronet.gsfc.nasa.gov)

1298 and the web site provides these data freely to the public. Data may be acquired by utilizing several download

1299 mechanisms including site-by-site download tools and web service options for near real-time data acquisition.

1300

1301 *Author contributions*. For five years, the AERONET staff (listed from DG to BH) worked individually and

1302 collaboratively drawing on their decades of project scientific, engineering and programming expertise to develop

1303 and assess the Version 3 AOD processing system presented herein. Traditional assignment of co-authorship is not

1304 possible. Aside from the first author, contributing AERONET staff is listed in reverse chronological order based on

1305 their start date with the project. JL, JC, and EW provided LIDAR data for development of the cirrus curvature

1306 methodology. SK and AL provided gaseous and water vapor absorption coefficients based on radiative transfer

1307 models.

1308

1309 *Competing interests:* The authors declare that they have no conflict of interest.

1310

1311 *Acknowledgements*. The AERONET and MPLNET projects at NASA GSFC are supported by the Earth Observing

1312 System Program Science Office Cal-Val, Radiation Science program at NASA headquarters, and various field

1313 campaigns. NCEP Reanalysis data are obtained routinely from the U.S. National Weather Service Climate

1314   Prediction Center. We would like to thank Edward Celarier for several discussions and providing the OMI NO_2

1315   monthly climatology. Fred Espenak and Chris O'Byrne (NASA GSFC) provided solar and lunar eclipse predictions

1316   and the Eclipse Explorer software.

1317

1318   We thank the MPLNET PIs for their effort in establishing and maintaining the sites: Arnon Karnieli

1319   (SEDE_BOKER); Sachi Tripathi (Kanpur); Greg Schuster (COVE); Margarita Yela Gonzalez (Santa Cruz

1320   Tenerife); and John Barnes (Trinidad Head).

1321

1322   The authors thank the AERONET calibration facilities in the USA (NASA GSFC, NOAA Mauna Loa Observatory,

1323   and NEON), France (PHOTONS), and Spain (RIMA and Izana). We thank the following AERONET PIs and their

1324   staff for maintaining the sites and contributing aerosol data: Norm O'Neill, Ihab Abboud and Vitali Fioletov

1325   (PEARL, Toronto, Bratts Lake); Itaru Sano (Osaka); Paulo Artaxo (Rio Branco); Neng-Huei Lin (Lulin); Pucai

1326   Wang and Xiangao Xia (XiangHe); Mikhail Panchenko (Ussurisyk); Arnon Karnieli (SEDE BOKER); Emilio

1327   Cuevas-Agullo (Santa Cruz Tenerife); Joseph Prospero (Ragged Point); Soo-Chin Liew and Santo Salinas Cortijo

1328   (Singapore); S. N. Tripathi (Kanpur); Francisco Reyes (Malaga); and Jean Rajot and Beatrice Marticorena (IER-

1329   Cinzana). A special acknowledgement is given to the AERONET principal investigators and their site staff around

1330   the world who participate in monitoring aerosols to expand our scientific understanding of the Earth.

References

Alexandrov, M. D., Schmid, B., Turner, D. D., Cairns, B., Oinas, V., Lacis, A. A., Gutman, S. I., Westwater, E. R., Smirnov, A., and Eilers, J.: Columnar water vapor from multifilter rotating shadowband radiometer data, J. Geophys, Res., 114, D02306, https://doi.org/10.1029/2008JD010543, 2009.

Andrews, E., Ogren, J. A., Kinne, S., and Samset, B.: Comparison of AOD, AAOD and column single scattering albedo from AERONET retrievals and in situ profiling measurements, Atmos. Chem. Phys., 17, 6041-6072, https://doi.org/10.5194/acp-17-6041–2017, 2017.

Ångstrom, A.: Apparent solar constant variations and their relation to variability of atmospheric transmission, Tellus. 22, 205-218, https://doi.org/10.3402/tellusa.v22i2.10215, 1970.

Arola, A. and Koskela T.: On the sources of bias in aerosol optical depth retrieval in the UV range, J. Geophys. Res., 109, D08209, https://doi.org/10.1029/2003JD004375, 2004.

Barreto, A., Cuevas, E., Damiri, B., Guirado, C., Berkoff, T., Berjón, A. J., Hernández, Y., Almansa, F., and Gil, M.: A new method for nocturnal aerosol measurements with a lunar photometer prototype, Atmos. Meas. Tech., 6, 585-598, https://doi.org/10.5194/amt-6-585-2013, 2013.

Barreto, Á., Cuevas, E., Granados-Muñoz, M.-J., Alados-Arboledas, L., Romero, P. M., Gröbner, J., Kouremeti, N., Almansa, A. F., Stone, T., Toledano, C., Román, R., Sorokin, M., Holben, B., Canini, M., and Yela, M.: The new sun-sky-lunar Cimel CE318-T multiband photometer – a comprehensive performance evaluation, Atmos. Meas. Tech., 9, 631-654, https://doi.org/10.5194/amt-9-631-2016, 2016.

Berkoff, T.A., Sorokin, M., Stone, T., Eck, T.F., Hoff, R., Welton, E., and Holben, B.: Nocturnal Aerosol Optical Depth Measurements with a Small-Aperture Automated Photometer Using the Moon as a Light Source. J. Atmos. Ocean. Tech., 28, 1297–1306, https://doi.org/10.1175/JTECH-D-10-05036.1, 2011.

Bock, O., Bosser, P., Bourcy, T., David, L., Goutail, F., Hoareau, C., Keckhut, P., Legain, D., Pazmino, A., Pelon, J., Pipis, K., Poujol, G., Sarkissian, A., Thom, C., Tournois, G., and Tzanos, D.: Accuracy assessment of water vapour measurements from in situ and remote sensing techniques during the DEMEVAP 2011 campaign at OHP, Atmos. Meas. Tech., 6, 2777-2802, https://doi.org/10.5194/amt-6-2777-2013, 2013.

Bodhaine, B. A., Wood, N. B., Dutton, E. G., Slusser, J. R.: On Rayleigh Optical Depth Calculations, J. Atmos. Ocean. Tech., 16, 1854-1861, https://doi.org/10.1175/1520-0426(1999)016%3C1854:ORODC%3E2.0.CO;2, 1999.

Boersma, K. F., H. J. Eskes, and E. J. Brinksma: Error analysis for tropospheric NO2 retrieval from space, J. Geophys. Res., 109, D04311, https://doi.org/10.1029/2003JD003962, 2004.

Boersma, K. F., Jacob, D. J., Eskes, H. J., Pinder, R. W., Wang, J., and van der A, R. J.: Intercomparison of SCIAMACHY and OMI tropospheric NO2 columns: Observing the diurnal evolution of chemistry and emissions from space, J. Geophys. Res., 113, D16S26, https://doi.org/10.1029/2007JD008816, 2008.

Bokoye, A. I., Royer, A., O'Neill, N. T., Cliche, P., Fedosejevs, G.,Teillet, P. M., and McArthur, L. J. B.: Characterization of atmospheric aerosols across Canada from a ground-based sunphotometer network: AEROCAN, Atmosphere-Ocean, 39:4, 429-456,: https://doi.org/10.1080/07055900.2001.9649687, 2001.

Bokoye, A. I., Royer, A., O'Neill, N. T., Cliché, P., McArthur, L. J. B., Teillet, P. M., Fedosejevs, G., and Thériault, J.-M.: Multisensor analysis of integrated atmospheric water vapor over Canada and Alaska, J. Geophys. Res., 108, 4480, doi: 10.1029/2002JD002721, D15, 2003.

Bruegge, C. J., Conel, J. E., Green, R. O., Margolis, J. S., Holm, R. G., and Toon, G.: Water vapor column abundance retrievals during FIFE, J. Geophys. Res., 97(D17), 18759–18768, https://doi.org/10.1029/92JD01050, 1992.

Burrows, J. P., Dehn, A., Deters, B., Himmelmann, S., Richter, A., Voigt, S. and Orphal, J.: Atmospheric Remote-Sensing Reference Data from GOME: Part 1. Temperature-Dependent Absorption Cross-sections of NO2 in the 231-794 nm Range, JQSRT, 60, 1025–1031, https://doi.org/10.1016/S0022-4073(97)00197-0, 1998.

Burrows, J. P., Richter, A., Dehn, A., Deters, B., Himmelmann, S., Voigt, S. and Orphal J.: Atmospheric remote-sensing reference data from GOME – 2. Temperature-dependent absorption cross sections of O_3 in the 231-794 nm range, J. Quant. Spectrosc. Ra., 61, 509–517, https://doi.org/10.1016/S0022-4073(98)00037-5, 1999.

Cachorro, V. E., Romero, P. M., Toledano, C., Cuevas, E., and de Frutos, A. M.: The fictitious diurnal cycle of aerosol optical depth: A new approach for ''in situ'' calibration and correction of AOD data series, Geophys. Res. Lett., 31, L12106, https://doi.org/10.1029/2004GL019651, 2004.

Campbell, J.R., Hlavka, D. L., Welton, E. J., Flynn, C. J., Turner, D. D., Spinhirne, J. D., Scott, V.S., and Hwang, I.H.: Full-time, Eye-Safe Cloud and Aerosol Lidar Observation at Atmospheric Radiation Measurement Program Sites: Instrument and Data Processing, J. Atmos. Ocean. Tech., 19, 431-442, https://doi.org/10.1175/1520-0426(2002)019%3C0431:FTESCA%3E2.0.CO;2, 2002.

Campbell, J. R., Vaughan, M. A., Oo, M., Holz, R. E., Lewis, J. R., and Welton, E. J.: Distinguishing cirrus cloud presence in autonomous lidar measurements, Atmos. Meas. Tech., 8, 435–449, https://doi.org/10.5194/amt-8-435-2015, 2015.

Campanelli, M., Mascitelli, A., Sanò, P., Diémoz, H., Estellés, V., Federico, S., Iannarelli, A. M., Fratarcangeli, F., Mazzoni, A., Realini, E., Crespi, M., Bock, O., Martínez-Lozano, J. A., and Dietrich, S.: Precipitable water vapour content from ESR/SKYNET sun–sky radiometers: validation against GNSS/GPS and AERONET over three different sites in Europe, Atmos. Meas. Tech., 11, 81-94, https://doi.org/10.5194/amt-11-81-2018, 2018.

Cavalieri, O., Cairo, F., Fierli, F., Di Donfrancesco, G., Snels, M., Viterbini, M., Cardillo, F., Chatenet, B., Formenti, P., Marticorena, B., and Rajot, J. L.: Variability of aerosol vertical distribution in the Sahel, Atmos. Chem. Phys., 10, 12005–12023, https://doi.org/10.5194/acp-10-12005-2010, 2010.

Che, H., Zhang, X.-Y., Xia, X., Goloub, P., Holben, B., Zhao, H., Wang, Y., Zhang, X.-C., Wang, H., Blarel, L., Damiri, B., Zhang, R., Deng, X., Ma, Y., Wang, T., Geng, F., Qi, B., Zhu, J., Yu, J., Chen, Q., and Shi, G.: Ground-based aerosol climatology of China: aerosol optical depths from the China Aerosol Remote Sensing Network (CARSNET) 2002–2013, Atmos. Chem. Phys., 15, 7619-7652, https://doi.org/10.5194/acp-15-7619-2015, 2015.

1403 Chew, B. N., Campbell, J. R., Reid, J. S., Giles, D. M., Welton, E. J., Salinas, S. V., and Liew, S. C.: Tropical cirrus
1404   cloud contamination in sun photometer data, Atmos. Environ., 45, 6724–6731,
1405   https://doi.org/10.1016/j.atmosenv.2011.08.017, 2011.

1406 Clough, S. A., F. X. Kneizys, and R. W. Davies: Line shape and the water vapor continuum, Atmos. Res., 23, 229–
1407   241, https://doi.org/10.1016/0169-8095(89)90020-3, 1989.

1408 Coddington, Lean, O., J., Pilewskie, P., Snow, M., and Lindholm, D.: A solar irradiance climate data record, Bull.
1409   Amer. Meteor. Soc., https://doi.org/10.1175/BAMS-D-14-00265.1, 2016.

1410 DeVore, J.G., Stair, A.T., LePage, A., Rall, D., Atkinson, J., Villanucci, D., Rappaport, S.A., Joss, P.C., and
1411   McClatchey, R.A.: Retrieving Properties of Thin Clouds from Solar Aureole Measurements. J. Atmos.
1412   Oceanic Technol., 26, 2531–2548, https://doi.org/10.1175/2009JTECHA1289.1, 2009.

1413 DeVore, J. G., Stair Jr., A. T., LePage, A. J., and Villanucci, D.: Using scattering calculations to compare MODIS
1414   retrievals of thin cirrus optical properties with SAM solar disk and aureole radiance measurements, J.
1415   Geophys. Res., 117, D01204, https://doi.org/10.1029/2011JD015858, 2012.

1416 Dubovik, O. V, Lapyonok, T. V. and Oshchepkov, S. L.: Improved technique for data inversion: optical sizing of
1417   multicomponent aerosols, Appl.Opt., 34, 8422-8436, https://doi.org/10.1364/AO.34.008422, 1995.

1418 Dubovik, O. and King, M. D.: A flexible inversion algorithm for retrieval of aerosol optical properties from Sun and
1419   sky radiance measurements, J. Geophys. Res., 105, 20 673–20 696, https://doi.org/10.1029/2000JD900282,
1420   2000.

1421 Eck, T. F., Holben, B. N., Reid, J. S., Dubovik, O., Smirnov, A., O'Neill, N. T., Slutsker, I., and Kinne, S.:
1422   Wavelength dependence of the optical depth of biomass burning, urban, and desert dust aerosols, J.
1423   Geophys. Res., 104(D24), 31333–31349, https://doi.org/10.1029/1999JD900923, 1999.

1424 Eck, T. F., Holben, B. N., Reid, J. S., Arola, A., Ferrare, R. A., Hostetler, C. A., Crumeyrolle, S. N., Berkoff, T. A.,
1425   Welton, E. J., Lolli, S., Lyapustin, A., Wang, Y., Schafer, J. S., Giles, D. M., Anderson, B. E., Thornhill, K.
1426   L., Minnis, P., Pickering, K. E., Loughner, C. P., Smirnov, A., and Sinyuk, A.: Observations of rapid
1427   aerosol optical depth enhancements in the vicinity of polluted cumulus clouds, Atmos. Chem. Phys., 14,
1428   11633–11656, doi: 10.5194/acp-14-11633-2014, 2014.

1429 Eck, T. F., Holben, B. N., Reid, J. S., Xian, P., Giles, D. M., Sinyuk, A., Smirnov, A., Schafer, J. S., Slutsker, I.,
1430   Kim, J., Koo, J.-H., Choi, M., Kim, K. C., Sano, I., Arola, A., Sayer, A. M., Levy, R. C., Munchak, L. A.,
1431   O'Neill, N. T., Lyapustin, A., Hsu, N. C., Randles, C. A., Da Silva, A. M., Buchard, V., Govindaraju, R.
1432   C., Hyer E., Crawford, J. H., Wang, P., and Xia, X.: Observations of the interaction and transport of fine
1433   mode aerosols with cloud and/or fog in Northeast Asia from Aerosol Robotic Network and satellite remote
1434   sensing, J. Geophys. Res. Atmos., 123, 5560–5587. https://doi.org/10.1029/2018JD028313, 2018.

1435 Eck, T. F., Holben, B. N., Giles, D. M., Slutsker, I., Sinyuk, A., Schafer, J. S., Smirnov, A., Sorokin, M., Reid, J. S.,
1436   Sayer, A. M., Hsu, N. C., Shi, Y. R., Levy, R. C., Lyapustin, A., Rahman, M. A., Liew, S.-C., Cortijo, S. V.
1437   S., Li, T., Kalbermatter, D., Keong, K. L., Elifant, M., Aditya, F., Mohamad, M., Mahmud, M., Chong, T.
1438   K., San, L. H., Choon, Y. E., Deranadyan, G., Kusumaningtyas, S. D. A., and Aldrian, E.: AERONET

1439   remotely sensed measurements and retrievals of biomass burning aerosol optical properties during the 2015

1440   Indonesian burning season, J. Geophys. Res., in review, 2019.

1441 Eiden R.: Calculations and measurements of the spectral radiance of the solar aureole, Tellus, 20:3, 380–399, doi:

1442   10.3402/tellusa.v20i3.10017, 1968.

1443 Espenak, F., and Meeus, J.: Five Millennium Cannon of Solar Eclipses: −1999 to +3000 (2000 BCE to 3000 CE),

1444   NASA Technical Publication TP-2006-214141, NASA, Greenbelt, MD, 2006.

1445 Gamache, R. R., Roller, C., Lopes, E., Gordon, I. E., Rothman, L. S., Polyansky, O. L., Zobov, N. F., Kyuberis, A.

1446   A., Tennyson, J., Yurchenko, S. N., Csaszar, A. G., Furtenbacher, T., Huang, X., Schwenke, D. W., Lee, T.

1447   J., Drouin, B. J., Tashkun, S. A., Perevalov, V. I., Kochanov, R. V.: Total internal partition sums for 166

1448   isotopologues of 51 molecules important in planetary atmospheres: Application to HITRAN2016 and

1449   beyond, J. Quant. Spectrosc. Ra., https://doi.org/10.1016/j.jqsrt.2017.03.045, 2017.

1450 Giles, D. M., Holben, B. N., Eck, T. F., Sinyuk, A., Smirnov, A., Slutsker, I., Dickerson, R. R., Thompson, A. M.,

1451   and Schafer, J. S.: An analysis of AERONET aerosol absorption properties and classifications

1452   representative of aerosol source regions, J. Geophys. Res., 117, D17203,

1453   https://doi.org/10.1029/2012JD018127, 2012.

1454 Goloub, P., Li, Z., Dubovik, O., Blarel, L., Podvin, T., Jankowiak, I., Lecoq, R., Deroo, C., Chatenet, B., Morel, J.

1455   P., Cuevas, E., and Ramos, R.: PHOTONS/AERONET sunphotometer network overview: description,

1456   activities, results, Proc. SPIE, 6936, 69360V, https://doi.org/10.1117/12.783171, 2008.

1457 Haapanala, P., Räisänen, P., McFarquhar, G. M., Tiira, J., Macke, A., Kahnert, M., Nousiainen, T.: Disk and

1458   circumsolar radiances in the presence of ice clouds, Atmos. Chem. Phys., 17(11), 6865–6882, doi:

1459   https://dx.doi.org/10.5194/acp-17-6865-2017, 2017.

1460 Halthore, R. N., Eck, T. F., Holben, B. N., and Markham, B. L.: Sun photometric measurements of atmospheric

1461   water vapor column abundance in the 940-nm band, J. Geophys. Res., 102(D4), 4343–4352,

1462   https://doi.org/10.1029/96JD03247, 1997.

1463 Hamonou, Chazette, E., P., Balis, D., Dulac, F., Schneider, X., Galani, E., Ancellet, G., and Papayannis, A.:

1464   Characterization of the vertical structure of Saharan dust export to the Mediterranean basin, J. Geophys.

1465   Res., 104(D18), 22257–22270, https://doi.org/10.1029/1999JD900257, 1999.

1466 Herman, J., Cede, A., Spinei, E., Mount, G., Tzortziou, M., and Abuhassan, N.: NO2 column amounts from ground-

1467   based Pandora and MFDOAS spectrometers using the direct-sun DOAS technique: Intercomparisons and

1468   application to OMI validation, J. Geophys. Res., 114, D13307, https://doi.org/10.1029/2009JD011848,

1469   2009.

1470 Holben, B. N., Vermote, E., Kaufman, Y. J., Tanre, D. and Kalb, V.: Aerosol retrieval over land from AVHRR data-

1471   application for atmospheric correction, IEEE T. Geosci. Remote, 30, 212–222,

1472   https://doi.org/10.1109/36.134072, 1992.

1473 Holben, B. N., Eck, T. F., Slutsker, I., Tanre, D., Buis, J. P., Setzer, A., Vermote, E., Reagan, J. A., Kaufman, Y.,

1474   Nakajima, T., Lavenue, F., Jankowiak, I., and Smirnov, A.: AERONET–A federated instrument network

1475   and data archive for aerosol characterization, Remote Sens. Environ., 66, 1–16,
1476   https://doi.org/10.1016/S0034-4257(98)00031-5, 1998.

1477   Holben, B. N., Tanre, D., Smirnov, A., Eck, T. F., Slutsker, I., Abuhassan, N., Newcomb, W. W., Schafer, J.,
1478   Chatenet, B,. Lavenue, F., Kaufman, Y., Vande Castle, J., Setzer, A., Markham, B., Clark, D., Frouin, R.,
1479   Halthore, R., Karnieli, A., O'Neill, N. T., Pietras, C., Pinker, R. T., Voss, K. and Zibordi, G.: An emerging
1480   ground-based aerosol climatology: Aerosol optical depth from AERONET, J. Geophys. Res., 106(D11),
1481   12,067–12,097, https://doi.org/10.1029/2001JD900014, 2001.

1482   Holben, B. N., Eck, T. F., Slutsker, I., Smirnov, A., Sinyuk, A, Schafer, J., Giles, D., and Dubovik, O.: Aeronet's
1483   Version 2.0 quality assurance criteria, Proc. SPIE, 6408, Conf. on Remote Sensing of the Atmosphere and
1484   Clouds, 64080Q, https://doi.org/10.1117/12.706524, 2006.

1485   Huang, J., Hsu, N., Tsay, S.-C., Jeong, M.-J., Holben, B. N., Berkoff, T. A., and Welton, E. J.: Susceptibility of
1486   aerosol optical thickness retrievals to thin cirrus contamination during the BASE-ASIA campaign, J.
1487   Geophys. Res., 116, D08214, https://doi.org/10.1029/2010JD014910, 2011.

1488   Ingold, T., Schmid, B., Mätzler, C., Demoulin, P., and Kämpfer, N.: Modeled and empirical approaches for
1489   retrieving columnar water vapor from solar transmittance measurements in the 0.72, 0.82 and 0.94-mm
1490   absorption bands, J. Geophys. Res., 105, 24,327–24,343, https://doi.org/10.1029/2000JD900392, 2000.

1491   Kahn, R. A., and Gaitley, B. J.: An analysis of global aerosol type as retrieved by MISR, J. Geophys. Res. Atmos.,
1492   120, 4248–4281, https://doi.org/10.1002/2015JD023322, 2015.

1493   Kasten, F.: A new table and approximation formula for relative optical air mass, Arch. Meteorol. Geophys.
1494   Bioklimatol. Ser. B, 14, 206–223, https://doi.org/10.1007/BF02248840, 1965.

1495   Kasten, F. and Young, A. T.: Revised optical air mass tables and approximation formula, Appl. Opt., 28, 4735–
1496   4738, https://doi.org/10.1364/AO.28.004735, 1989.

1497   Kalnay, E., Kanamitsu, M., Kistler, R., Collins, W., Deaven, D., Gandin, L., Iredell, M., Saha, S., White, G.,
1498   Woollen, J., Zhu, Y., Chelliah, M., Ebisuzaki, W., Higgins, W., Janowiak, J., Mo, K. C., Ropelewski, C.,
1499   Wang, J., Leetmaa, A., Reynolds, R., Jenne, R. and Joseph, D.: The NCEP/NCAR 40-Year Reanalysis
1500   Project, Bull. Amer. Meteor. Soc., 77, 437–471, https://doi.org/10.1175/1520-
1501   0477(1996)077%3C0437:TNYRP%3E2.0.CO;2, 1996.

1502   Kaufman, Y. J., and Tanré, D.: Strategy for direct and indirect methods for correcting the aerosol effect on remote
1503   sensing: From AVHRR to EOS-MODIS, Rem. Sens. Environ., 55, 1, 65–79, https://doi.org/10.1016/0034-
1504   4257(95)00193-X, 1996.

1505   Kaufman, Y. J., Remer, L. A., Tanre, D., Li, R.-R., Kleidman, R., Mattoo, S., Levy, R. C., Eck, T. F., Holben, B. N.,
1506   Ichoku, C., Martins, J. V., and Koren, I.: A Critical Examination of the Residual Cloud Contamination and
1507   Diurnal Sampling Effects on MODS Estimates of Aerosol Over Ocean, IEEE T. Geosci. Remote, 43,
1508   https://doi.org/10.1109/TGRS.2005.858430, 2005.

1509   Kazadzis, S., Kouremeti, N., Nyeki, S., Gröbner, J., and Wehrli, C.: The World Optical Depth Research and
1510   Calibration Center (WORCC) quality assurance and quality control of GAW-PFR AOD measurements,
1511   Geosci. Instrum. Method. Data Syst., 7, 39-53, https://doi.org/10.5194/gi-7-39-2018, 2018.

Kinne, S., Akerman, T. P., Shiobara, M., Uchiyama, A., Heymsfield, A. J., Miloshevich, L., Wendell, J., Eloranta, E., Purgold, C., and Bergstrom, R. W.: Cirrus cloud radiative and microphysical properties from ground observations and in situ measurements during FIRE 1991 and their application to exhibit problems in cirrus solar radiative transfer modeling, J. Atmos. Sci., 54, 2320–2344, https://doi.org/10.1175/1520-0469(1997)054%3C2320:CCRAMP%3E2.0.CO;2, 1997

Kline, Morris: Calculus: An Intuitive and Physical Approach, Dover. 457–461, ISBN 978-0-486-40453-0, 1998.

Komhyr, W. D., Grass, K. D., and Leonard, R. K.: Dobson Spectrophotometer 83: a standard for total ozone measurements, 1962-1987, J. Geophys. Res., 94, 9847–9861, https://doi.org/10.1029/JD094iD07p09847, 1989.

Levy, R. C., Remer, L. A., Kleidman, R. G., Mattoo, S., Ichoku, C., Kahn, R., and Eck, T. F.: Global evaluation of the Collection 5 MODIS dark-target aerosol products over land, Atmos. Chem. Phys., 10, 10399–10420, https://doi.org/10.5194/acp-10-10399-2010, 2010.

Levy, R. C., Mattoo, S., Munchak, L. A., Remer, L. A., Sayer, A. M., Patadia, F., and Hsu, N. C.: The Collection 6 MODIS aerosol products over land and ocean, Atmos. Meas. Tech., 6, 2989–3034, https://doi.org/10.5194/amt-6-2989-2013, 2013.

Lewis, J., Campbell, J., Welton, E. J., Stewart, S. A., and Haftings, P. C.: Overview of MPLNET Version 3 Cloud Detection, J. Atmos. Ocean Tech., https://doi.org/10.1175/JTECH-D-15-0190.1, 2016.

Li, Z., Zhao, X., Kahn, R., Mishchenko, M., Remer, L., Lee, K.-H., Wang, M., Laszlo, I., Nakajima, T., and Maring, H.: Uncertainties in satellite remote sensing of aerosols and impact on monitoring its long-term trend: a review and perspective, Ann. Geophys., 27, 2755–2770, https://doi.org/10.5194/angeo-27-2755-2009, 2009.

Li, Z., Xia, X., Cribb, M., Mi, W., Holben, B., Wang, P., Chen, H., Tsay S.-C., Eck, T. F., Zhao, F., Dutton, E. G. and Dickerson, R. E.: Aerosol optical properties and their radiative effects in northern China, J. Geophys. Res., 112, D22S01, https://doi.org/10.1029/2006JD007382, 2007.

Li, Z., Li, K., Li, D., Yang, J., Xu, H., Goloub, P., and Victori, S.: Simple transfer calibration method for a Cimel Sun–Moon photometer: calculating lunar calibration coefficients from Sun calibration constants, Appl. Opt. 55, 7624-7630, https://doi.org/10.1364/AO.55.007624, 2016.

Lin, N.-H., S.-C. Tsay, H. B. Maring, M.-C. Yen, G.-R. Sheu, S.-H. Wang, et al.: An overview of regional experiments on biomass burning aerosols and related pollutants in Southeast Asia: From BASE-ASIA and the Dongsha Experiment to 7-SEAS, Atmos. Environ., 78, 1–19, https://doi.org/10.1016/j.atmosenv.2013.04.066, 2013.

Martins, J. V., Tanré, D., Remer, L., Kaufman, Y., Mattoo, S., and Levy, R.: MODIS Cloud screening for remote sensing of aerosols over oceans using spatial variability, Geophys. Res. Lett., 29(12), https://doi.org/10.1029/2001GL013252, 2002.

McPeters, R. D., Frith, S., and Labow, G. J.: OMI total column ozone: extending the long-term data record, Atmos. Meas. Tech., 8, 4845–4850, https://doi.org/10.5194/amt-8-4845-2015, 2015.

Michalsky, J.: The astronomical almanac's algorithm for approximate solar position (1950–2030), Solar Energy, 40, 227–235, https://doi.org/10.1016/0038-092X(88)90045-X, 1988.

Michalsky, J. J., J.C. Liljegren and Harrison, L. C: A Comparison of Sun Photometer Derivations of Total Column Water Vapor and Ozone to Standard Measures of Same at the Southern Great Plains Atmospheric Radiation Measurement Site, J. Geophys. Res., 100, 25995–26003, https://doi.org/10.1029/95JD02706, 1995.

Mitchell, R. M., Forgan, B. W., and Campbell, S. K.: The Climatology of Australian Aerosol, Atmos. Chem. Phys., 17, 5131-5154, https://doi.org/10.5194/acp-17-5131-2017, 2017.

Mlawer, E. J., V. H. Payne, J.-L. Moncet, J. S. Delamere, M. J. Alvarado and D. D. Tobin: Development and recent evaluation of the MT_CKD model of continuum absorption, Phil. Trans. Roy. Soc. A, 370, 1–37, https://doi.org/10.1098/rsta.2011.0295, 2012.

Nakajima, T., Tonna, G., Rao, R., Boi, P., Kaufman, Y., and Holben, B.: Use of sky brightness measurements from ground for remote sensing of particulate polydispersions, Appl. Opt. 35, 2672–2686, https://doi.org/10.1364/AO.35.002672, 1996.

Omar, A. H., Winker, D. M., Tackett, J. L., Giles, D. M., Kar, J., Liu, Z., Vaughan, M. A., Powell, K. A., and Trepte, C. R., CALIOP and AERONET aerosol optical depth comparisons: One size fits none, J. Geophys. Res. Atmos., 118, 4748–4766, https://doi.org/10.1002/jgrd.50330, 2013.

O'Neill, N. T., Eck, T. F., Holben, B. N., Smirnov, A., Dubovik, O., and Royer, A.: Bimodal size distribution influences on the variation of Angstrom derivatives in spectral and optical depth space, J. Geophys. Res., 106, 9787–9806, https://doi.org/10.1029/2000JD900245, 2001.

O'Neill, N. T., Eck, T. F., Smirnov, A., Holben, B. N., and Thulasiraman, S.: Spectral discrimination of coarse and fine mode optical depth, J. Geophys. Res., 108, D17, 4559–4573, https://doi.org/10.1029/2002JD002975, 2003.

O'Neill, N. T., Eck, T. F., Reid, J. S., Smirnov, A., and Pancrati, O.: Coarse mode optical information retrievable using ultraviolet to short-wave infrared Sun photometry: Application to United Arab Emirates Unified Aerosol Experiment data, J. Geophys. Res., 113, D05212, https://doi.org/10.1029/2007JD009052, 2008.

Prasad, A. K. and Singh R. P.: Validation of MODIS Terra, AIRS, NCEP/DOE AMIP-II Reanalysis-2, and AERONET Sun photometer derived integrated precipitable water vapor using ground-based GPS receivers over India, J. Geophys. Res., 114, D05107, doi: 10.1029/2008JD011230, 2009.

Pérez-Ramírez, D., Whiteman, D. N., Smirnov, A., Lyamani, H., Holben, B. N., Pinker, R., Andrade, M., and Alados-Arboledas, L.: Evaluation of AERONET precipitable water vapor versus microwave radiometry, GPS, and radiosondes at ARM sites, J. Geophys. Res. Atmos., 119, 9596–9613, https://doi.org/10.1002/2014JD021730, 2014.

Redemann, J., Masonis, S. J., Schmid, B., Anderson, T. L., Russell, P. B., Livingston, J. M., Dubovik, O., and Clarke, A. D.: Clear-column closure studies of aerosols and water vapor aboard the NCAR C-130 during ACE-Asia, 2001, J. Geophys. Res., 108(D23), 8655, https://doi.org/10.1029/2003JD003442, 2003.

Remer, L. A., Kaufman, Y. J., Tanré, D., Mattoo, S., Chu, D. A., Martins, J. V., Li, R., Ichoku, C., Levy, R. C., Kleidman, R. G., Eck, T. F., Vermote, E., and Holben, B. N.: The MODIS Aerosol Algorithm, Products, and Validation. J. Atmos. Sci., 62, 947–973, https://doi.org/10.1175/JAS3385.1, 2005.

Rossow, W. B. and Schiffer, R. A.: Advances in Understanding Clouds from ISCCP. Bull. Amer. Meteor. Soc., 80, 2261–2288, https://doi.org/10.1175/1520-0477(1999)080<2261:AIUCFI>2.0.CO;2, 1999.

Russell, P. B., Livingston, J. M., Dutton, E. G., Pueschel, R. F., Reagen, J. A., DeFoor, T. E., Box, M. A., Allen, D., Pilewskie, P., Herman, B. M., Kinne, S. A. and Hoffman, D. J..: Pinatubo and pre-Pinatubo optical-depth spectra: Mauna Loa measurements, comparisons, inferred particle size distributions, radiative effects, and relationship to lidar data, J. Geophys. Res., 98(D12), 22969–22985, https://doi.org/10.1029/93JD02308, 1993.

Sakerin S.M., Kabanov D.M., Panchenko M.V., Pol'kin V.V., Holben B.N., Smirnov A.V., Beresnev S.A., Gorda S.Yu., Kornienko G.I., Nikolashkin S.V., Poddubnyi V.A., Tashchilin M.A: Monitoring of atmospheric aerosol in the Asian part of Russia in 2004 within the framework of AEROSIBNET program, Atmospheric and oceanic optics, 18, 11, 871–878, 2005.

Sapucci, L.F., Machado, L.A., Monico, J.F., and Plana-Fattori, A.: Intercomparison of Integrated Water Vapor Estimates from Multisensors in the Amazonian Region. J. Atmos. Oceanic Technol., 24, 1880–1894, https://doi.org/10.1175/JTECH2090.1, 2007.

Sassen, K., and Campbell, J. R.: A midlatitude cirrus cloud climatology from the Facility for Atmospheric Remote Sensing. Part I: Macrophysical and synoptic properties, J. Atmos. Sci., 58, 481–496, https://doi.org/10.1175/1520-0469(2001)058%3C0481:AMCCCF%3E2.0.CO;2, 2001.

Sayer, A. M., Hsu, N. C., Bettenhausen, C., and Jeong, M.-J.: Validation and uncertainty estimates for MODIS Collection 6 "Deep Blue" aerosol data, J. Geophys. Res. Atmos., 118, 7864–7872, https://doi.org/10.1002/jgrd.50600, 2013.

Schmid, B., Thome, K.J., Demoulin, P., Peter, R., Matzler, C., and Sekler, J.: Comparison of modeled and empirical approaches for retrieving columnar water vapor from solar transmittance measurements in the 0.94 micron region, J. Geophys. Res., 101, 9345–9358, https://doi.org/10.1029/96JD00337, 1996.

Schmid, B, Michalsky, J. J., Slater, D. W., Barnard, J. C., Halthore, R. N., Liljegren, J. C., Holben, B. N., Eck, T. F., Livingston, J. M., Russell, P. B., Ingold, T., and Slutsker, I.: Comparison of Columnar Water-Vapor Measurements from Solar Transmittance Methods, Appl. Opt. 40, 1886–1896, https://doi.org/10.1364/AO.40.001886, 2001.

Shaw, G. E., Reagan, J. A., and Herman, B. M.: Investigations of atmospheric extinction using solar radiation measurements made with multiple wavelength radiometer, J. Appl. Meteorol., 12, 374–380, https://doi.org/10.1175/1520-0450(1973)012%3C0374:IOAEUD%3E2.0.CO;2, 1973.

Shaw, G.E., Sun Photometry, Bull. Am. Meteor. Soc., 64, 4-10, https://doi.org/10.1175/1520-0477(1983)064%3C0004:SP%3E2.0.CO;2, 1983.

1619 Shi, Y. R., Levy, R. C., Eck, T. F., Fisher, B., Mattoo, S., Remer, L. A., Slutsker, I., and Zhang, J.: Characterizing
1620   the 2015 Indonesia Fire Event Using Modified MODIS Aerosol Retrievals, Atmos. Chem. Phys. Discuss.,
1621   https://doi.org/10.5194/acp-2018-468, in review, 2018.

1622 Sinyuk, A., Holben, B. N., Smirnov, A., Eck, T. F., Slutsker, I., Schafer, J. S., Giles, D. M., and Sorokin, M.:
1623   Assessment of error in aerosol optical depth measured by AERONET due to aerosol forward scattering,
1624   Geophys. Res. Lett., 39, L23806, https://doi.org/10.1029/2012GL053894, 2012.

1625 Smirnov, A., Holben, B. N., Eck, T. F., Dubovik, O., and Slutsker, I.: Cloud screening and quality control
1626   algorithms for the AERONET database, Rem. Sens. Env., 73, 337-349, https://doi.org/10.1016/S0034-
1627   4257(00)00109-7, 2000.

1628 Smirnov, A, Holben, B.N., Lyapustin A., Slutsker, I. and Eck, T.F.: AERONET processing algorithms refinement,
1629   AERONET 2004 Workshop, El Arenosillo, Spain, May 10–14, 2004.

1630 Smirnov, A., Holben, B. N., Slutsker, I., Giles, D. M., McClain, C. R., et al.: Maritime Aerosol Network as a
1631   component of Aerosol Robotic Network, J. Geophys. Res., 114, D06204,
1632   https://doi.org/10.1029/2008JD011257, 2009.

1633 Takamura, T, T. Nakajima and SKYNET community group: Overview of SKYNET and its Activities, Proceedings
1634   of AERONET workshop, El Arenosillo., Optica Pura y Aplicada, 37, 3303–3308, 2004.

1635 Toledano, C., Cachorro, V. E., Berjon, A., de Frutos, A. M., Fuertes, D., Gonzalez, R., Torres, B., Rodrigo, R.,
1636   Bennouna, Y., Martin, L., and Guirado, C.: RIMA-AERONET network: long-term monitoring of aerosol
1637   properties, Opt. Pura Apl., 44, 629–633, 2011.

1638 Toledano, C., González, R., Fuertes, D., Cuevas, E., Eck, T. F., Kazadzis, S., Kouremeti, N., Gröbner, J., Goloub,
1639   P., Blarel, L., Román, R., Barreto, Á., Holben, B. N., and Cachorro, V. E.: Assessment of Sun photometer
1640   Langley calibration at the high-elevation sites Mauna Loa and Izaña, Atmos. Chem. Phys. Discuss.,
1641   https://doi.org/10.5194/acp-2018-430, in review, 2018.

1642 Tzortziou, M., Herman, J. R., Cede, A., and Abuhassan, N.: High precision, absolute total column ozone
1643   measurements from the Pandora spectrometer system: Comparisons with data from a Brewer double
1644   monochromator and Aura OMI, J. Geophys. Res., 117, D16303, https://doi.org/10.1029/2012JD017814,
1645   2012.

1646 USNO: Approximate Solar Coordinates derived from The Astronomical Almanac, pg. C5:
1647   http://aa.usno.navy.mil/faq/docs/SunApprox.php.

1648 Van Malderen, R., Brenot, H., Pottiaux, E., Beirle, S., Hermans, C., De Mazière, M., Wagner, T., De Backer, H.,
1649   and Bruyninx, C.: A multi-site intercomparison of integrated water vapour observations for climate change
1650   analysis, Atmos. Meas. Tech., 7, 2487-2512, https://doi.org/10.5194/amt-7-2487-2014, 2014.

1651 Wang S.-H., Tsay, S.-C., Lin, N.-H., Chang, S.-C., C. L., Welton, E. J., Holben, B. N., Hsu, N. C., Lau, W. K. M.,
1652   Lolli, S., Kuo, C.-C., Chia, H.-P., Chiu, C.-Y., Lin, C.-C., Bell, S. W., Ji, Q., Hansell, R. A., Sheu, G.-R.,
1653   Chi, K.-H., and Peng, C.-M.: Origin, transport, and vertical distribution of atmospheric pollutants over the
1654   northern South China Sea during the 7-SEAS/Dongsha Experiment, Atmospheric Environment, 78 , 124–
1655   133, https://doi.org/10.1016/j.atmosenv.2012.11.013, 2013.

1656 Welton, E. J., Voss, K. J., Gordon, H. R., Maring, H., Smirnov, A., Holben, B., Schmid, B., Livingston, J. M.,
1657   Russell, P. B., Durkee, P. A., Formenti, P., and Andreae, M. O.: Ground-based Lidar Measurements of
1658   Aerosols During ACE-2: Instrument Description, Results, and Comparisons with other Ground-based and
1659   Airborne Measurements, Tellus B, 52, 635–650, https://doi.org/10.1034/j.1600-0889.2000.00025.x, 2000.
1660 Welton, E.J., and Campbell, J.R.: Micro-pulse Lidar Signals: Uncertainty Analysis, J. Atmos. Oceanic Technol., 19,
1661   2089–2094, https://doi.org/10.1175/1520-0426(2002)019%3C2089:MLSUA%3E2.0.CO;2, 2002.
1662 Zibordi, G., Holben, B., Melin, F., D'Alimonte, D., Berthon, J.-F, Slutsker, I., and Giles, D.: AERONET-OC: an
1663   overview, Can. J. Remote Sens., 36, 5, https://doi.org/10.5589/m10-073, 2010.
1664

1665 **Table 1.** Nominal AERONET wavelengths for ion assisted deposition filters used for aerosol remote sensing and spectral
1666 corrections or components for each channel.

Nominal Central Wavelengths (nm)	Filter Bandpass (nm)	Spectral Corrections/ Components
340	2	Rayleigh, NO_2, O_3
380	2	Rayleigh, NO_2
440	10	Rayleigh, NO_2
500	10	Rayleigh, NO_2, O_3
675	10	Rayleigh, O_3
870	10	Rayleigh
935	10	Rayleigh, Aerosol
1020	10	Rayleigh, H_2O
1640	25	Rayleigh, H_2O, CO_2, CH_4

1667

1668

1669 **Table 2.** Summary of Cloud Screening Related Quality Control Changes from Version 2 to Version 3.

Algorithm/Parameter	Version 2	Version 3
Very High AOD Restoration	N/A	$\tau 870 > 0.5$; $\alpha 675\text{-}1020 > 1.2$ or $\alpha 870\text{-}1020 > 1.3$, restore if eliminated by cloud screening
Optical Air Mass Range	Maximum of 5.0	Maximum of 7.0
Number of Potential Measurements	$N_{remain} < 3$, reject all measurements in the day	After all checks applied, reject all measurements in the day if $N_{remain} < MAX\{3$ or 10% of N$\}$
Triplet Criterion	All wavelengths checked; AOD Triplet Variability $> MAX\{0.02$ or $0.03 *\tau_{aerosol}\}$	AOD Triplet Variability $> MAX\{0.01$ or $0.015 *\tau_{aerosol}\}$ for 675nm, 870nm, and 1020nm wavelengths simultaneously
Ångstrom Exponent (AE) Limitation	N/A	If $AE_{440-870nm} < -1.0$ or $AE_{440-870nm} > 3.0$, then eliminate triplet measurement.
Smoothness Check	D<16	For AOD500nm (or 440nm) $\Delta\tau_{aerosol} > 0.01$ per minute, then remove larger $\tau_{aerosol}$ in pair. Repeat condition for each pair until points are not removed.
Solar Aureole radiance Curvature Check (Sect. 3.2.2)	N/A	Using 1020nm solar aureole radiances, compute the curvature (k) between 3.2° and 6.0° scattering angle (φ) at the smallest scattering angle. If $k < 2.0E-5\ \varphi$ and if slope of curvature (M) is greater than 4.3 (empirically determined), then radiances are cloud contaminated. For sky scan measurements, all $\tau_{aerosol}$ measurements are removed within 30 minutes of the sky measurement. For Model T, special aureole scan measurements will remove all $\tau_{aerosol}$ within a two minute period superseding any sky scan aureole measurements.
Standalone Measurements	N/A	If no data exists within 1 hour of a measurement, then reject it unless AE440-870nm>1.0.
AOD Stability Check	Same as Version 3	Daily averaged AOD 500nm (or 440nm) has σ less than 0.015, then do not perform 3-σ check.
3-σ Check	Same as Version 3	AOD 500nm and AE440-870nm should be within the MEAN$\pm 3\sigma$; otherwise, the points are rejected.

1670

1671

1672   **Table 3.** AERONET and MPLNET sites and date ranges used for assessing cirrus and non-cirrus cloud presence

Site	Latitude	Longitude	Elevation (meters)	Date Range
GSFC	38.9925° N	76.8398° W	87	May 2001–Jan 2013
COVE	36.9000° N	75.7100° W	37	May 2004–Jan 2008
Kanpur	26.5128° N	80.2316° E	123	May 2009–Jan 2013
SEDE_BOKER	30.8550° N	34.7822° E	480	Nov 2007–Apr 2013
Santa_Cruz_Tenerife	28.4725° N	16.2473° W	52	Nov 2005–Jan 2013
Singapore	1.2977° N	103.7804° E	30	Aug 2009–Jan 2013
Ragged_Point	13.1650° N	59.4320° W	40	Jun 2008–Jan 2013
Trinidad_Head	41.0539° N	124.1510° W	105	May 2005–Feb 2013

1673

1674

1675 **Table 4.** Thresholds used to determine the independent and dependent AOD diurnal dependence. Satisfying both the slope and
1676 correlation coefficient (R) conditions would constitute the possible removal of all measurements for a day.

Day Removal Type	AOD Diurnal Shape	Analyzed Period	Slope Threshold	R Threshold
Independent	Concave	AM, PM, Day	>0.25	>0.974
Dependent	Concave	AM, PM	>0.04	>0.94
Dependent	Concave	Day	>0.1	>0.94
Dependent	Convex	AM, PM, Day	<−0.02	<−0.94
Dependent − τ_{avg}<0.1	Convex	AM, PM, Day	<−0.1	<−0.94
Independent − 2 or more Silicon wavelengths (440, 675, 870, 1020nm) or 1640nm InGaAs	Concave	AM, PM, Day	>0.1 Day or AM & PM > 0.02	>0.94

1677

1678

1679 **Table 5**. Statistics corresponding to Fig. 21 and Fig. 22 for AOD interpolated to 500nm, Ångstrom exponent 440–870nm,
1680 precipitable water (cm), and the number of days. Version 3 Level 2.0 and Version 2 Level 2.0 data are compared for the same
1681 multi-year monthly averages when sites have a total of more than 1000 days for all months and more than 30 days in each month.
1682 Data represented as "Matched" indicates the further condition that the exact observations were matched in Version 2 and Version
1683 3 Level 2.0 multi-year monthly average data sets. Note that PW values for the "Matched" data set are approximately the same as
1684 the unmatched data set.

Parameter	AOD_{500nm} (V3−V2) Unmatched	$AE_{440-870nm}$ (V3−V2) Unmatched	PW (cm) (V3−V2) Unmatched	Days (V3−V2) Unmatched	AOD_{500nm} (V3−V2) Matched	$AE_{440-870nm}$ (V3−V2) Matched
Average	0.002	−0.01	−0.02	−0.4	−0.002	−0.03
Standard Deviation	0.022	0.10	0.06	24.8	0.004	0.10
Maximum	0.247	0.29	0.34	150	0.015	0.35
Minimum	−0.166	−1.54	−0.45	−130	−0.029	−1.63
Number of Months	2953	2953	2953	2953	2514	2514

1685

1686
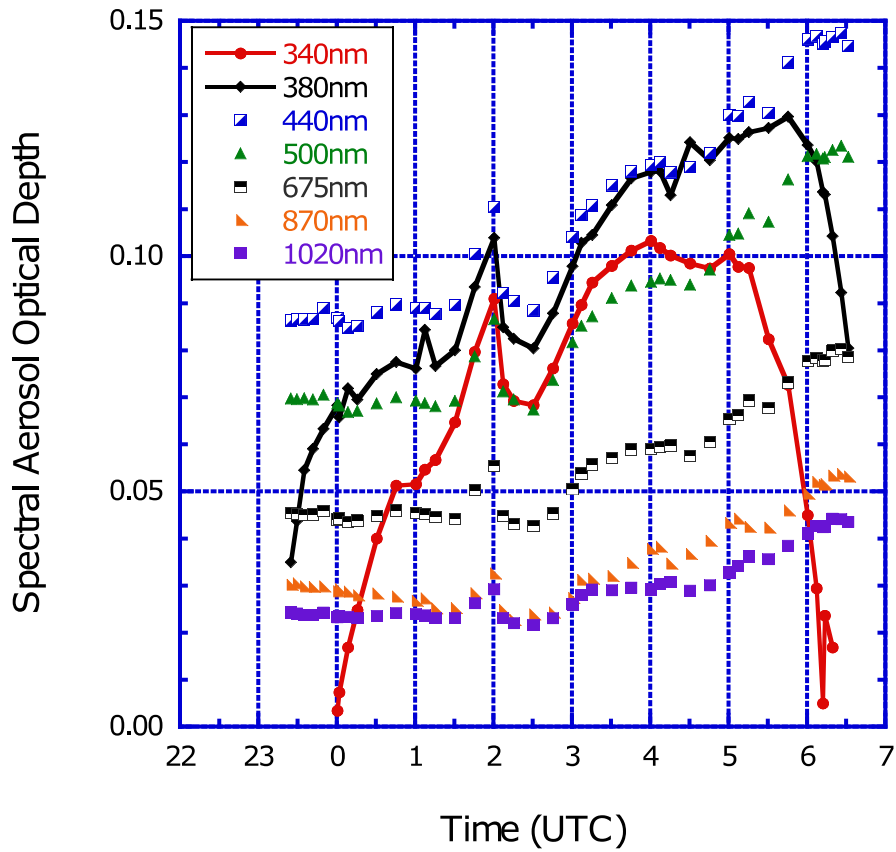
1687

Figure 1. Aerosol optical depth (AOD) data from AERONET Ussuriysk site (43.70° N, 132.16° E) on 30 November 2005 shows electronic instability. For the Cimel Model 4 instruments, the electronic sensitivity of the UV AOD data (340nm and 380nm) can be high due to a bad amplifier. The resulting AOD data for the UV channels are out of spectral dependence the entire day with a maximum error for large optical air mass due to large dark current values. The UV channels (identified by line plots) are removed by the quality control while preserving other wavelengths that are not affected by this condition.

1693
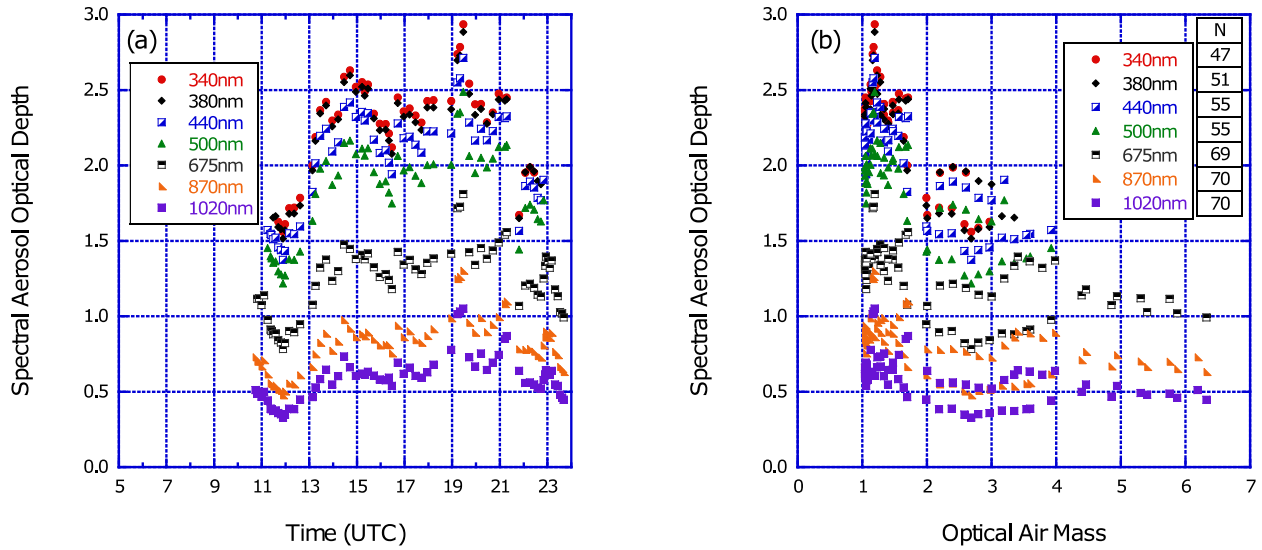
Figure 2. Spectral dependent low digital number removal at NASA Goddard Space Flight Center (GSFC; 38.99°N, 76.84°W). **(a)** Level 1.0 AOD data from GSFC on 8 July 2002 are plotted for the Quebec forest fire smoke event. Significantly fewer Level 1.0 AOD data are available for the shorter wavelengths near local sunrise (~11 UTC) and sunset (~23:30 UTC). **(b)** The distribution of the AOD measurements with respect to optical air mass clearly shows the removal of short wavelengths for large air mass in this fine mode aerosol event. The high aerosol loading due to smoke and haze results in significant extinction at UV and visible wavelengths, which corresponds to low digital counts. The low digital count quality control removes AOD measurements impacted by diffuse radiation scattered into the instrument field of view (Sinyuk et al., 2012).

1703
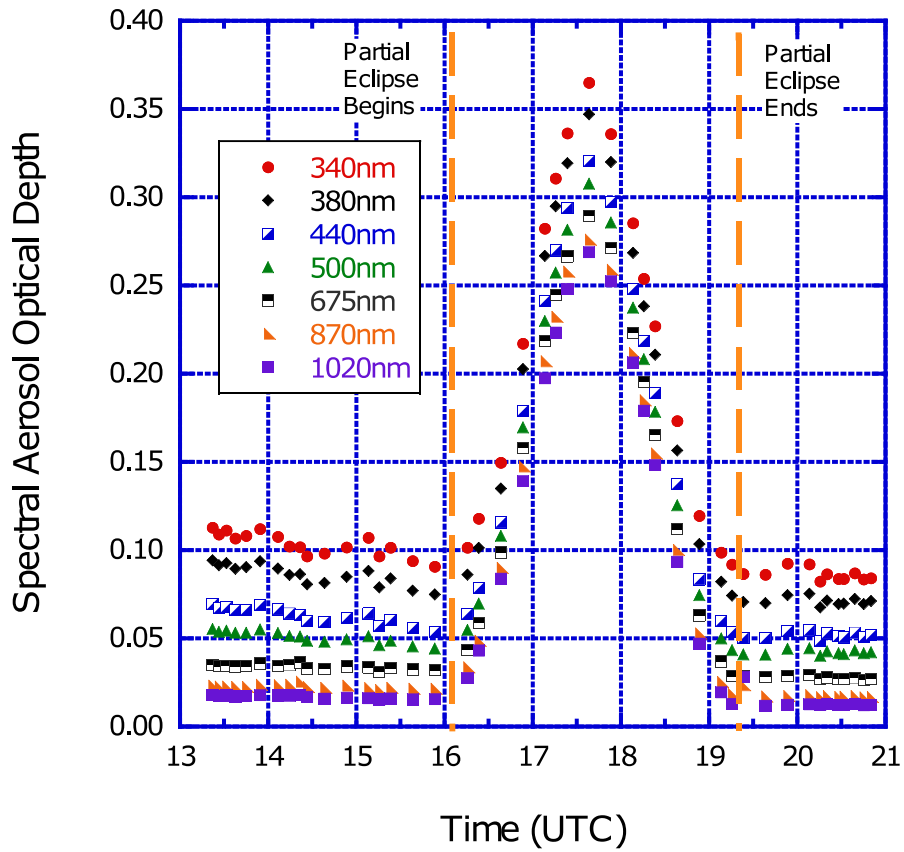
Figure 3. Eclipse circumstance at the NASA Goddard Space Flight Center (GSFC; 38.99° N, 76.84° W) on 25 December 2000 between 16:04:13 UTC and 19:16:25 UTC. The maximum AOD during the eclipse occurs at the maximum obscuration of 0.42, which results in a change of ~0.28 for AOD 500nm compared to data before and after the solar eclipse. Utilizing the NASA Solar Eclipse database, the AOD measurements are removed between the partial eclipse first contact and partial eclipse last contact as denoted by the vertical dashed lines.

1709

1710
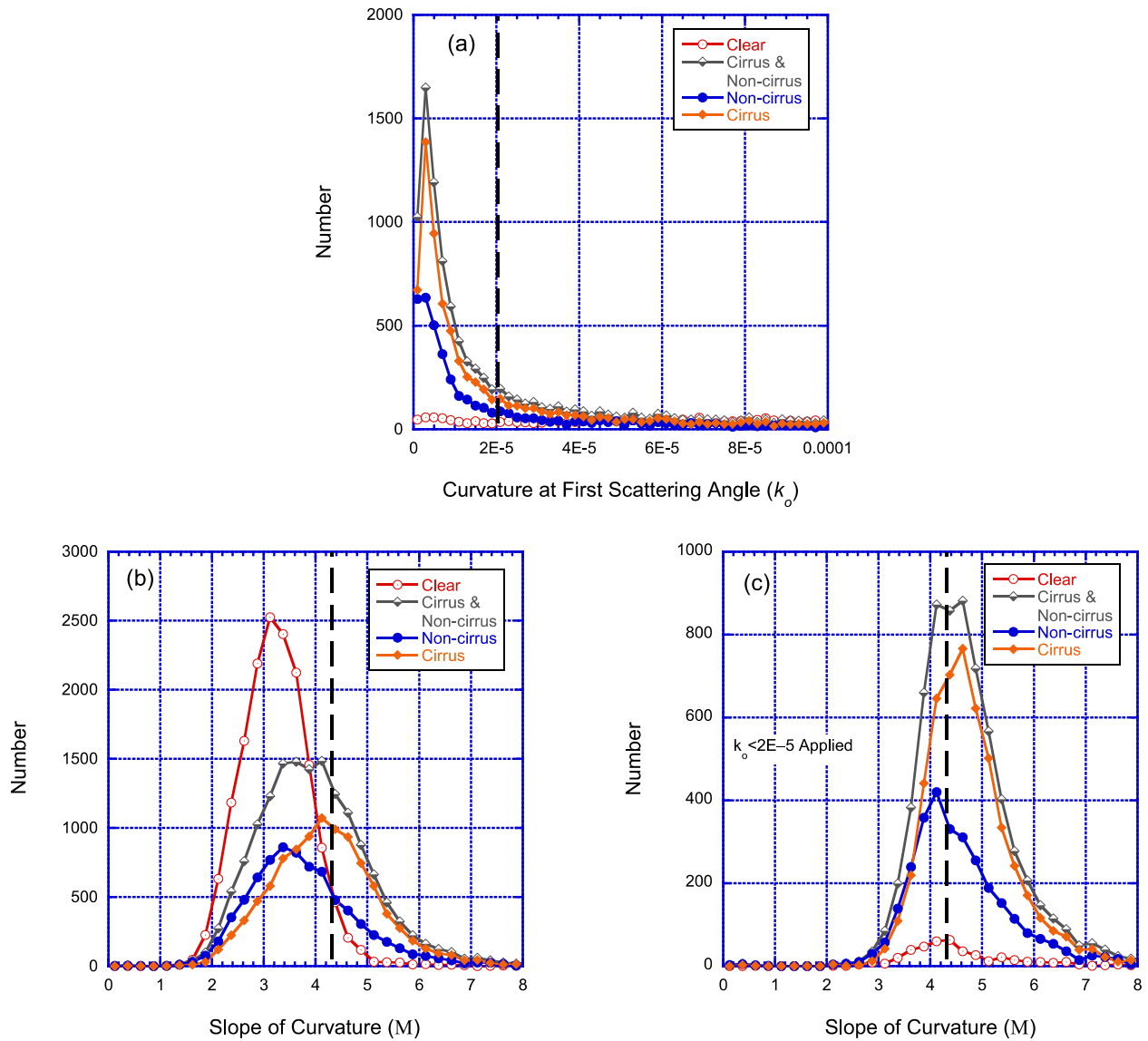
1711

Figure 4. NASA Goddard Space Flight Center (GSFC; 38.99° N, 76.84° W) AERONET data coincident with MPLNET LIDAR derived sky condition categories (Clear, both Cirrus and Non-cirrus clouds, Non-cirrus clouds, and Cirrus clouds) from 2001–2013. The AERONET solar aureole 1020nm radiances are used to calculate the curvature at the first scattering angle (k_o) and the slope of curvature (M) between 3.2° and 6.0° scattering angles. **(a)** The number distribution of k_o is shown and the dashed vertical line at k_o equals 2E-5 indicates the threshold where values less than 2E−5 are considered possibly cirrus cloud contaminated (the x-axis is truncated at 1E−4 for viewing purposes). **(b)** The number distribution of M is shown and M greater than 4.3 are considered to be possibly cirrus cloud contaminated (the dashed vertical line indicates the threshold of 4.3). **(c)** Similar to panel (b) except that the k_o threshold (k_o<2E−5) is applied first and, as a result, data greater than 4.3 in this panel are considered to be cirrus cloud contaminated.

1721
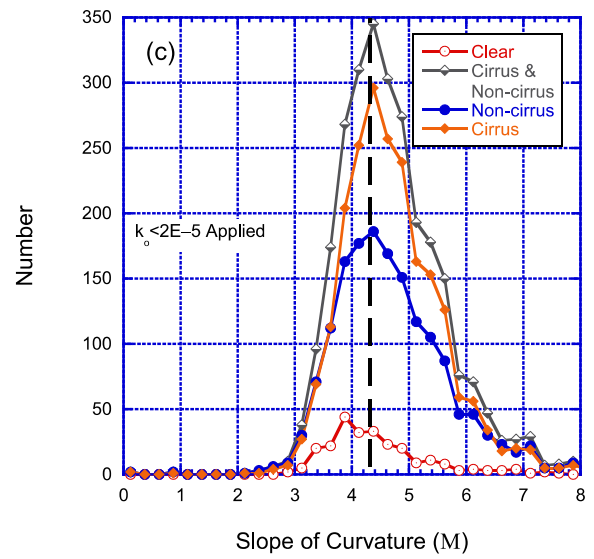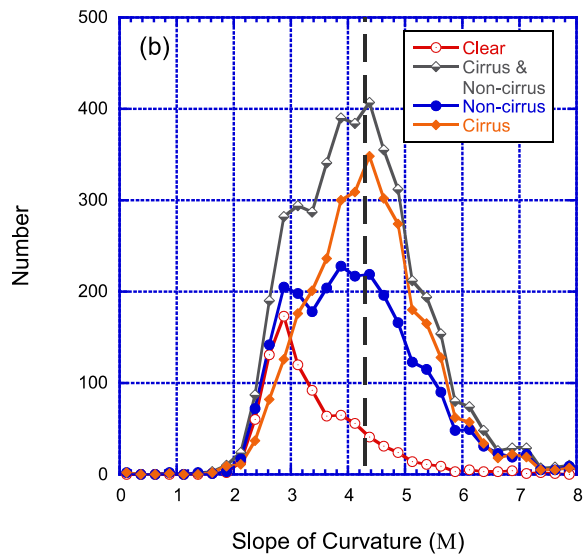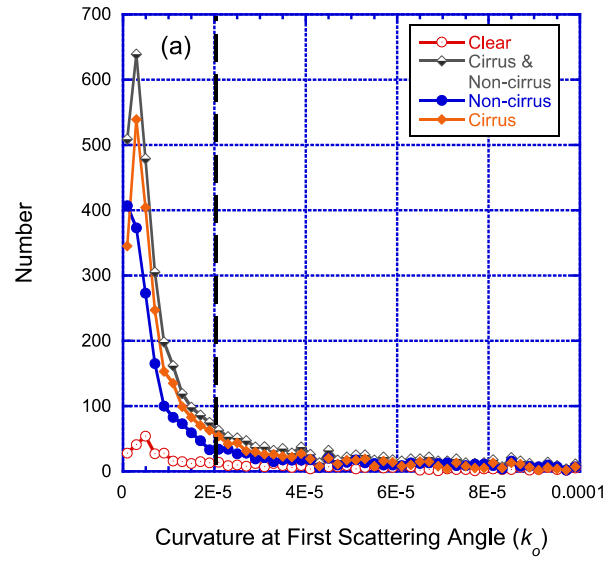
1722

1723 **Figure 5.** Similar to Fig. 4, except for Singapore (1.29° N, 103.78° E) from 2009–2013.

1724
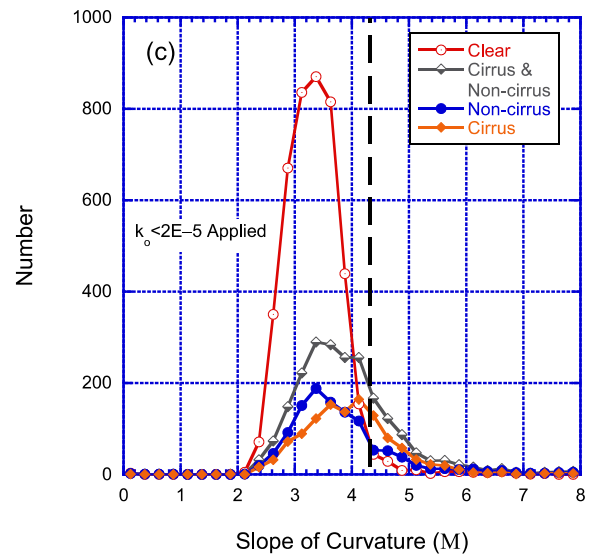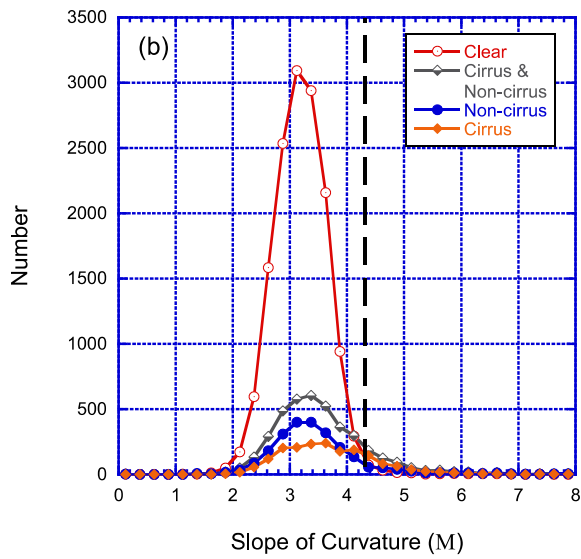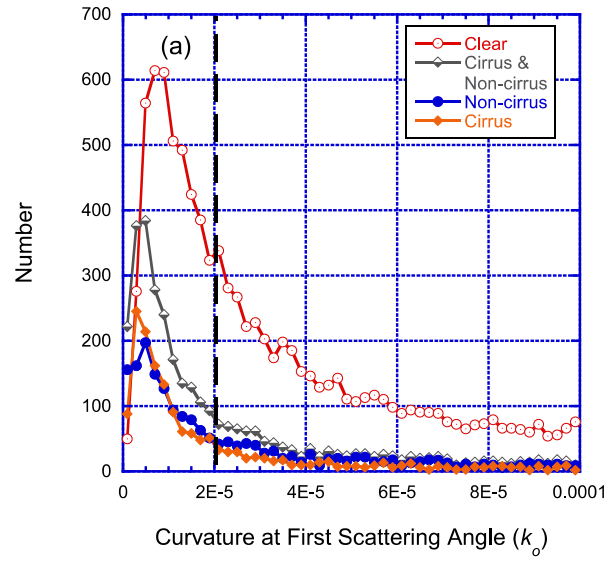
1725

1726 **Figure 6.** Similar to Fig. 4, except for SEDE BOKER (30.85° N, 34.78° E) from 2007–2013.

1727
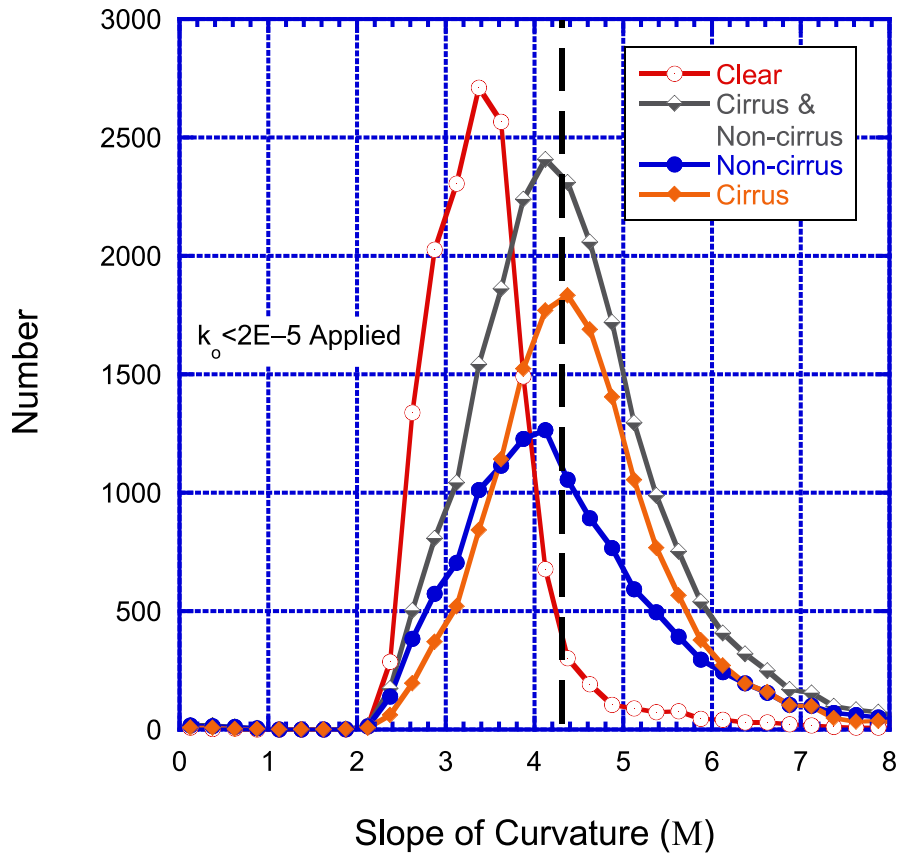
1728

1729   **Figure 7.** Similar to Fig. 4c including all analyzed sites in Table 3.

1730

k	M	AOD$_{app\ 1020nm}$
2.4E-5	2.8	0.30
9.4E-6	4.4	0.13
7.4E-6	5.4	0.38
1.2E-5	4.4	0.32
1.4E-4	2.2	0.14
8.4E-4	5.0	0.03
7.0E-6	3.5	0.01
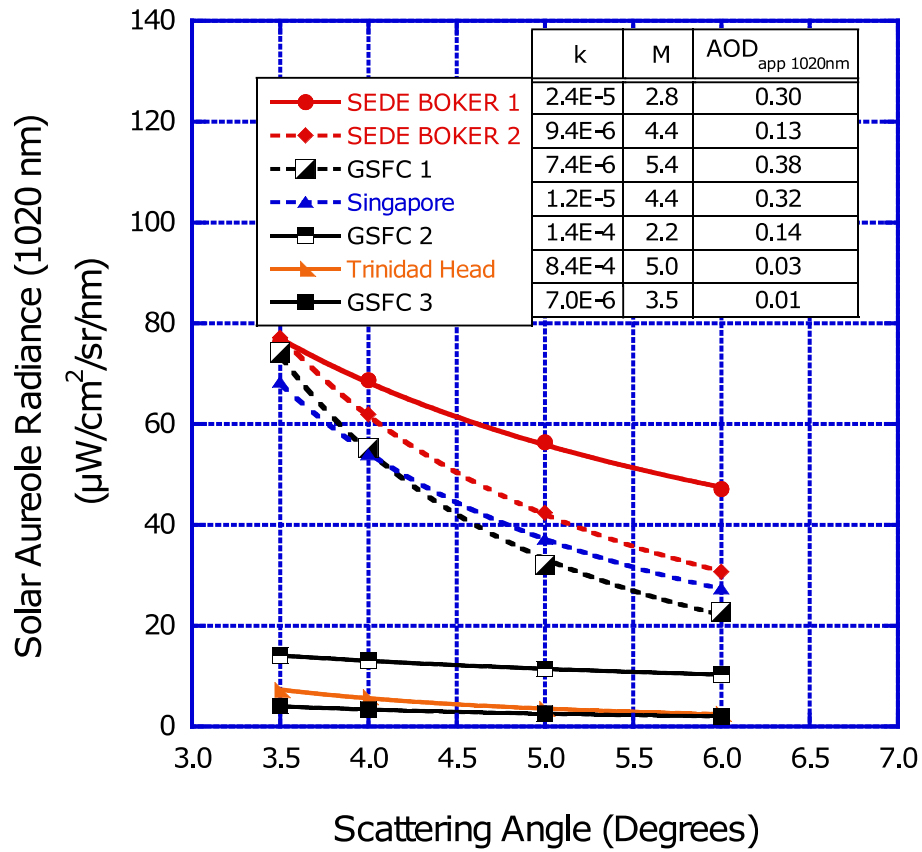
1731

Figure 8. The solar aureole 1020nm radiance versus the scattering angle in degrees for selected sites. Data plots with the dashed lines (i.e., SEDE BOKER 2, GSFC 1, and Singapore) all qualify for the removal of data due to optically thin homogeneous cloud contamination.

1735
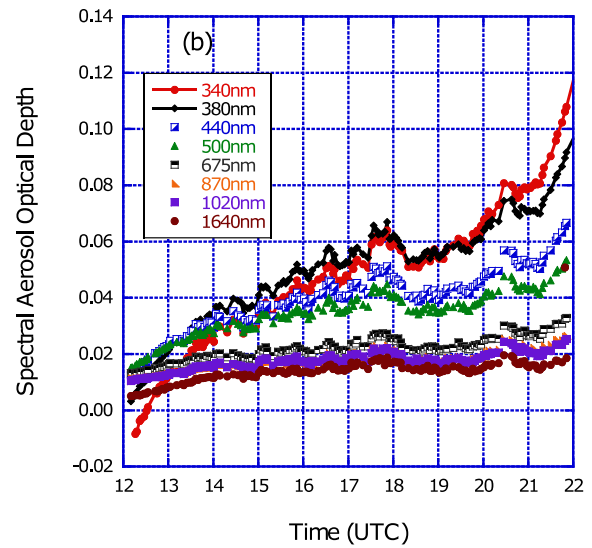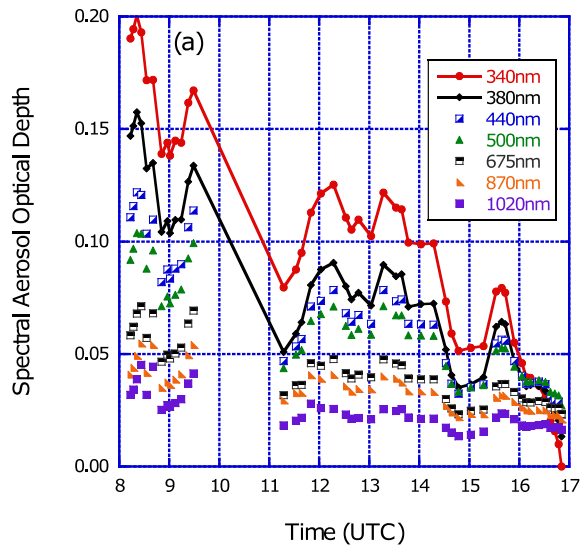
1736

1737   **Figure 9**. Time shifted aerosol optical depth (AOD) data examples at Malaga (36.72° N, 4.48° W) and Toronto (43.79° N,
1738   79.47° W). Note the line plot is used to emphasize the 340nm and 380nm AOD impact for the time shift. **(a)** The Level 1.5
1739   AOD cloud screened only data measured at the Malaga site on 30 January 2014. These data show the time shifted AOD
1740   especially at short wavelengths represent the instrument clock is too fast. **(b)** The Level 1.5 AOD cloud screened only data
1741   measured at the Toronto site on 24 September 2013. The time shifted aerosol optical depth especially at short wavelengths
1742   represent when the instrument clock was too slow. Panel (a) also shows the algorithm can be used with data gaps and lower
1743   temporal resolution measurement interval compared to panel (b).

1744
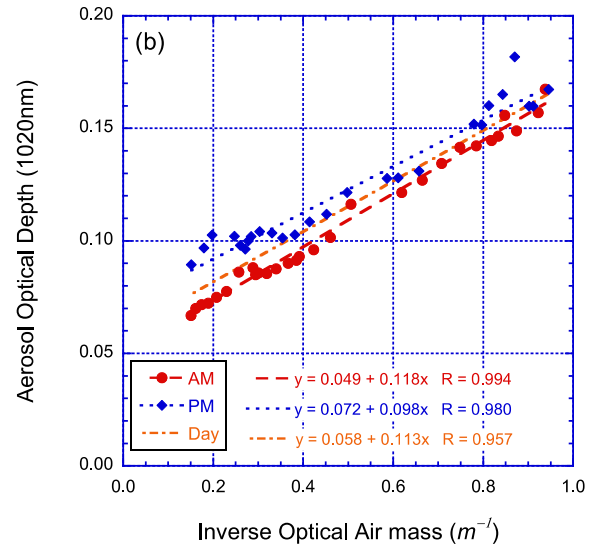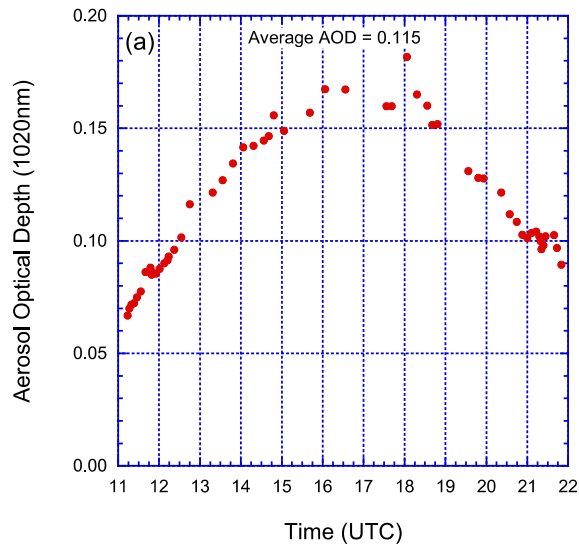
1745

1746 **Figure 10**. AERONET data collected at Rio Branco (9.96 °S, 67.87° W) on 30 August 2011. The AOD 1020nm Level 1.5 with
1747 only the cloud screening algorithm applied to the data. **(a)** The AOD diurnal dependence presents a concave shape during the
1748 solar day. **(b)** The AOD 1020nm and the inverse optical air mass show a highly correlated linear fit and the slope is significant
1749 for the full day (day) and morning (AM), and afternoon (PM). Data separation for AM and PM is defined by the local solar
1750 noon, which is 16:31:28 UTC at Rio Branco.

1751
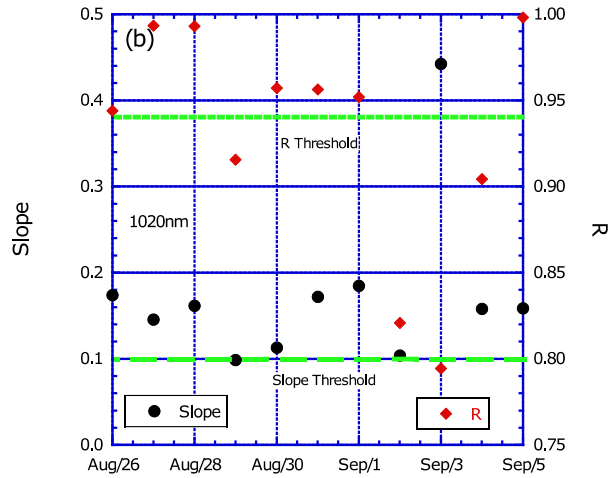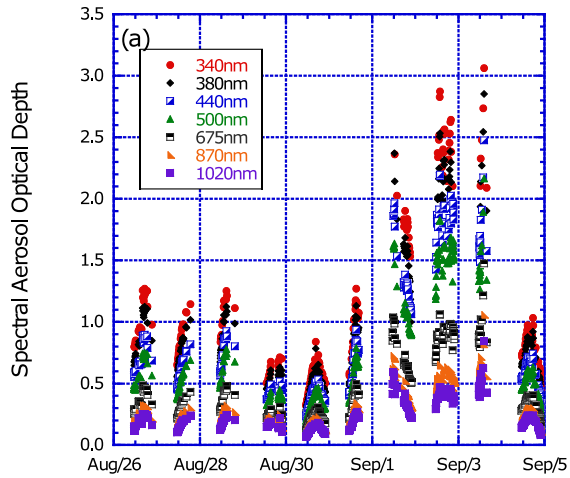
1752

Figure 11. AERONET data collected at Rio Branco (9.96° S, 67.87° W) from 15 August to 30 September 2011. **(a)** The time series of Level 1.5 spectral AOD (cloud screened only) data is plotted from 26 August to 5 September 2011 and shows repeated diurnal dependence for varying magnitudes of AOD. **(b)** The robust linear fit slope and correlation coefficient (R) is calculated from the AOD 1020nm versus the inverse of the optical air mass (m^{-1}). For the full day evaluation, the green dashed line indicates the threshold for the slope parameter at 0.1 and the solid green line indicates the threshold for the correlation coefficient (R = 0.94). Both the slope and R must exceed these thresholds for at least three days scanning from the current day to the last occurrence within the 20-day period to remove the spectral AOD, and in this circumstance, all of the data are removed for the period for Levels 1.5 and 2.0.

1761
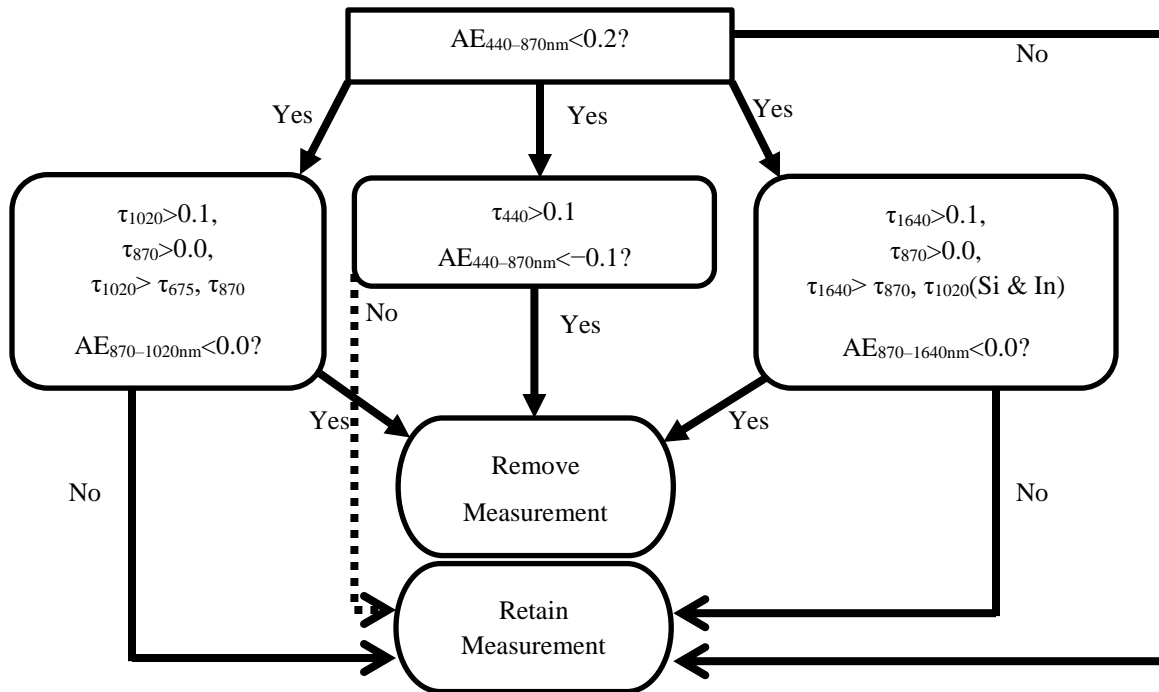
1762

1763 **Figure 12.** Flowchart of the reverse spectral dependence algorithm used to remove cloud contamination artifacts and instrument
1764 anomalies. The 1640nm wavelength is available on some Cimel Model 5 instruments and all Model T instruments.

1765
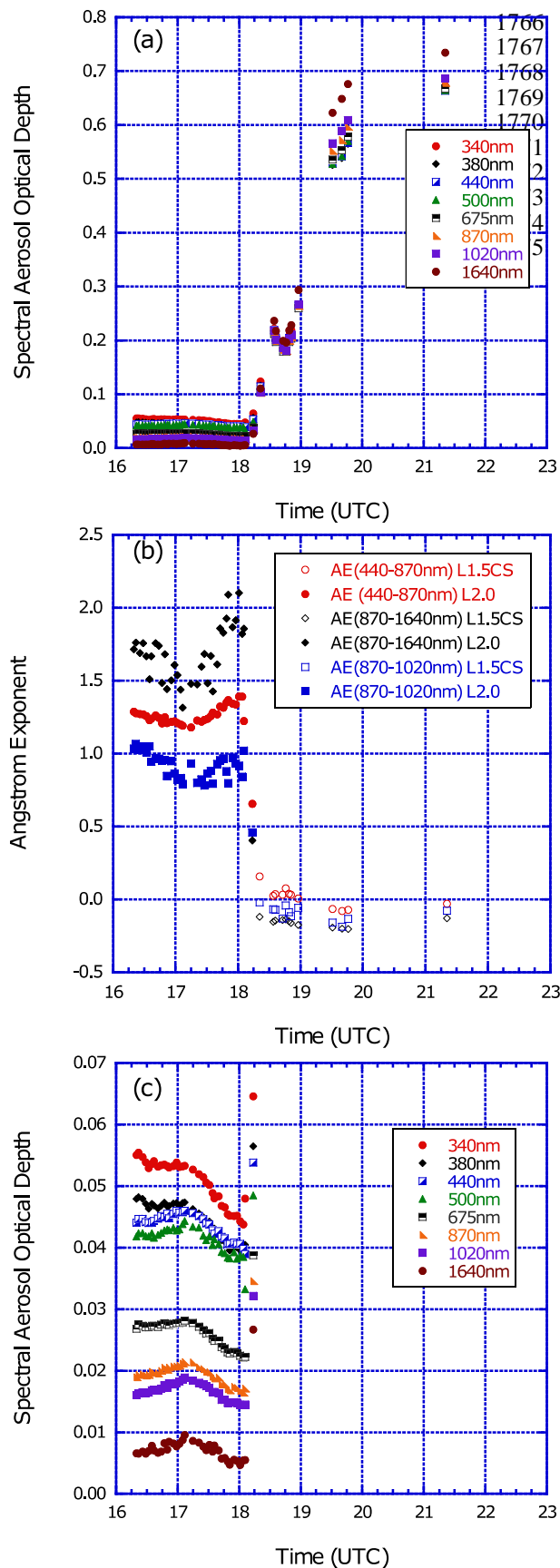
Figure 13. Data from Bratts Lake (50.20° N, 104.71° W) on 7 January 2007. **(a)** The Level 1.5 data with only the cloud screening (CS) algorithm applied shows cloud contaminated data remain after 18:10 UTC. **(b)** For the same period as (a), the Ångstrom exponent values decreased significantly to a level where coarse mode aerosol particles are not expected. **(c)** The final Level 1.5 and Level 2.0 data series after the reverse spectral dependence quality control or additional cloud screening method has been applied to the standalone Level 1.5 CS data.

1776
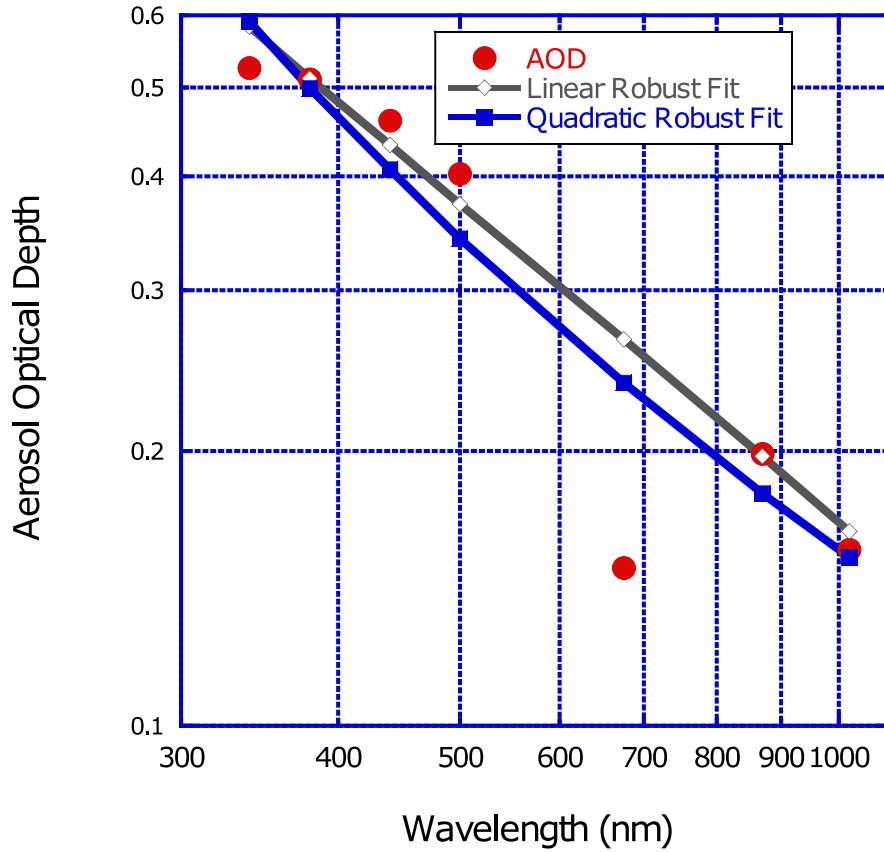
1777 **Figure 14.** AERONET data from the Osaka (34.65° N, 135.59° E) site on 16 October 2006 at 22:02:11 UTC. The plot shows
1778 AOD versus the wavelength with lines identifying the linear and quadratic robust regression fits on logarithmic scale used by the
1779 AOD spectral dependence algorithm. The 675nm channel is clearly anomalous with fits differing by 0.12 for linear and 0.09 for
1780 quadratic. In addition, the AOD 340nm appears anomalous with deviations of 0.06 from linear fit and 0.07 from quadratic fit.
1781 While both wavelengths exceed their respective AOD thresholds (0.023 for 675nm and 0.051 for 340nm), the algorithm
1782 determines the maximum deviation for linear and quadratic fits and removes the AOD 675nm measurement. A subsequent scan
1783 by the algorithm determined that the remaining AOD measurements from 340nm to 1020nm were within the established fit
1784 deviation thresholds.

1785
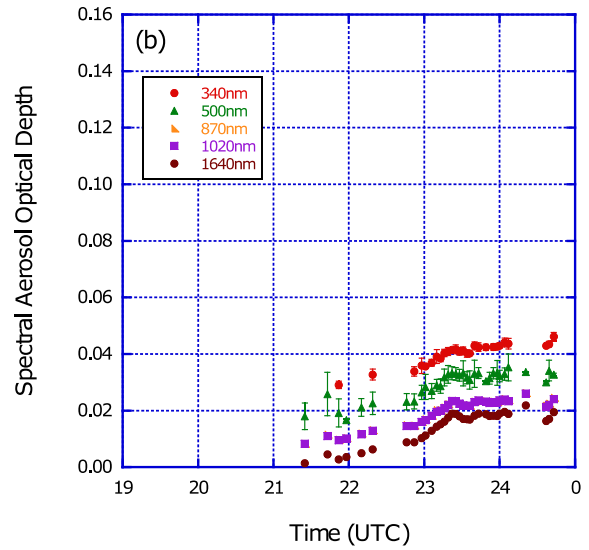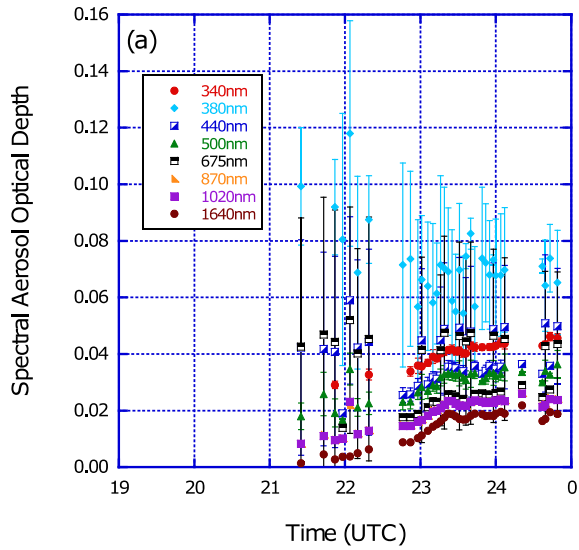
Figure 15. Spectral AOD exhibiting large triplet variability at PEARL (80.05° N, 86.42° W) on 25 August 2013. **(a)** Version 3 Level 1.5 cloud screened only data is plotted with large triplet variability and these data were not removed by the cloud screening. The error bars represent the triplet variability (AOD Max – AOD Min) divided by 2 so the full range represents the AOD triplet variability. The large triplet variability occurs mainly at shorter wavelengths than 675nm. **(b)** Data affected by large triplet variability (i.e., AOD 380nm, AOD 440nm, and AOD 675nm) are removed by using the Level 1.5 large triplet variability quality controls.
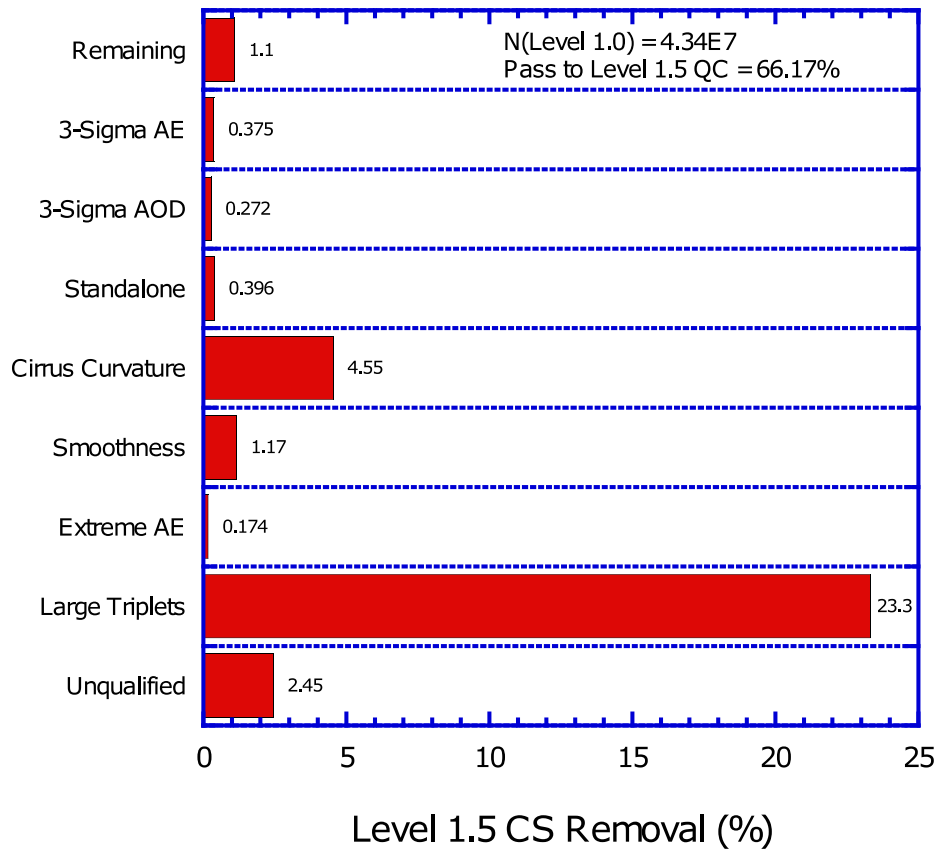
Level 1.5 CS Removal (%)

Figure 16. The Level 1.0 AOD measurement removal by the Level 1.5 cloud screening algorithm from 1993 to 2018. The plot shows the impact of the major cloud screening steps in the Level 1.5 cloud screening algorithm and removal of these data applies to all wavelengths. The triplet criterion removes more than 23% of the Level 1.0 data. Nearly 5% of the Level 1.0 data are removed due to cirrus cloud contamination. The "Remaining" category indicates the check performed after each cloud screening step to determine if enough measurements are available and do not meet the high AOD retention criteria. The "Unqualified" category indicates data that are not triplets or lack sufficient channels to participate in the cloud screening algorithm.

1801
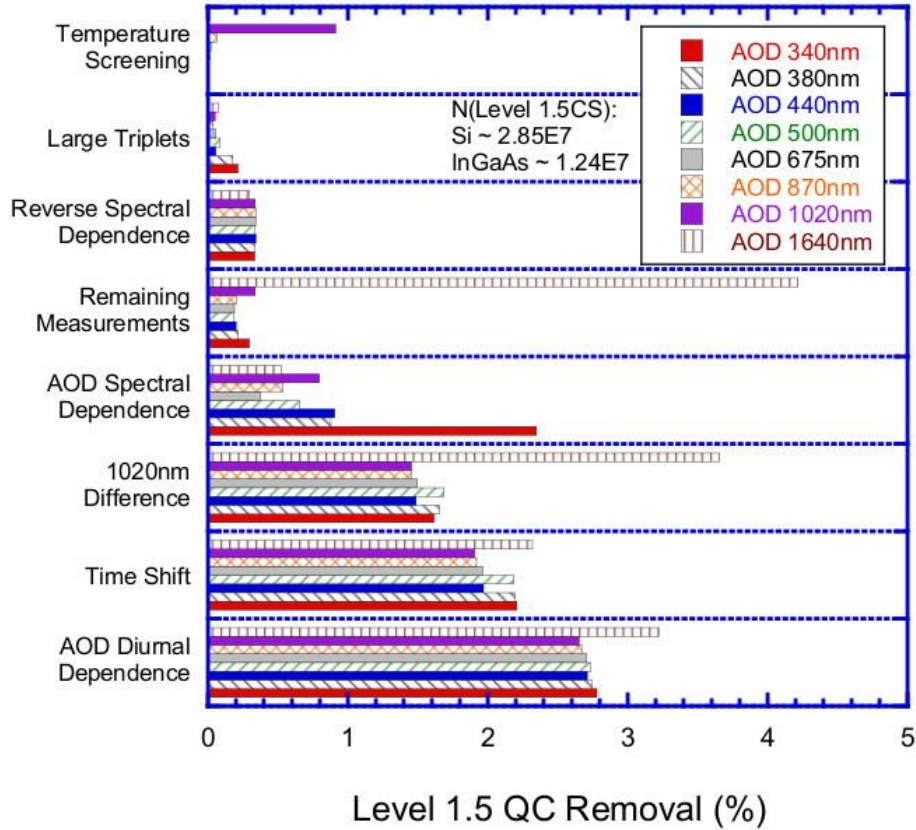
Figure 17. Level 1.5 quality control algorithm wavelength dependent impacts for each major step for the period analyzed from 1993–2018. The most significant removal for most channels is due to AOD diurnal dependence, time shift, and difference between AOD 1020nm on the Silicon and InGaAs detectors (resulting from collimator inconsistency). The AOD 340nm has significant removal of AOD spectral dependence. The 1640nm InGaAs channel has significant removal by "Remaining Measurements" since this wavelength cannot be checked for quality when the Silicon channels are not available. Temperature screening mostly applies to the 1020nm Silicon wavelength due to its strong temperature dependence near the edge of the signal sensitivity of the Silicon photodiode detector.
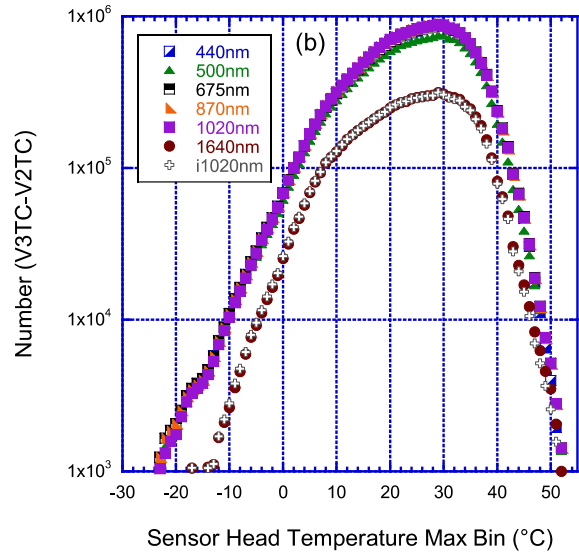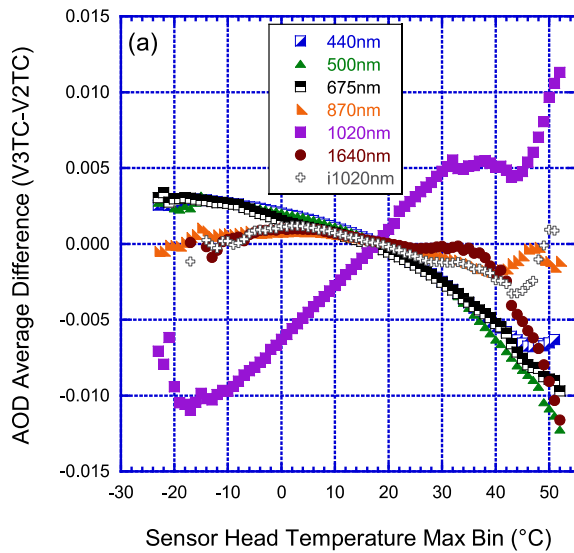
1810

1811 **Figure 18**. Difference in AOD response between Version 3 and Version 2 temperature correction applied to Version 3 AOD data
1812 based on the sensor head temperature from 1993–2018. The Version 2 temperature correction assumes temperature ranges for
1813 1020nm and no temperature correction for all other wavelengths, while Version 3 temperature correction characterizes the
1814 temperature response for each filter or set of default filters for each instrument for wavelengths ≥400nm. **(a)** The AOD average
1815 difference plotted for each 1°C temperature bin from −25°C to +55°C. The AOD 1020nm exhibits an opposite trend compared to
1816 the other wavelengths varying from −0.01 at low temperatures and up to +0.01 at high temperatures. Other wavelengths have
1817 slight differences at cold temperatures but apparent dependencies at high temperatures greater than 40°C possibly due to
1818 extrapolation of the temperature coefficients to higher temperatures. **(b)** The number of measurements plotted for each 1°C
1819 temperature bin with a minimum of 1000 observations.

1820
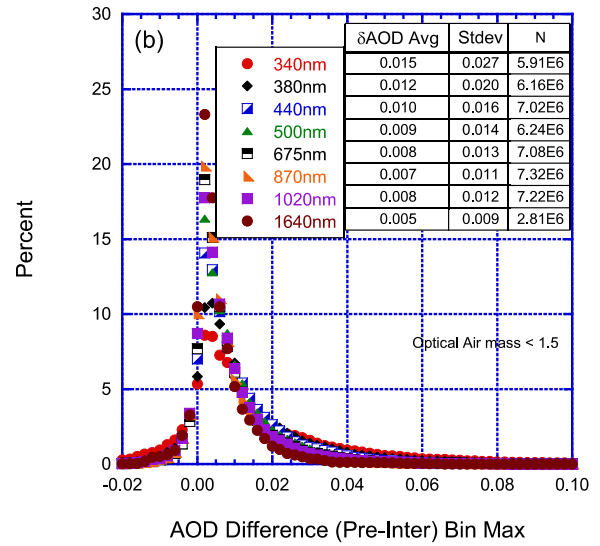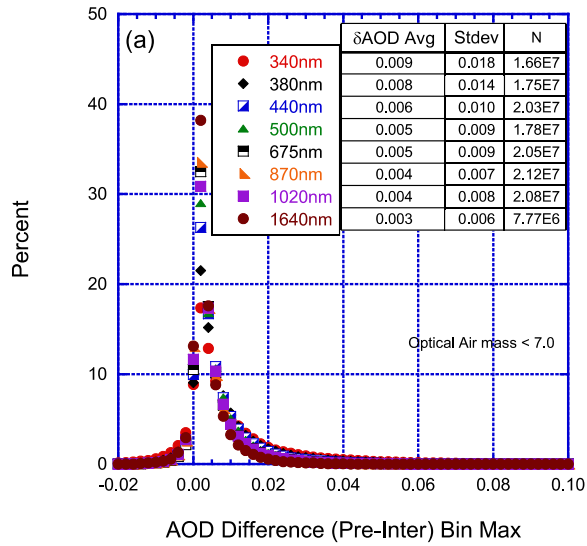
1821

1822 **Figure 19.** Using data qualified as Version 3, Level 2.0, aerosol optical depth (AOD) average difference comparing
1823 measurements only with the pre-field calibration applied versus instruments with both the pre-field and post-field calibrations
1824 applied from 1993–2018. Calibration sites are excluded from the analysis. The histogram of AOD differences is provided for the
1825 optical air mass $1.0 \leq m < 7.0$ range in panel **(a)** and $1.0 \leq m < 1.5$ range in panel **(b)**. The average difference is largest for the UV
1826 wavelengths and smallest for the longer wavelengths.

1827
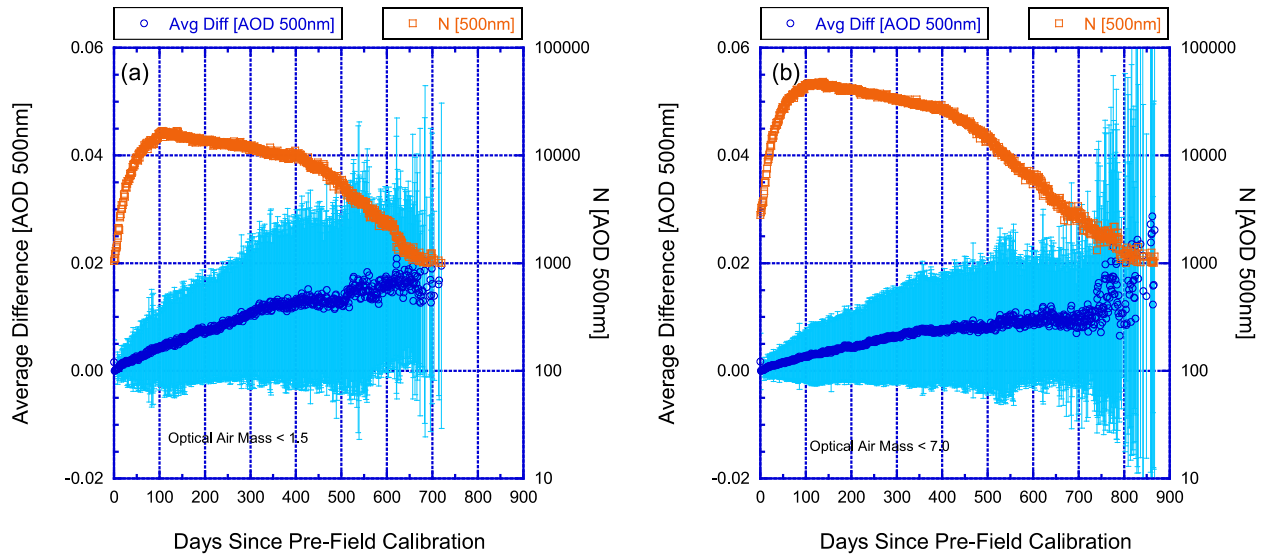
1828

Figure 20. Using data qualified as Version 3 Level 2.0 aerosol optical depth (AOD) 500nm average difference comparing
measurements only with the pre-field calibration applied versus instruments with both the pre-field and post-field calibrations
applied from 1993–2018. The AOD average differences are provided for the optical air mass 1.0≤m<7.0 range in panel **(a)** and
1.0≤m<1.5 range in panel **(b).** Vertical bars represent the standard deviation for each day bin. The secondary y-axis in
logarithmic scale represents the number of measurements of AOD 500nm for each day bin.

1834
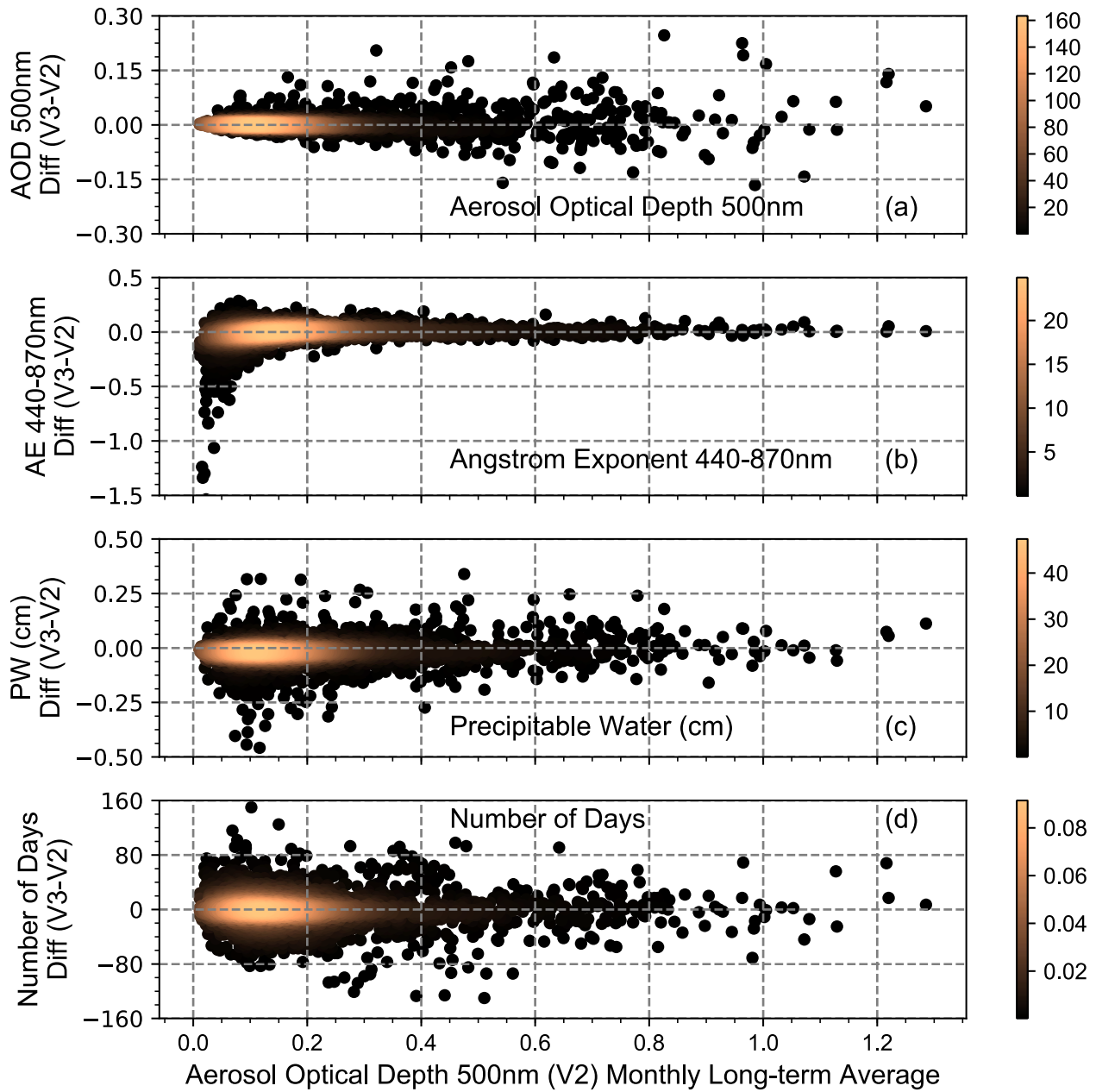
Figure 21. Comparison of Version 3 and Version 2 Level 2.0 multi-year monthly average data sets. **(a)** The aerosol optical depth (AOD) interpolated to 500nm to include data from instruments without 500nm. **(b)** The Ångstrom exponent (AE) is calculated utilizing the inclusive ordinary least squares regression fit from 440–870nm. **(c)** The precipitable water in cm is derived from the 935nm water vapor channel. **(d)** The difference in the number of days is determined for each monthly long-term average.

1841
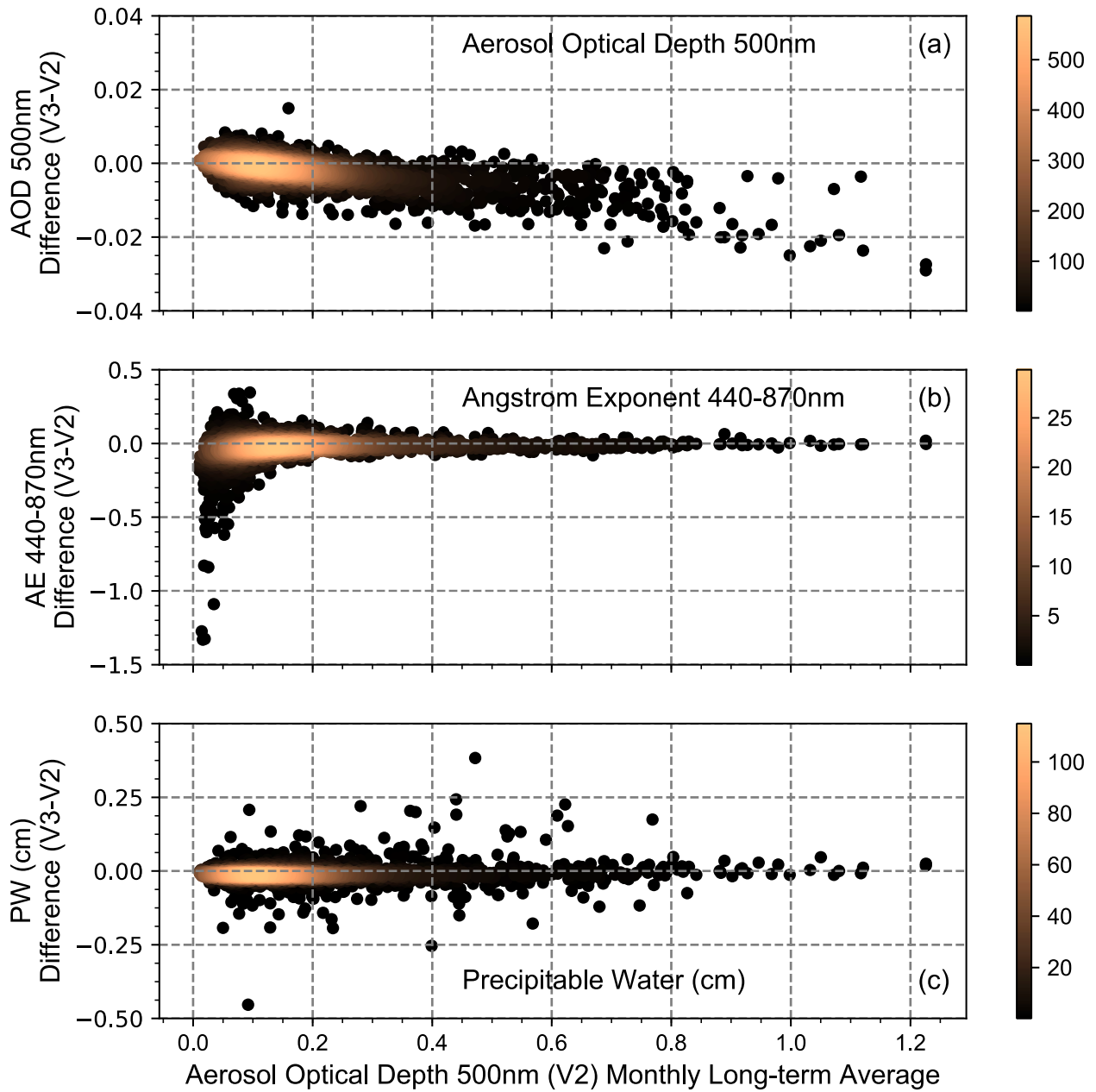
Figure 22. Comparison of Version 3 and Version 2 Level 2.0 multi-year monthly average data sets for time matched instantaneous observations in both data sets. The panels are similar to those in Fig. 21.

1842
1843

1844
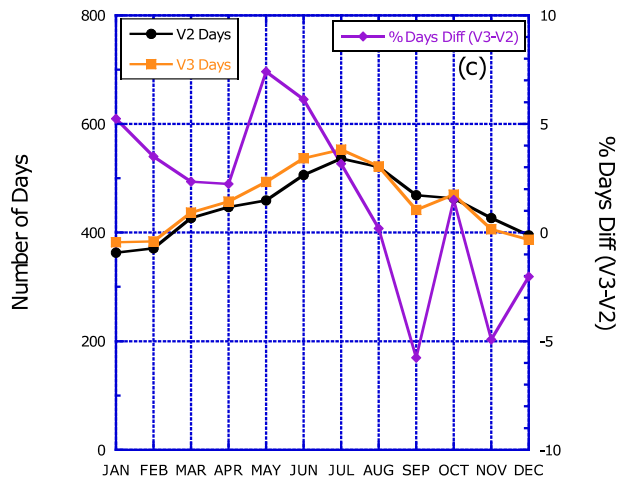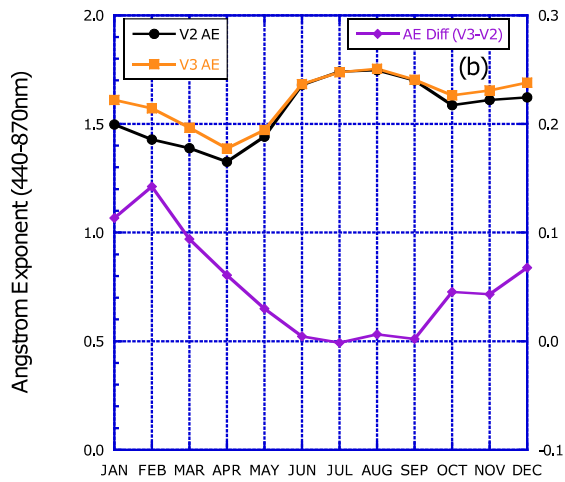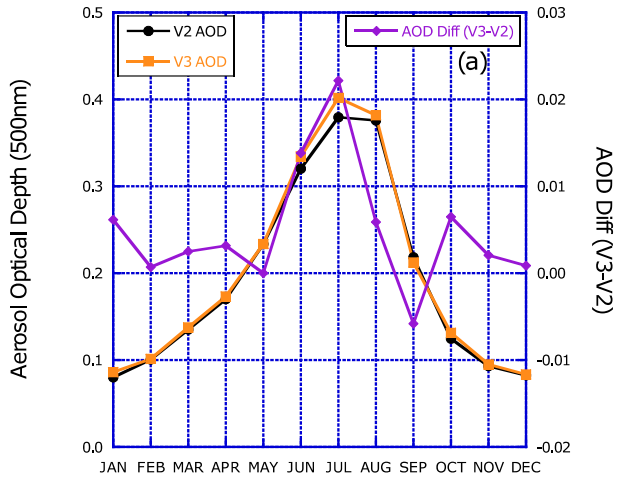
1845

1846   **Figure 23**. Long-term multi-year (1993–2016) monthly average comparisons of the Version 3 and Version 2 Level 2.0 data sets
1847   at the NASA Goddard Space Flight Center (GSFC), Maryland, USA. The panel **(a)** provides the AOD interpolated to 500nm for
1848   each version on the primary y-axis and differences on the secondary y-axis. The panels **(b)** and **(c)** are plotted similarly for the
1849 $AE_{440-870nm}$ and the number of days in the multi-year monthly average, respectively.

1850
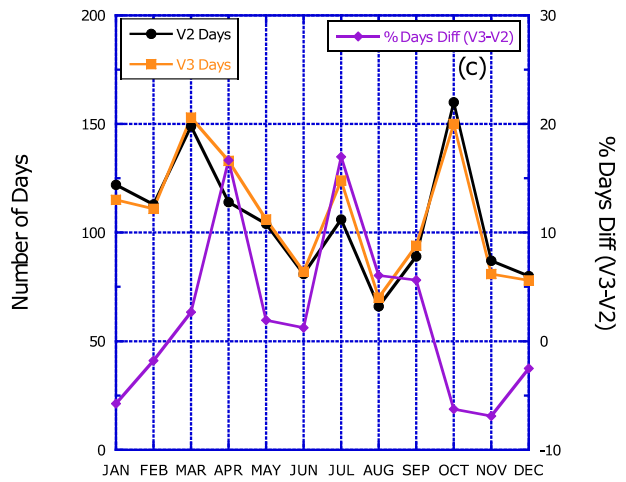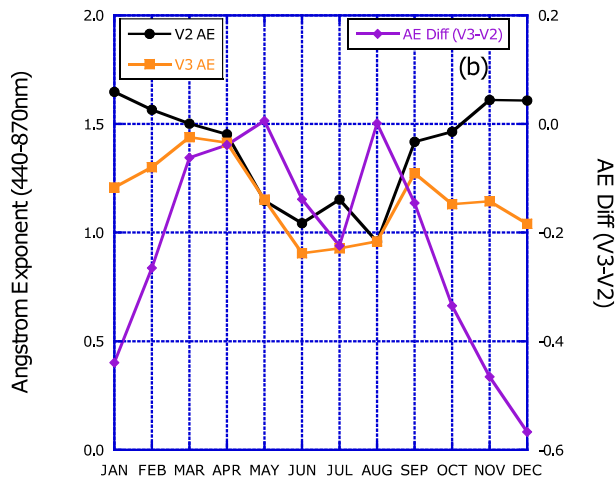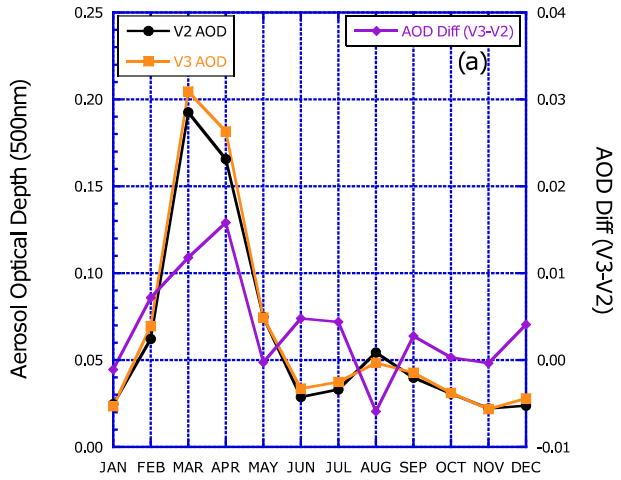
Figure 24. Similar to Fig. 23 except for Lulin, Taiwan (23.47° N, 120.87° E) from 2006–2017.
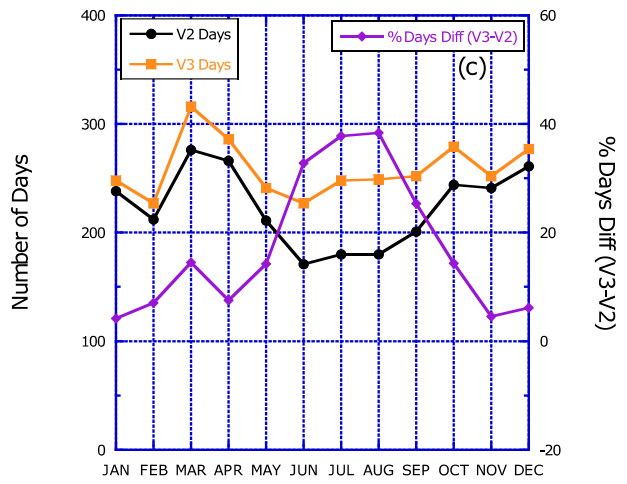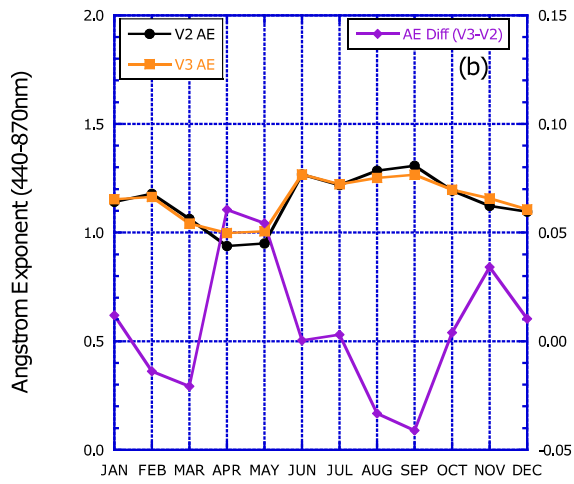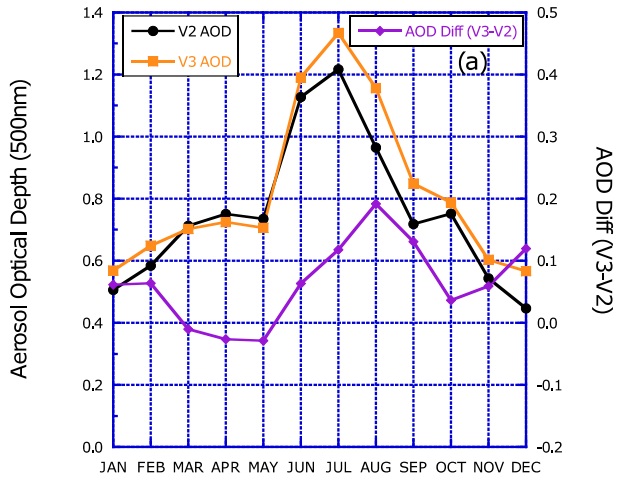
1854

1855   **Figure 25.** Similar to Fig. 23 except for XiangHe, China (39.75° N, 116.96° E) from 2001–2017, except 2009.

1856
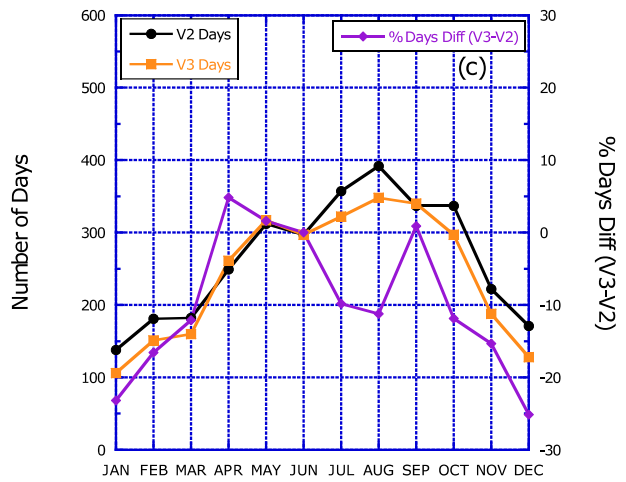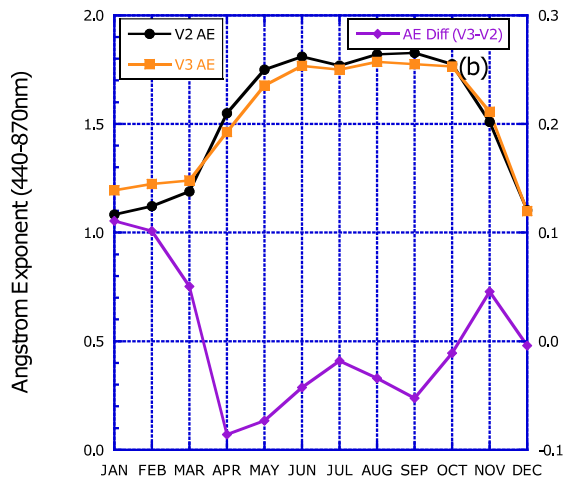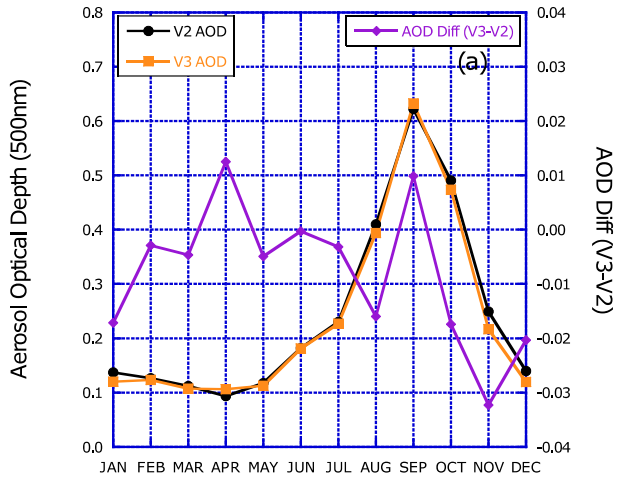
1857

1858 **Figure 26.** Similar to Fig. 23 except for Mongu, Zambia (15.25° S, 23.15° E) from 1997–2010.

1859
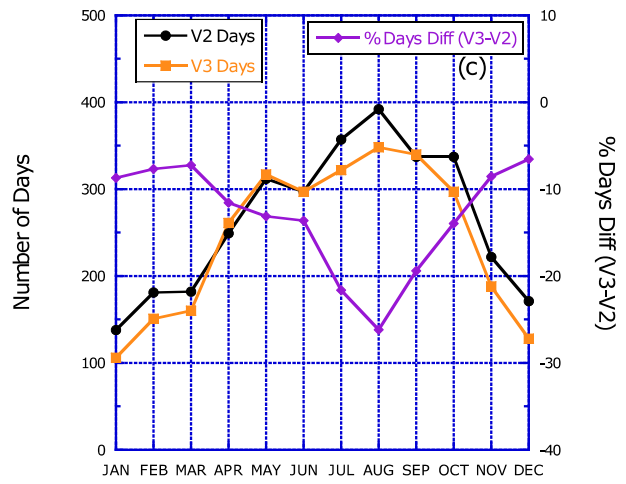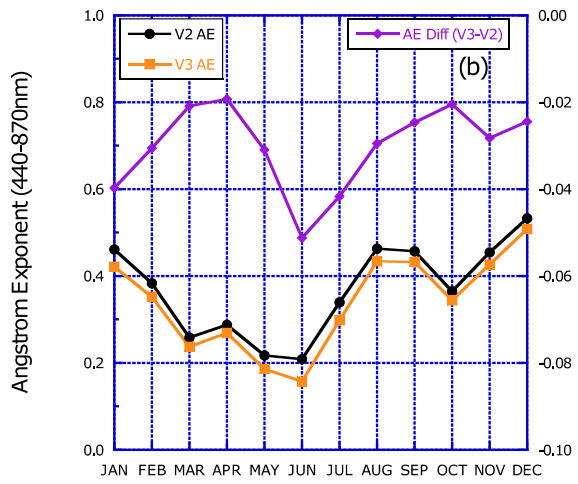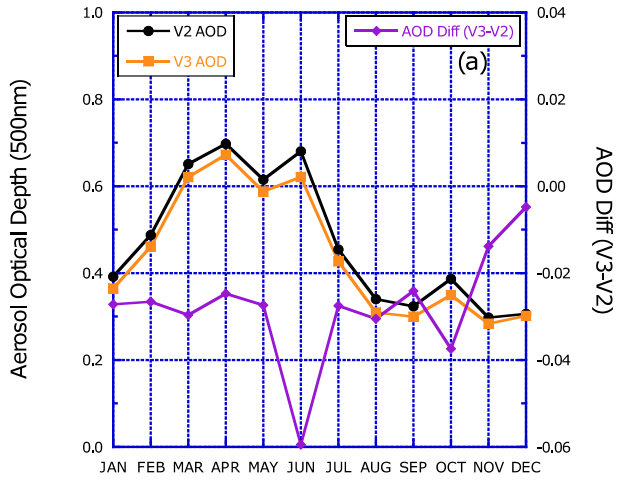
1860

1861 **Figure 27.** Similar to Fig. 23, except for IER-Cinzana, Mali (13.28° N, 5.93° W) from 2004-2017.